NASA CONTRACTOR REPORT 166297

Aeroacoustic Theory for Noncompact Wing-Gust Interaction

Rudolph Martinez and
Sheila E. Widnall

CONTRACT NSG-2142
October 1981

NASA

NASA CONTRACTOR REPORT 166297

Aeroacoustic Theory for Noncompact Wing-Gust Interaction

Rudolph Martinez and
Sheila E. Widnall
Massachusetts Institute of Technology
Cambridge, Massachusetts 02139

Prepared for
Ames Research Center
under Grant NSG-2142

National Aeronautics and
Space Administration

Ames Research Center
Moffett Field, California 94035

AEROACOUSTIC THEORY FOR NONCOMPACT WING-GUST INTERACTION

By

Rudolph Martinez and Sheila E. Widnall

FDRL Report No. 81-7 October, 1981

This work was supported by NASA Grant NSG-2142. We would also like to acknowledge Profs. Harris' and Landahl's many useful suggestions during the course of this investigation.

This Page Intentionally Left Blank

AEROACOUSTIC THEORY FOR NONCOMPACT WING-GUST INTERACTION

Table of Contents

List of Symbols

$A(\lambda_1)$	function defined in eqn. (4.12)
b	blade semichord
c_o	sound speed
D/Dt	substantial derivative
E, E^*	Fresnel integral, E is conjugate of E
F	integrand factor, eqn. (3.9)
f	acoustic frequency in Hz
G	integrand factor, eqns. (3.8, 3.14)
h	blade-vortex separation
Im	"Imaginary part" of a complex number
I_n	integral defined in eqn. (4.19)
$\tilde{I}_n$	integral defined in eqn. (4.33)
k_x	reduced frequency or chordwise wavenumber
k_y	spanwise wavenumber = $k_x \tan\Lambda$
K	$k_x M/(1-M^2)$
K^*	$\rho_o w_o U\, e^{-i\pi/4} \Big/ (\sqrt{\pi}\sqrt{\frac{k_x}{1-M^2}+\mu})$
L	blade length
L_{max}	maximum sectional lift (lb/ft)
M	freestream Mach number
p, p_*	pressures for 2-D problems
$\bar{P}, P_*$	3-D pressure, and Fourier transform, eqns. (3.5a,b)
$p_*^{(s)}$	correction side-edge pressure, eqns. (4.38, 4.39a,b)
$\bar{p}$	transient signal, eqn. (3.23)
r	assumed form for 3-D upwash, eqns. (4.10a,b)

$\bar{r}$	observer position
Re	"real part" of a complex number
s	characteristic length in chapter 4's theory
t	time
U	subsonic freestream velocity, or flight speed
v	assumed form for 3-D upwash, eqns. (4.10a,b)
w,W	vortex-induced upwash, and Fourier transform
w_o	gust amplitude
x,y,z	chorwise, spanwise, and normal to surface coordinates
Y,Z	$\sqrt{1-M^2}y$, $\sqrt{1-M^2}z$, respectively
Φ,ϕ_*	perturbation velocity potentials
γ,ϕ	angles in spherical coordinate system
Γ	vortex strength (ft^2/sec)
λ_{sound}	acoustic wavelength
μ	$\frac{k_x}{\sqrt{1-M^2}} \left\{ \frac{M^2}{1-M^2} - \tan^2\Lambda \right\}^{1/2}$
ρ_o	freestream density
ω	acoustic frequency in rad/sec
Θ	$\tan^{-1} z/x$
Θ^*	$\tan^{-1}(\sqrt{1-M^2}\tan\Theta)$
τ	source, or retarded time

Superscripts

(1)	solution of leading-edge problem
(2)	solution of trailing-edge problem
(s)	solution of side-edge problem

Subscripts

a	acoustic reference frame
2-D	two-dimensional solution
3-D	three-dimensional solution

Chapter 1: Introduction

The past few decades have seen helicopters evolve into truly multi-purpose machines. In the cities, radio stations use them to provide motorists with valuable traffic information, and in some of the largest they have become just one more form of commuting. In the battlefield, helicopters have proved themselves effective tools in rescue operations, as well as for the transport of troops and supplies to otherwise inaccessible regions. In either role, civilian or military, they are expected to do their job as quietly as possible.

Everyone has heard the unpleasant "slapping" noise from an approaching helicopter. When present, and it often is, in hover, it usually dominates all other sources of helicopter noise - including engine noise. Investigators generally agree[1] that for moderate subsonic tip Mach numbers a great part of each slap signal has its origin in the impulsive load a blade feels upon passage over a vortex trailing from another. For higher tip speeds, however, Boxwell, et. al.[2] have demonstrated experimentally that blade slap can be mostly due another aerodynamic effect: the presence of tip-region shocks on the advancing side of the rotor. Here we develop aeroacoustic models to predict blade slap due to blade-vortex interaction alone.

Normally, heavier helicopters operate faster turning rotors for greater values of needed lift (instead, the number of blades can sometimes be increased). The analysis to

determine the unsteady blade force and associated acoustic field for a blade-vortex interaction at high subsonic tip-Mach numbers is fundamentally different from that for low tip-Mach numbers; compressibility effects then become important in the calculation of a section of the signal's spectrum which may contain a substantial fraction of the signal's acoustic energy. Also, compressibility changes the qualitative character of acoustic radiation: pulses from blade surface dipoles firing at different values of retarted time $t-r/c_0$ may nevertheless reach the far-field point r simultaneously at time t; for high subsonic M, these differences in firing time $\Delta(t-r/c_0)$'s in general are not small in comparison to the period of oscillation of high-level spectral components of the total slap signature. In the present study we develop models to predict theoretically this important part of the signal's spectrum, the part which causes our blade to behave largely as a noncompact acoustic source. We shall see that in the boundary-value problems we need to solve compressibility and high-frequency effects appear lumped in two parameters, both proportional to reduced frequency divided by $1-M^2$.

In the linear models developed here, we split the aeroacoustic problem of blade-vortex interaction into a sum of simpler gust problems; each gust represents a component of the spectrum of the vortex-induced upwash on the plane of flight. It is important to point out that application of our models for blade-gust interaction is not limited to

predictions of noise due to blade-vortex interaction, but that they could also be used, for example, to calculate unsteady forces acting on compressor blades in the presence of nonuniform incident flows, or to predict the acoustic field surrounding a thin wing cutting through confined regions of turbulence.

In earlier theoretical studies of helicopter-blade slap,[3,4] investigators have applied incompressible flow models to calculate unsteady sectional loads acting on a blade passing over a vortex. They used this computed lift force in three-dimensional acoustic models to represent the strength of simple point dipoles along a chosen portion of the blade length. Application of such chordwise-compact aeroacoustic models of blade-vortex interaction to predict noise for practical cases of interest was justified whenever interaction parameters met one of the following two conditions: (1) Large vertical blade-vortex separation to chord ratio for moderate Mach numbers; (2) very low Mach numbers for arbitrary blade-vortex separations.

Actual helicopter blades often operate such that neither of these two compactness criteria is satisfied, however, and noncompact aeroacoustic theories such as those developed here become necessary. The natural uncoupling that exists between an acoustic field and its aerodynamic source (in two-dimensions, the loading along the chord) disappears when the latter is acoustically noncompact; there is no incompressible flow region surrounding the airfoil then, and

the acoustic field begins at the airfoil surface. Instead of radiation from a simple dipole, we expect a more complicated acoustic field due to a distribution of dipoles over the chord with large differences in phase. Kaji has discussed in detail noncompactness effects in ref. 5.

Only a few of many important three-dimensional problems in unsteady aerodynamics have been solved in closed form for subsonic flow; for example, until very recently an unsteady lifting-line theory was not available (ref. 6). Another three-dimensional, but chordwise- compact, model is that due to Chu[7,8], who developed a numerical lifting-surface theory for a semi-infinite blade passing through a gust, and then applied it to predict noise due to blade-vortex interaction. Many past efforts[4,9] in modelling the strength of acoustic sources due to blade-vortex interaction, however, have been based on two-dimensional aerodynamic theories. These models assumed that at most spanwise positions on a blade three-dimensional tip effects can be neglected; they become more and more valid as the vertical blade-vortex separation is reduced and the loading at each section along the length of the blade is dominated two-dimensionally by local chordwise unsteadiness.

Landahl[10] has shown that the surface pressure distribution for a thin two-dimensional airfoil passing subsonically through a gust of arbitrary wavelength may be determined by means of an iterative scheme applied in the aerodynamic reference frame (fixed on the airfoil). In the

first step the chord is allowed to extend infinitely in the downstream direction from the leading edge; this eliminates the Kutta condition and the wake from the problem. The solution to this leading-edge problem satisfies both the upstream boundary condition $\Phi=0$ and the flow tangency boundary condition on the airfoil. A trailing-edge problem is then solved in order to correct the leading-edge solution in the wake. The sum of these two results satisfies flow tangency on the airfoil and pressure continuity across the wake; however it violates the condition of $\Phi=0$ upstream. Further iterations may be carried out to provide a more accurate solution.

Landahl[11] has shown that the series which results from aplication of his iteration scheme converges uniformly; but that due to the strong communication that exists between leading and trailing edges when the gust wavelength is much longer than the airfoil chord, many terms would be needed to obtain a good approximation to a solution which is easily available by simpler methods because the source region is then acoustically compact. Landahl's iteration scheme becomes useful when the gust wavelength is much shorter than the airfoil chord. Then the leading edge and the trailing edge become largely independent of each other, and only a few terms in his series are needed to approximate a solution which is difficult to obtain by any method known because the source region is acoustically noncompact. In the short-wavelength limit the solution is given by the first

term in the series: the relatively simple result from the leading-edge problem.

Adamczyk[12] has also given an infinite-series solution for a two-dimensional airfoil passing through a gust of arbitrary wavelength. His approach was quite different to that of Landahl's and the terms in his series of Mathieu functions cannot be interpreted physically as edge effects. He presented numerical results for some values of the acoustic directivity in the aerodynamic reference frame showing enhancement of the acoustic signal in the downstream direction.

Adamczyk[13] has also determined the response of an infinite-span swept wing to an oblique gust convected by a subsonic freestream. His expression for the pressure distribution on the wing was the sum of the first two terms of the series from the iteration scheme described above. Although he presented numerically calculated loads on an airfoil passing over a potential vortex in this work, he did not report any acoustic results, not even for the gust problem.

Amiet[14] gave numerical results for the power-spectral density of the three-dimensional acoustic far field in the aerodynamic reference frame due the interaction of small-scale turbulence with a high-speed thin wing of finite span. He replaced the surface of the wing with a distribution of point dipoles of strengths given by Adamczyk's two-dimensional response function for a

short-wavelength gust, which he then used in a spanwise superposition to model finite-span effects. His three-dimensional acoustic model for numerical calculations is valid in the high-frequency limit, or alternatively, in the limit of infinite aspect ratio. Amiet[15] has estimated the power-spectral density of the acoustic far field due to a fast climbing rotor cutting through small-scale turbulence. The small-scale character of the turbulence allowed him to consider spanwise blade elements as moving in a locally rectilinear fashion. The results were given in a coordinate system fixed to the rotor hub.

Amiet[16] has also generalized Adamczyk's[13] original two-dimensional high-frequency theory by considering a gust not convected by the freestream. In addition to the gust problem, in this work he also investigated plunging motion of the airfoil; no acoustic analysis was performed, however.

In chapter 2 we develop a two-dimensional aeroacoustic model for a blade of infinite span passing through an oblique gust of short wavelength. We apply Landahl's concept of edge separation and obtain an expression for the pressure field due to the airfoil-gust interaction. The result is approximate because it is the sum of the first two terms in the iteration scheme of edge separation: the first leading-edge solution; and the first trailing-edge solution. Both of these two problems are solved in the aerodynamic reference frame by the Wiener-Hopf technique. The total solution contains the aerodynamics at the airfoil surface,

that is, the surface pressure distribution, and the acoustics of the interaction in a rather compact analytic expression. Letting the field point in the solution come down on the airfoil, we recover Adamczyk's two-dimensional aerodynamic result for the case of zero sweep. Letting the field point go to infinity, we obtain the two-dimensional acoustic field in the airfoil reference frame due to the interaction of an oblique short-wavelength gust with a subsonic airfoil. This section of our presentation is a review of part of the work reported in ref. 9.

In chapter 3 we perform a spanwise superposition of the two-dimensional solution from chapter 2 to approximate the three-dimensional pressure field for a rotating rectangular wing with subsonic tip-Mach number passing through a gust; this last result is given in the acoustic, or ground, reference frame. We calculate the three-dimensional acoustic far field by allowing the observer's coordinates to go to infinity, and obtain a closed-form expression for the acoustic directivity pattern which does not require numerical computation.

In ref. 9 the author performed a spanwise superposition of the two-dimensional result of chapter 2 which is different from the one presented here. The earlier one in ref. 9 is actually valid only in the infinite frequency limit, whereas the one we develop here in chapter 3 is valid for arbitrary high frequencies, not just the infinite limit. As we will see, the analysis in ref. 9 hid some interesting physical

features of the solution for cases in which the disturbance through the fluid has a supersonic trace speed. Also, the three-dimensional model developed in ref. 9 used a "box" spanwise superposition in which inboard blade sections reached the same maximum value of loading as sections near the blade tip. Here we develop a much better model for the unsteady loading on a rotating blade, which in reality sees a freestream linearly increasing from hub to tip: We model the three-dimensional unsteady blade load by the two-dimensional value at the tip, and say that it decreases from this value linearly to zero at the blade hub; the Mach number in the two-dimensional solution is used as the tip-Mach number in the three-dimensional solution.

The actual loading on a helicopter blade, however, vanishes at the tip as $\sqrt{L-y}$, a functional behavior with infinite slope at y=L, where we therefore expect to find generation of strong trailing vorticity. It follows that our aerodynamic superposition model is not consistent with reality near the tip: it overestimates the strength of acoustic dipoles there, and also gives a wrong representation for their phase. As we discussed earlier, however, at high frequencies the spanwise extent of aerodynamic influence of the tip is reduced; blade sections react then mainly to strong local shed vorticity. Acoustic fields predicted by the model in chapter 3 should be good approximations to those we would obtain using a model with correct magnitude and phase of tip dipoles.

Lima[17] has applied the three-dimensional acoustic theory developed in ref. 9 in a study of effects of tip-vortex structure on radiated noise. He used Betz's[18] theory to construct vortices from assumed forms of steady loading on a helicopter blade, and then computed numerically the spectrum of the upwash which each vortex investigated induced on the plane of flight.

In the second section of chapter 3 we apply the leading-edge part of the acoustic theory developed in the first section to calculate the noise signature for the interaction with a potential vortex. The result is given in closed form. It may be used also to predict noise due to the interaction with a real vortex, which has a viscous core. This follows from Widnall's[4] suggestion that the aerodynamic effect of a real vortex may be modelled by a potential vortex at a somewhat larger effective distance below the flight plane.

We also should point out here, as we did in ref. 9, that results equivalent to those obtained by our approach could be reached by an alternate method: By using the airfoil surface pressure distribution already available[13,16] as the strength of point dipoles in a Green's function integral. With the present technique, however, the whole pressure field is obtained at once, so that the solution is both more elegant and compact. Also, the results here in terms of contour integrals make the far-field calculations straightforward and unambiguous. For example, the phases of certain quantities

are always obvious by the present complex-variables method. Finally, our solutions at a general field point may be used immediately to calculate other off-airfoil flow properties of interest besides the acoustic field - the shed vorticity in the wake, for instance.

We have said earlier that for very short wavelengths the blade loading is well approximated by the two-dimensional result only at a distance away from the tip. It turns out, however, that in single-rotor helicopters blade-vortex interactions frequently occur in which only outboard sections of each blade are actually expected to radiate noise. The purpose of chapter 4 is to develop a three-dimensional aeroacoustic model for a blade tip passing through a gust. The objective is to determine the actual magnitude and spanwise phase variation of tip dipoles. Such a tip model should replace chapter 3's whenever conditions of noncompactness prevail, but frequencies are not high enough to ignore three-dimensional tip effects.

Due to the complexity of the problem in general, we consider here the case of a square tip with side edge. Also, since earlier studies[9,13] have demonstrated that in very noncompact situations the trailing edge can be neglected, we simplify the model further: We remove the trailing edge and determine the unsteady pressure field for a quarter-infinite plate with side edge passing through a gust at high subsonic speed.

Miles[19] solved exactly a problem similar to the one we

consider here, but for supersonic flow. For the subsonic flow case no simple procedure yielding an exact closed-form result is available. In chapter 4 we obtain an approximate solution analytically for the pressure field everywhere in space; we apply a procedure similar to that Carrier[20] has used to solve a three-dimensional diffusion problem. By allowing the field point down on the plate's surface we are able, with some work, to obtain a relatively simple expression for the tip loading valid for high frequencies and for large values of the interaction angle Λ. In fact, this load expression turns out to be simple enough to enable us, in chapter 5, to reintroduce the trailing edge into the analysis and so arrive at an aerodynamic model for a rectangular-tip blade of semi-infinite span, with $\sqrt{y}$ side-edge loading behavior, passing through an oblique gust. We then proceed to calculate the associated acoustic field in closed form.

We end this introductory chapter with a very brief qualitative discussion on how we should expect a typical blade-slap signal to look. General acoustic theory[21] tells us that a blade-slap pulse is proportional to the first time derivative of the unsteady blade force induced by the interaction. Fig.1.1a shows a rotor turning at angular speed Ω; the position of rolled-up tip vortices is indicated. Consider the particular blade-vortex interaction for which we have drawn the symbol Λ, for the interaction angle: The position of the vortex relative to the blade at that instant

corresponds to time 1 in fig. 1.1b. Point 1 in fig.1.1c indicates the value of unsteady blade force F(t) at time 1; because its positive part nearly cancels its negative part there, the total load magnitude is relatively small. At time 3, however, F(t) reaches its largest negative value, and its time derivative dF/dt quickly shoots up as the vortex suddenly crosses outboard of the tip. At time 4 the net force is small again.

Chapter 2: Two-dimensional aeroacoustic theory for noncompact blade-gust interaction

In this chapter we apply the concept of separation of leading- and trailing-edge effects at high reduced frequencies to obtain an approximate solution for the two-dimensional pressure field for an infinite-span wing passing through an oblique gust. The result is the sum of the solutions of the first leading- and trailing-edge problems. Before using it to calculate the two-dimensional acoustic field, we bring the field point down to the airfoil surface and recover the expression in ref. 13 for the pressure distribution due to the interaction with the gust; this suggests that our result for the pressure at a general field point in space must be correct. We then proceed to calculate the acoustic field by letting the field point in the solution go to infinity. The resulting expression for the directivity of sound is our contribution to the noncompact two-dimensional theory of airfoil-gust interaction; it first appeared in ref. 9.

Following Amiet's formulation,[16] we have in the aerodynamic reference frame a rigid flat-plate airfoil on the x-y plane with its chord extending from x=0 to x=2. It interacts at an angle Λ with a short-wavelength sinusoidal gust convected by the freestream (fig. 2.1). The linearized equation for the perturbation velocity potential Φ is

$$\Phi_{xx} + \Phi_{yy} + \Phi_{zz} - \frac{1}{c_0^2} \frac{D^2\Phi}{Dt^2} = 0 \qquad (2.1);$$

with boundary conditions

$$\Phi(x<o,y,o,t) = 0 \qquad (2.2a),$$

$$\Phi_z(o<x<2,y,o,t) = -bw(x,y)\, e^{i\omega t} \qquad (2.2b),$$

$$\frac{D\Phi}{Dt}(x\geq 2,y,o,t) = 0 \qquad (2.2c);$$

where the spatial variables have been nondimensionalized with respect to the airfoil semichord b. D/Dt denotes $\partial/\partial t+(U/b)\partial/\partial x$, the linearized substantial derivative. For a sinusoidal gust of small amplitude w_o, the gust downwash $w(x,y)$ becomes $w_o\exp[i(\omega t-k_x x-k_y y)]$; for one convected by the freestream, the nondimensionalized gust wavenumber in the x direction k_x is then $\omega b/U$, the reduced frequency, and the spanwise wavenumber $k_y=(\omega b/U)\tan\Lambda$. Boundary condition (2.2b) is a statement of flow tangency on the airfoil surface. From the linear relation between potential and pressure, i.e., $P=-\rho_o(D\Phi/Dt)$, boundary condition (2.2c) requires that there be no pressure discontinuities at the trailing edge and across the wake.

Since the plate is infinite in the y direction, the potential Φ will have the y dependence of the input gust, a traveling sinusoid; we therefore assume a harmonic behavior

$$\Phi(x,y,z,t)=\phi(x,z)\, e^{i\omega t-ik_y y}$$

according to (2.2b). We also make the change of dependent

variable

$$\phi(x,z) = \phi_{\pm}(x,z)\ e^{\frac{ik_x M^2 x}{1-M^2}}$$

and compress the z coordinate by the change $\sqrt{1-M^2}\,z=Z$. The object of these last two transformations is to reduce the relatively complicated convected wave equation to the more familiar Helmholtz equation.

The boundary-value problem for ϕ_* becomes

$$\phi_{*xx} + \phi_{*_{ZZ}} + \mu^2\phi_* = 0 \qquad (2.3),$$

with

$$\phi_* \ (x<0,0) = 0 \qquad (2.4a),$$

$$\phi_{*Z} \ (0\leq x<2,0) = -\frac{bw_0}{\sqrt{1-M^2}} e^{\frac{-ik_x x}{1-M^2}} \qquad (2.4b),$$

$$\left[\frac{ik_x}{1-M^2} + \frac{\partial}{\partial x}\right] \phi_* \ (x \geq 2,0) = 0 \qquad (2.4c);$$

where

$$\mu^2 = \frac{k_x^2 M^2}{1-M^2} - \frac{k_y^2}{1-M^2} = \frac{k_x^2 \tan^2\Lambda}{(1-M^2)^2}\left[\frac{M^2}{\sin^2\Lambda} - 1\right] = \frac{k_x^2}{1-M^2}\left[\frac{M^2}{1-M^2} - \tan^2\Lambda\right] \qquad (2.4d),$$

and is one of the two wavenumber-related similarity parameters in the problem; the other is $k_x/(1-M^2)$. The parameter μ^2 is negative for $M/\sin\Lambda<1$ $(\tan\Lambda>M/\sqrt{1-M^2})$. This case corresponds physically to a subsonic speed of

propagation of the disturbance due to the passage of the infinite-span wing through the stationary gust. Since a subsonically traveling disturbance of infinite extent radiates no sound, we expect no sound radiation for those Mach number and interaction angle combinations for which μ^2 is negative.

Leading-edge problem

The boundary-value problem for $\phi_*^{(1)}$, the velocity potential field due to the interaction of the gust with a semi-infinite chord airfoil extending downstream from the leading edge, is

$$\phi_{*xx}^{(1)} + \phi_{*ZZ}^{(1)} + \mu^2\phi_*^{(1)} = 0 \qquad (2.5);$$

with

$$\phi_*^{(1)}\ (x<0,0) = 0 \qquad (2.6a),$$

$$\phi_{*_Z}^{(1)}\ (x\geq 0,0) = \frac{-bw_0}{\sqrt{1-M^2}} \exp\left[\frac{-ik_x x}{1-M^2}\right] \qquad (2.6b).$$

The problem may be readily solved by the Wiener-Hopf technique. We define the transform pair

$$\phi_*^{(1)}(x,Z) = \int_C \frac{d\lambda}{\sqrt{2\pi}}\, e^{-i\lambda x}\, \tilde{\phi}(\lambda,Z) \qquad (2.7a),$$

$$\tilde{\phi}\ (\lambda,Z) = \int_{-\infty}^{\infty} \frac{dx}{\sqrt{2\pi}}\, e^{i\lambda x}\, \phi_*^{(1)}(x,Z) \qquad (2.7b);$$

where

$$\tilde{\phi}(\lambda,Z)=\tilde{\phi}_{\ominus}(\lambda,Z) + \tilde{\phi}_{\oplus}(\lambda,Z)$$

that is,

$$\tilde{\phi}_{\ominus}(\lambda,Z) = \int_{-\infty}^{0} \frac{dx}{\sqrt{2\pi}}\, e^{i\lambda x}\, \phi_*(x,Z) \qquad (2.8a),$$

$$\tilde{\phi}_{\oplus}(\lambda,Z) = \int_{0}^{\infty} \frac{dx}{\sqrt{2\pi}}\, e^{i\lambda x}\, \phi_*^{(1)}(x,Z) \qquad (2.8b).$$

The contour C and the regions of analyticity $\ominus$, $\oplus$ in the complex λ plane are yet to be determined by the physical requirement that acoustic waves propagate away from the airfoil, the Sommerfeld radiation condition. Transforming (2.5) and solving the resulting equation, we obtain that for this lifting problem

$$\tilde{\phi}\,(\lambda,Z\pm)= \pm\, \tilde{\phi}\,(\lambda,0^{+})\, e^{\mp\, Z\sqrt{\lambda^2-\mu^2}} \qquad (2.9);$$

where the branch of $\sqrt{\lambda^2-\mu^2}$ is chosen so that its argument vanishes as $|\lambda|$ goes to infinity along C. We initially take μ as a positive constant corresponding to $M/\sin\Lambda>1$. The results may be analytically continued later to include the negative μ^2 case.

Since an $\exp(i\omega t)$ dependence was assumed, outward propagation requires that k_x, and thus also k_y and μ, have a small negative imaginary part. The regions of $\oplus$ and $\ominus$

analyticity in the complex λ plane for (2.8a,b) are then given by $Im(\lambda)>Im(\mu)$, $Im(\lambda)<Im(-\mu)$, respectively, as shown in Fig. 2.2. The contour C runs below the real axis for $Re(\lambda)<Re(-\mu)$ and above the real axis and the point $k_x/(1-M^2)$ for $Re(\lambda)>Re(\mu)$.

From (2.6a,b) and (2.8a,b) the following Wiener-Hopf equation is obtained ($\ominus = \oplus$)

$$\frac{-ibw_0}{\sqrt{2\pi}}\frac{1}{\sqrt{1-M^2}}\frac{1}{(\lambda-\frac{k_x}{1-M^2})}\left\{\frac{1}{\sqrt{\lambda+\mu}}-\frac{1}{\sqrt{\frac{k_x}{1-M^2}+\mu}}\right\}+\frac{1}{\sqrt{\lambda+\mu}}\frac{\partial\tilde{\phi}_{\ominus}(\lambda,o)}{\partial Z}=$$

$$\frac{ibw_0}{\sqrt{2\pi}\sqrt{\frac{k_x}{1-M^2}+\mu}}\frac{1}{(\lambda-\frac{k_x}{1-M^2})}-\sqrt{\lambda-\mu}\;\tilde{\phi}_{\oplus}(\lambda,0+) \qquad (2.10),$$

the left side of (2.10) being a $\ominus$ function and the right a $\oplus$. They are, therefore, analytic continuations of each other and so they are both at least entire functions of λ. If $\tilde{\phi}$, $\partial\tilde{\phi}/\partial Z$ are assumed to be well behaved a $\lambda=\infty$, (the Riemann-Lebesgue lemma) Liouville's theorem then states that both sides of (2.10) are independently equal to zero. The right side of the equality says that

$$\tilde{\phi}(\lambda,o^+)=\frac{ibw_o}{\sqrt{2\pi}}\frac{1}{\sqrt{1-M^2}}\frac{1}{\sqrt{\frac{k_x}{1-M^2}+\mu}}\frac{1}{\sqrt{\lambda-\mu}}\frac{1}{(\lambda-\frac{k_x}{1-M^2})} \qquad (2.11);$$

and so, from (2.9) and (2.7a)

$$\phi_{\pm}^{(1)}(x,Z)=\frac{ibw_o}{2\pi\sqrt{1-M^2}}\frac{Z/|Z|}{\sqrt{\frac{k_x}{1-M^2}+\mu}}\int_C\frac{d\lambda\; e^{-i\lambda x-|Z|\sqrt{\lambda^2-\mu^2}}}{\sqrt{\lambda-\mu}}\frac{1}{(\lambda-\frac{k_x}{1-M^2})} \qquad (2.12).$$

Arguments similar to those made for the time and y dependence of the velocity potential also apply to the pressure. Making the same changes of dependent and independent variables made before for the potential, we have

$$P(x,y,z,t) = p(x,z)\, e^{i\omega t - ik_y y} \qquad (2.13a),$$

$$p(x,z) = p_*(x,Z)\, \exp\left[\frac{ik_x M^2 x}{1-M^2}\right] \qquad (2.13b).$$

From the relationship between pressure and velocity potential, the pressure $p_*^{(1)}(x,Z)$ corresponding to $\phi_*^{(1)}(x,Z)$ is obtained:

$$p_*^{(1)}(x,Z) = -\frac{\rho_\infty w_0 U}{2\pi\sqrt{1-M^2}} \frac{Z/|Z|}{\sqrt{\frac{k_x}{1-M^2}+\mu}} \int_C \frac{d\lambda}{\sqrt{\lambda-\mu}}\, e^{i\lambda x - |Z|\sqrt{\lambda^2-\mu^2}} \qquad (2.14).$$

For $x>0$, $Z=0+$, the contour C may be deformed to C^* in fig. 2.3 so that

$$p_*^{(1)}(x>0,0^{\pm}) = \frac{\mp \rho_\infty w_0 U}{\sqrt{\pi}\sqrt{1-M^2}} \frac{1}{\sqrt{\frac{k_x}{1-M^2}+\mu}} \frac{e^{-\frac{i\pi}{4} - i\mu x}}{\sqrt{x}} \qquad (2.15),$$

in agreement with the aerodynamic result in ref. 13.

Trailing-edge problem

The solution to the trailing-edge problem is a pressure $p_*^{(2)}$ such that $p_*^{(1)}+p_*^{(2)}$ is zero at the trailing edge and in the wake. From the linear relation between potential and pressure, we note that $p_*^{(2)}(x,Z)$ also satisfies Helmholtz's

equation. We also require that $\partial p_*^{(2)}/\partial Z$ vanish upstream of the trailing edge and that it be continuous for all x. With $x=x'+2$, the trailing-edge correction boundary-value problem for $p_*^{(2)}$ in the x'-Z coordinate system is

$$p_{*x'x'}^{(2)} + p_{*ZZ}^{(2)} + \mu^2 p_*^{(2)} = 0 \qquad (2.16);$$

with

$$\frac{\partial p_*^{(2)}}{\partial Z}\,(x'+2,0) = 0 \text{ for } x'<0 \qquad (2.17a),$$

$$p_*^{(2)}\,(x'+2,0^{\pm}) = -\,p_*^{(1)}\,(x'+2,0^{\pm}) \text{ for } x'>0 \qquad (2.17b).$$

This problem may also be solved by the Wiener-Hopf technique. We define the transform pair

$$p_*^{(2)}\,(x',Z) = \int_C \frac{d\lambda}{\sqrt{2\pi}}\, e^{-i\lambda x}\,\tilde{p}(\lambda,Z) \qquad (2.18a),$$

$$\tilde{p}\,(\lambda,Z) = \int_{-\infty}^{\infty} \frac{dx'}{\sqrt{2\pi}}\, e^{i\lambda x'}\, p_*^{(2)}\,(x',Z) \qquad (2.18b);$$

where $\tilde{p} = \tilde{p}_{\ominus} + \tilde{p}_{\oplus}$; that is,

$$\tilde{p}_{\ominus}(\lambda,Z) = \int_{-\infty}^{0} d\xi e^{i\lambda\xi}\, p_*^{(2)}\,(\xi,Z) \qquad (2.19a),$$

$$\tilde{p}_{\oplus}(\lambda,Z) = \int_{0}^{\infty} d\xi e^{i\lambda\xi}\, p_*^{(2)}\,(\xi,Z) \qquad (2.19b).$$

Transforming (2.16), solving the resulting equation and

invoking the continuity of $\partial p_*^{(2)}/\partial Z$ for all x', we obtain

$$\tilde{p}(\lambda, Z^{\pm}) = \pm \tilde{P}(\lambda, 0^+)\, e^{\mp Z\sqrt{\lambda^2-\mu^2}} \qquad (2.20);$$

where $\tilde{P}(\lambda,0+)=\tilde{P}_{\ominus}(\lambda,0+)+\tilde{P}_{\oplus}(\lambda,0+)$, the arbitrary function of λ to be determined by the Wiener-Hopf technique.

From boundary condition (2.17a), we see that $\partial\tilde{P}_{\ominus}(\lambda,0)/\partial Z=0$. From boundary condition (2.17b), and recalling the result in (2.15), $\tilde{P}_{\oplus}(\lambda,0^{\pm})$ may be calculated:

$$\tilde{P}_{\oplus}(\lambda,0^{\pm}) = \pm \frac{K^* e^{-i2\lambda}}{\sqrt{\lambda-\mu}} \left\{ \frac{e^{i\pi/4}}{\sqrt{2}} - E\left[2(\lambda-\mu)\right] \right\} \qquad (2.21);$$

where $E(a)=\int_0^a \frac{dt\, e^{it}}{\sqrt{2\pi t}}$ a Fresnel integral; $E[2(\lambda-\mu)]$ therefore has a branch point at $\lambda=\mu$.

The Wiener-Hopf equation in this case is ($\ominus=\oplus$)

$$\sqrt{\lambda+\mu}\,\tilde{P}_{\ominus}(\lambda,0+)+K^*\left[\sqrt{\frac{\lambda+\mu}{\lambda-\mu}}\; e^{-2i\lambda}\left\{\frac{e^{i\pi/4}}{\sqrt{2}} - E\,[2(\lambda-\mu)]\right\}\right.$$

$$\left. - \frac{e^{-i\pi/4}}{\pi\sqrt{2}} \int_{\mu}^{\infty} \frac{d\xi}{\xi-\lambda}\sqrt{\frac{\xi+\mu}{\xi-\mu}}\; e^{-2i\xi}\right] = -\frac{1}{\sqrt{\lambda-\mu}}\,\frac{\partial\tilde{P}_{\oplus}}{\partial Z}(\lambda,0+) - K^*\, f_{\oplus}(\lambda) \qquad (2.22);$$

where

$$K^* = \frac{\rho_a W_o\, U\, e^{-i\pi/4}}{\sqrt{\pi}\sqrt{\frac{k_x}{1-M^2}+\mu}}\,\frac{1}{\sqrt{1+M^2}}$$

a constant, and $K^* f_{\oplus}$ denotes that additive part of $\sqrt{\lambda+\mu}\,\tilde{P}_{\oplus}(\lambda,0+)$ which is analytic in the upper half λ plane. The standard procedure of splitting an arbitrary function into a sum of two, one $\ominus$ and the other $\oplus$, is treated in detail in

ref. 22. Making the usual assumptions regarding the good behavior of $\tilde{P}_{\ominus}(\lambda,0+)$ and $\partial\tilde{P}_{\oplus}(\lambda,0)/\partial Z$, we have that (Liouville's theorem) both sides of (2.22) vanish independently. This gives $\tilde{P}_{\ominus}(\lambda,0+)$. Adding (2.21) to it, we obtain $\tilde{P}(\lambda,0+)$, and substituting into (2.20) and by means of (2.18a), we finally have that

$$p_*^{(2)}(x,Z) = -\frac{i\rho_0 w_0 U}{2\pi^2\sqrt{1-M^2}} \frac{Z/|Z|}{\sqrt{\frac{kx}{1-M^2}+\mu}} \int_C \frac{d\lambda}{\sqrt{\lambda+\mu}} e^{-i\lambda(x-2)-|Z|\sqrt{\lambda^2-\mu^2}} \int_\mu^\infty \frac{d\xi}{\xi-\lambda}\sqrt{\frac{\xi+\mu}{\xi-\mu}}\, e^{-2i\xi} \qquad (2.23);$$

where the contour C is indented above the real axis at $\lambda=\xi$.

Total Solution

Adding (2.14) and (2.23) and applying (2.13b), we obtain the two-term approximation to the two-dimensional pressure field for the passage of an infinite-span wing through an oblique gust

$$p(x,z) \cong p^{(1)}(x,z) + p^{(2)}(x,z) \qquad (2.24).$$

The pressure distribution on the airfoil, with its chord extending from x=0 to x=2, is calculated from (2.24) which now says that

$$p(0<x<2,0+) \cong p^{(1)}(x>0,0^+) + p^{(2)}(x<2,0^+) \qquad (2.25).$$

The part $p^{(1)}(x>0,0+)$ has already been determined and is given by (2.15) and (2.13b). To obtain $p^{(2)}(x<2,0+)$, we start

with (2.23) and observe that for Z=0+, x<2, the integral

$$I(\mu,x,Z^+) = \int_C \frac{d\lambda}{\sqrt{\lambda+\mu}} e^{-i\lambda(x-2)-Z\sqrt{\lambda^2-\mu^2}} \int_\mu^\infty \frac{d\xi}{\xi-\lambda}\sqrt{\frac{\xi+\mu}{\xi-\mu}}\, e^{-2i\xi} \qquad (2.26)$$

may be deformed to

$$I(\mu,x,0+) = \int_{C^{**}} \frac{d\lambda}{\sqrt{\lambda+\mu}} e^{-i\lambda(x-2)} \int_\mu^\infty \frac{d\xi}{\xi-\lambda}\sqrt{\frac{\xi+\mu}{\xi-\mu}}\, e^{-2i\xi} \qquad (2.27);$$

where the contour C^{**} is shown in fig. 2.4.

Interchanging orders of integration we have

$$I(\mu,x,0+) = -\int_\mu^\infty d\xi \sqrt{\frac{\xi+\mu}{\xi-\mu}}\, e^{-2i\xi} \int_{C^{**}} \frac{d\lambda\, e^{-i\lambda(x-2)}}{\sqrt{\lambda+\mu}} \frac{1}{(\lambda-\xi)} \qquad (2.28).$$

The term $1/(\lambda-\xi)$ attains its maximum magnitude of $-1/2\mu$ when $\xi=\mu$ and $\lambda=-\mu$. and goes to zero as $\xi\to\infty$ or as $\lambda\to-\infty$ along C^{**}, or both. We can expect then that the largest contribution to $I(\mu,x,0)$ comes from values of ξ near the lower limit. We therefore make the following approximation:

$$I(\mu,x,0+) \cong -\sqrt{2\mu}\, e^{-i\mu(x-2)} \int_\mu^\infty \frac{d\xi\, e^{-2i\xi}}{\sqrt{\xi-\mu}} \int_{C^{**}} \frac{d\lambda\, e^{-i(\lambda-\mu)(x-2)}}{\sqrt{\lambda+\mu}} \frac{1}{(\lambda-\mu)}$$

$$= (1-i)\pi^{3/2}\, e^{-i\mu x} \{1-(1+i)\, E^*[2\mu(2-x)]\} \qquad (2.29);$$

where E^* is the complex conjugate of E as defined in (2.21). Substituting for $I(\mu,x,0+)$ in $p_*^{(2)}(x<2,0+)$, we have

$$p_*^{(2)}(x<2,0+) \cong \frac{\rho_0 w_0 U}{\sqrt{2\pi}\sqrt{1-M^2}} \frac{e^{-i\pi/4 - i\mu x}}{\sqrt{\frac{k_x}{1-M^2}+\mu}} \{1-(1+i)E^*[2\mu(2-x)]\} \quad (2.30);$$

from which (2.25) becomes

$$p(0<x<2,0+) \cong \mp \frac{\rho_0 w_0 U}{\sqrt{\pi}\sqrt{1-M2}} \frac{1}{\sqrt{\frac{k_x}{1-M2}+\mu}} e^{i\frac{k_x M^2}{1-M^2}x - i\mu x - \frac{i\pi}{4}}$$

$$\left\{\frac{1}{\sqrt{x}} - \frac{1}{\sqrt{2}}\left[1-(1+i)\,E^*\,[2\mu(2-x)]\right]\right\} \quad (2.31);$$

so that the Kutta condition is satisfied at x=2 as required. The result in (2.31) agrees with that given in ref. 13 for the pressure distribution on an infinite-span wing passing through an oblique short-wavelength gust. It serves as a check for the expression in (2.24) that we have derived for the pressure p(x,Z) at a general field point.

Two-dimensional acoustic far field in the airfoil frame of reference

Here we start with the two-dimensional pressure field P(x,y,Z,t) due to the passage of an infinite-span wing through an oblique gust as given by (2.24) and (2.13a). We determine the two-dimensional far field in the airfoil reference frame by allowing the field point to go to infinity. The calculated directivity of sound is theoretically that which would be measured in a wind tunnel experiment.

From (2.24) and (2.13a) we have

$$P(x,y,Z,t) = -\frac{\rho_0 w_0 U}{2\pi\sqrt{1-M^2}}\frac{Z/|Z|}{\sqrt{\frac{k_x}{1-M^2}+\mu}}\, e^{i\omega t - ik_y y + \frac{ik_x M^2 x}{1-M^2}}$$

$$\int_C d\lambda \left\{ \frac{1}{\sqrt{\lambda-\mu}} + \frac{i\, e^{2i\lambda}}{\pi\sqrt{\lambda+\mu}} \int_\mu^\infty \frac{d\xi}{\xi-\lambda}\sqrt{\frac{\xi+\mu}{\xi-\mu}}\, e^{-2i\xi} \right\} e^{-i\lambda x - |Z|\sqrt{\lambda^2-\mu^2}} \quad (2.32).$$

We notice that in order to obtain a nonvanishing far field the largest contribution to $P(x,y,Z,t)$ as $\sqrt{x^2+Z^2}\to\infty$ must come from values of λ such that $\sqrt{\lambda^2-\mu^2}<0$ or $|\lambda|<\mu$, and so it follows that in the far field, the largest contribution to the inside integral in (2.32) comes from its lower limit. Integrating by parts, we thus obtain that as $\sqrt{x^2+Z^2}\to\infty$

$$\int_\mu^\infty \frac{d\xi}{\xi-\lambda}\sqrt{\frac{\xi+\mu}{\xi-\mu}}\, e^{-2i\xi} \sim \frac{\pi\sqrt{2\mu}}{\sqrt{\mu-\lambda}}\, e^{-2i\lambda}\{1-(1+i)E^*[2(\mu-\lambda)]\} \quad (2.33).$$

Substituting this into (2.32), the asymptotic behavior of the λ integral as $\sqrt{x^2+Z^2}\to\infty$ may be determined by steepest descents (Noble,[23] pp. 33-36) to be

$$\frac{P(x,y,z,t)}{\sqrt{x^2+z^2}\to\infty} \sim \frac{\rho_0 w_0 U}{\sqrt{\pi}\sqrt{1-M^2}} \frac{e^{i\omega t - ik_y y - \frac{i\pi}{4} - \frac{ik_x M^2\cos\theta}{1-M^2} - i\mu\sqrt{1-M^2\sin^2\theta}\sqrt{x^2+z^2}}}{\sqrt{\frac{k_x}{1-M^2}+\mu}\;\frac{1}{(x^2+z^2)^{1/4}}}$$

$$\left\{ \frac{1-\cos(\Theta^*/2) - (1+i)E^*[2\mu(1-\cos\theta^*)]}{(1-M^2\sin^2\theta)^{1/4}} \right\} \quad (2.34);$$

where the substitution $Z=\sqrt{1-M^2}z$ has been made so that $\theta=\tan^{-1}(z/x)$ and $\Theta^*=\tan^{-1}(\sqrt{1-M^2}\tan\Theta)$. The expression in (2.34) shows that for negative μ^2 ($\mu=-i\sqrt{-\mu^2}$) there is no acoustic

field (the solution in (2.34) is exponentially damped). We had anticipated that this should be the case since the disturbance due to the passage of the infinite-span wing through the gust then travels subsonically through the fluid. The quantity in brackets is the two-dimensional acoustic directivity $D(\theta)$ in the airfoil reference frame; we plot it for different values of the Mach number M in figs. 2.5a,b. For values of 1 foot for the semichord b and 1100 ft/sec for the sound speed c_o, the acoustic signals corresponding to these patterns are sound tones of 280 and 315 Hz, respectively.

We can appreciate the dramatic effect of noncompactness on acoustic radiation if while we look at these we recall the directivity pattern for a simple dipole - the acoustic field for a compact region. Note the sensitivity of the lobing to a relatively small change in Mach number. The parameter which actually controls the amount of noncompactness of course is μ, which lumps frequency and compressibility effects together and without which the Helmholtz equation (2.3) becomes the Laplacian, the governing equation for compact aerodynamic regions; it appears alone in the directivity part of (2.34).

Amiet[16] and Adamczyk[13] have compared the predicted aerodynamic loading (2.31) to numerical results obtained by Graham[24] for a wide range of μ values. They have determined that the two-term theory (one leading- and trailing-edge problem) gives good results for loading when $\mu > .7$,

approximately, for μ real. For imaginary μ (2.31) remains valid in a wider range, apparently because the trailing-edge part of the loading converges then much faster; the Fresnel integral turns into an Error function and the loading becomes hydrodynamic in character.

Chapter 3: Approximate aeroacoustic model for a rotating blade of finite span passing through a gust. Application for a potential vortex

In chapter 2 we derived an expression for the pressure field everywhere in space for the two-dimensional interaction of a subsonic infinite-span airfoil with an oblique gust. In this chapter we use that two-dimensional solution in a superposition procedure which will enable us to model the three-dimensional acoustic field radiated by a rectangular blade rotating with high subsonic tip-Mach number. We find that when the disturbance due to the interaction travels supersonically through the fluid, the model breaks down along certain directions. For cases of subsonic trace speed of the disturbance, we present typical examples of acoustic directivity patterns and compare one case to the corresponding two-dimensional result in chapter 2.

Amiet[15] has pointed out that the contribution to the acoustic field from the acceleration effect of sources of sound on a rotating blade may be neglected when ω, the acoustic frequency, is much larger than Ω, the blade angular speed. Our three-dimensional model for the acoustic field uses this simplifying fact, and so we assume that each spanwise section of the blade passes rectilinearly through the gust with local speed varying from hub to tip.

In addition, the associated three-dimensional aerodynamic model makes the following two related assumptions: (1) the chordwise unsteadiness dominates the three-dimensional tip effect over all of the span; and (2)

that the spanwise loading may adequately modelled by a triangular shape with maximum loading at the tip (in reality the actual loading near the tip must vanish as $\sqrt{L-y}$).

We close the chapter by applying the leading-edge part of our result to predict acoustic signatures for the interaction with a potential vortex. The vortex in the model is located a distance h chords below the flight plane.

We start by defining the three-dimensional pressure field $P_{3\text{-}D}(x,y,Z,t)$ due to the passage of a rotating blade of span L through an oblique gust; as before $Z=\sqrt{1-M^2}\,z$. We require that this three-dimensional pressure equal the two-dimensional pressure P given in (2.32) on Z=0+, y=L, and that it decrease from this value to zero linearly at Z=0+, y=0. We make the changes

$$P_{3\text{-}D}(x,y,Z,t) = P_* (x,y,Z)\, e^{i\omega t + \frac{ik_x M^2}{1-M^2}x} \qquad (3.1),$$

and $Y=\sqrt{1-M^2}\,y$ so that P_* satisfies

$$P_{*xx} + P_{*YY} + P_{*ZZ} + \left(\frac{k_x M}{1-M^2}\right)^2 P_* = 0 \qquad (3.2)$$

subject to the boundary condition

$$P_*(x,Y,0+) = \begin{cases} \dfrac{Y}{L\sqrt{1-M^2}}\; P_{*2\text{-}D}\,(x,Y,0+) & \text{for } 0<Y<\sqrt{1-M^2}\,L \\ 0 & \text{otherwise} \end{cases} \qquad (3.3),$$

where

$$P_{*2\text{-}D}\,(x,Y,0+) = \frac{-\rho_0 w_0 U}{2\pi\sqrt{1-M^2}} \frac{1}{\sqrt{\frac{k_x}{1-M^2}+\mu}}\, e^{\frac{-ik_x \tan\Lambda Y}{\sqrt{1-M^2}}}$$

$$\int_C d\lambda e^{-i\lambda x}\left\{\frac{1}{\sqrt{\lambda-\mu}} + \frac{ie^{2i\lambda}}{\pi\sqrt{\lambda+\mu}}\int_\mu^\infty \frac{d\xi}{\xi-\lambda}\sqrt{\frac{\xi+\mu}{\xi-\mu}}\, e^{-2i\xi}\right\} \qquad (3.4).$$

as may be seen from eqn. (2.32).

We now define the transform pair

$$P_*(x,Y,Z) = \int_{-\infty}^{\infty}\int \frac{d\lambda_1 d\lambda_2}{(2\pi)^2}\, e^{-i\lambda_1 x - i\lambda_2 Y}\, \bar{P}(\lambda_1,\lambda_2;Z) \qquad (3.5a),$$

$$\bar{P}(\lambda_1,\lambda_2;Z) = \int_{-\infty}^{\infty}\int dx\, dY\, e^{i\lambda_1 x + i\lambda_2 Y}\, P_*(x,Y,Z) \qquad (3.5b).$$

Transforming (3.2) and solving, we obtain that

$$\bar{P}(\lambda_1,\lambda_2;Z\pm) = \pm\,\bar{P}(\lambda_1,\lambda_2,0+)\; e^{\mp Z\sqrt{\lambda_1^2+\lambda_2^2-K^2}} \qquad (3.6),$$

where we have called $k_x M/(1-M^2) \equiv K$, for convenience. From (3.5b) and (3.4) it follows that

$$\bar{P}(\lambda_1,\lambda_2,0+) = F(\lambda_1)\, G\left(\lambda_2 - \frac{k_x \tan\Lambda}{\sqrt{1-M^2}}\right) \qquad (3.7),$$

where

$$G\left(\lambda_2 - \frac{k_x\tan\Lambda}{\sqrt{1-M^2}}\right) = \int_0^{\sqrt{1-M^2}L} \frac{dY}{L}\frac{Y}{\sqrt{1-M^2}}\, e^{i\left(\lambda_2 - \frac{k_x\tan\Lambda}{\sqrt{1-M^2}}\right)Y} \qquad (3.8),$$

and

$$F(\lambda_1) = -\frac{\rho_0 w_0}{\sqrt{1-M^2}}\frac{\mu}{\sqrt{\frac{k_x}{1-M^2}+\mu}}\left\{\frac{1}{\sqrt{\lambda_1-\mu}} + \frac{i\,e^{2i\lambda_1}}{\pi\sqrt{\lambda_1+\mu}}\int_\mu^\infty \frac{d\xi}{\xi-\lambda_1}\sqrt{\frac{\xi+\mu}{\xi-\mu}}\, e^{-2i\xi}\right\} \qquad (3.9).$$

From (3.7), (3.6), (3.4a), and (3.1) we have therefore

that
$$P_{3\text{-}D}(x,Y,Z,t) = e^{i\omega t} + \frac{ik_x M^2 x}{1-M^2} \int_{-\infty}^{\infty}\int \frac{d\lambda_1 d\lambda_2}{(2\pi)^2} e^{-\lambda_1 x - i\lambda_2 Y - Z\sqrt{\lambda_1^2+\lambda_2^2-K^2}} F(\lambda_1)\, G\left(\frac{\lambda_2 - k_x \tan\Lambda}{\sqrt{1-M^2}}\right) \quad (3.10).$$

We now translate the solution in (3.10) from the airfoil frame of reference to the ground, or acoustic, reference frame. We let $\lambda_1 = b\tilde{\lambda}_1 + k_x M^2/(1-M^2)$, $\lambda_2 = b\tilde{\lambda}_2/\sqrt{1-M^2}$, and express the result in (3.10) in terms of the original unstretched y, z variables. We also introduce a ω' -t Fourier transform so that

$$P_{3\text{-}D}(x,Y,Z,t) = \int_{-\infty}\int \frac{b^2 d\tilde{\lambda}_1 d\tilde{\lambda}_2}{(2\pi)^2} \int_{-\infty}^{\infty} d\omega' e^{i\omega' t - i\tilde{\lambda}_1 bx - i\tilde{\lambda}_2 by}$$
$$\exp\left(-ibz\sqrt{\frac{\omega'^2}{c_0^2} - \tilde{\lambda}_1^2 - \tilde{\lambda}_2^2}\right) \delta[\omega' - (\omega - \tilde{\lambda}_1 U)]\, F\left(b\tilde{\lambda}_1 + \frac{k'_x M^2}{1-M^2}\right) G\left(\frac{b\tilde{\lambda}_2 - k'_x \tan\Lambda}{\sqrt{1-M^2}}\right) \quad (3.11),$$

where $k'_x = (\omega + \tilde{\lambda}_1 U)b/U$. Next, we express the δ-function appearing in (3.11) in terms of one of its well known limiting forms, e.g., $\delta(a) = \lim_{\varepsilon\to 0} \frac{1}{\pi}\frac{a}{\varepsilon^2 + a^2}$ and interchange the orders of $\tilde{\lambda}_1, \tilde{\lambda}_2$ integration with the ω' integral:

$$P_{3\text{-}D}(x_a,y,z,t) = \lim_{\varepsilon\to 0} \frac{b^2}{(2\pi)^2} \int_{-\infty}^{\infty} d\omega' e^{i\omega' t} \int_{-\infty}\int d\tilde{\lambda}_1 d\tilde{\lambda}_2 e^{-i\tilde{\lambda}_1 bx_a - i\tilde{\lambda}_2 by}$$
$$e^{-ibz\sqrt{\frac{\omega'^2}{c_0^2} - \tilde{\lambda}_1^2 - \tilde{\lambda}_2^2}} \frac{1}{\pi} \frac{[\omega' - (\omega - \tilde{\lambda}_1)U]}{\{\varepsilon^2 + [\omega' - (\omega - \lambda_1 U)]^2\}} F\left(b\tilde{\lambda}_1 + \frac{k'_x M^2}{1-M^2}\right) G\left(\frac{b\tilde{\lambda}_2 - k'_x \tan\Lambda}{\sqrt{1-M^2}}\right) \quad (3.12).$$

Here $bx_a = bx - Ut$, the "a" subscript denoting the acoustic reference frame. The last step is to evaluate $P_{3\text{-}D}$ in the far

field; this may be readily done by approximating the $\tilde{\lambda}_1$, $\tilde{\lambda}_2$ integrals using the method of stationary phase (Whitham,[25] p. 392). Before we do this, however, we may use the approximation indicated in (2.33) for the integral appearing in F in (3.9). The final result for the sound signal in the three-dimensional acoustic field which a listener on the ground hears as the rotating blade of span L and tip Mach number M passes through a stationary gust of short wavelength is

$$P_{3\text{-}D}(x,y,z,t) = \frac{-i\rho_0 w_0}{2\pi(1-M^2)^{1/4}} \frac{\sqrt{k_x}}{\sqrt{\frac{k_x}{1-M^2}+\mu}} \frac{e}{r_a} \frac{i\omega}{1+M\frac{x_a}{r_a}}\left(t-\frac{br_a}{c_0}\right) \frac{D_{3\text{-}D}\left(\frac{x_a}{r_a}, \frac{y}{r_a}, \frac{z}{r_a}\right)}{\left(1+M\frac{x_a}{r_a}\right)^2} \quad UM \tag{3.13}$$

where

$$D_{3\text{-}D}\left(\frac{x_a}{r_a}, \frac{y}{r_a}, \frac{z}{r_a}\right) = \frac{z}{r_a}\left\{\frac{1}{\left[\frac{M}{\sqrt{1-M^2}}\left(\frac{\frac{x_a}{r_a}+M}{1+M\frac{x_a}{r_a}}\right) - \sqrt{\frac{M^2}{1-M^2}-\tan^2\Lambda}\right]^{1/2}}\right.$$

$$+ \frac{i\sqrt{2}\left\{\frac{M^2}{1-M^2}-\tan^2\Lambda\right\}^{1/4}}{\left\{\frac{M^2}{\sqrt{1-M^2}}-\tan^2\Lambda-\left[\frac{M}{\sqrt{1-M^2}}\left(\frac{\frac{x_a}{r_a}+M}{1+M\frac{x_a}{r_a}}\right)\right]^2\right\}^{1/2}}\left\{1-(1+i)\right.$$

$$\left.\left.E^*\left[\frac{2k_x}{\sqrt{1-M^2}}\left(\sqrt{\frac{M^2}{1-M^2}-\tan^2\Lambda} - \frac{M\left(\frac{x_a}{r_a}+M\right)}{\sqrt{1-M^2}\left(1+M\frac{x_a}{r_a}\right)}\right)\right]\right\}\right\} \frac{G\left[k_x\left(\frac{My/r_a}{1+M\frac{x_a}{r_a}}-\tan\Lambda\right)\right]}{\sqrt{1-M^2}} \tag{3.14a}$$

and

$$\frac{1}{\sqrt{1-M^2}}\, G\left[k_x\left(\frac{My/r_a}{1+M\frac{x_a}{r_a}} - \tan\Lambda\right)\right] = \frac{e^{-ik_xL\left(\tan\Lambda - \frac{My/r_a}{1+M\frac{x_a}{r_a}}\right)} - 1}{L\left(k_x\left[\tan\Lambda - \frac{My/r_a}{1+M\frac{x_a}{r_a}}\right]\right)^2}$$

$$+ \frac{i\, e^{-i\,k_xL\left(\tan\Lambda - \frac{My/r_a}{1+M\frac{x_a}{r_a}}\right)}}{k_x\left(\tan\Lambda - \frac{My/r_a}{1+M\,x_a/r_a}\right)} \qquad (3.14b).$$

The distance $r_a=\sqrt{x_a^2+y^2+z^2}$ and the direction cosines x_a/r_a, y/r_a, z/r_a specify the position of the observer on the ground. $D_{3\text{-}D}(x_a/r_a, y/r_a, z/r_a)$ is the three-dimensional acoustic directivity not including the factor $(1+Mx_a/r_a)^{-2}$ which gives the usual forward enhancement of the acoustic signal from a moving source, in this case, the blade traveling in the $-x_a$ direction; $1+Mx_a/r_a$ also represents the position-dependent Doppler shift of the tone, as indicated in the exponential in (3.13).

The expressions in (3.13), (3.14a) stand as are for $M/\sin\Lambda>1$ ($\tan\Lambda<M/\sqrt{1-M^2}$), that is, for supersonic trace speeds of the disturbance. For subsonic trace speeds, $\sin\Lambda>M$, and we recall from chapter 2 that $\mu=-i\sqrt{-\mu^2}$, so that may then write

$$\sqrt{\frac{M^2}{1-M^2} - \tan^2\Lambda} = -i\sqrt{\tan^2\Lambda - \frac{M^2}{1-M^2}}$$

in (3.13), (3.14a). Before we make this change for the subsonic cases, however, we notice that the first term inside brackets in (3.14a), the contribution from the leading-edge problem, blows up in the direction given by

$$\left.\frac{x_a}{r_a}\right|_1 = -\left[\frac{\frac{M^2}{\sqrt{1-M^2}} - \sqrt{\frac{M^2}{1-M^2} - \tan^2\Lambda}}{\frac{M}{\sqrt{1-M^2}} - M\sqrt{\frac{M^2}{1-M^2} - \tan^2\Lambda}}\right] \qquad (3.15).$$

As fig. 3.1 shows, this is the direction taken by acoustic rays born at the line formed by the intersection of the downstream part of a typical Mach cone and the x_a-y plane. The breakdown of the leading-edge solution in this direction can be explained mathematically as follows: Since the chord extends downstream to infinity, in the above operations we have in fact tried to calculate the acoustic field of a distribution of supersonic sources which is infinite in extent; the surfaces of the associated system of Mach cones do not interfere and so, even those farthest from the leading edge will have an acoustic effect. But the determination of such an acoustic field is a badly posed problem for the method of stationary phase, which relies on the existence of a single point in physical space (and also in wavenumber space) where the acoustic effect of the entire source distribution may be modelled by one equivalent source of arbitrary complexity.

Similarly, we notice that the second term in brackets in (3.14a), the contribution from the trailing-edge problem, blows up along two different directions: one of these is given in (3.15), and the other by the solution of

$$\sqrt{\frac{M^2}{1-M^2} - \tan^2\Lambda} + \frac{M}{\sqrt{1-M^2}} \frac{\left(\frac{x_a}{r_a} + M\right)}{\left(1+M\frac{x_a}{r_a}\right)} = 0$$

which is

$$\left.\frac{x_a}{r_a}\right|_2 = -\left[\frac{\frac{M^2}{\sqrt{1-M^2}} + \sqrt{\frac{M^2}{1-M^2} - \tan^2\Lambda}}{\frac{M}{\sqrt{1-M^2}} + M\sqrt{\frac{M^2}{1-M^2} - \tan^2\Lambda}}\right] \qquad (3.16).$$

They are the directions of acoustic propagation from the two lines formed by the intersection of the Mach cones and the x_a-y plane. That the trailing-edge part of the solution breaks down in both directions should not surprise us if we recall that although it was constructed to cancel the leading-edge result in the wake, it was also nonzero (though small) upstream of the plate. Since the trailing-edge solution cancels the leading-edge solution in the wake, however, we would expect it to cancel also the breakdown because, in effect, it changes the leading edge's region of semi-infinite extent - the blade chord plus the wake, into one of finite extent - just the blade chord. Below we verify that this is in fact the case. Unfortunately, we still end up with a part of the trailing-edge solution which breaks down in the upstream direction given by (3.16); to correct it, a second leading-edge problem would have to be solved. But even then our problems would not be over, for we would still have a semi-infinite region of supersonic sources, now in the downstream direction.

In the direction given by (3.15), we find that

$$\frac{1}{\left\{\frac{M^2}{1-M^2} - \tan^2\Lambda - \left[\frac{M}{\sqrt{1-M^2}}\,\frac{\left(\frac{x_a}{r_a}+M\right)}{\left(1+M\,\frac{x_a}{r_a}\right)}\right]^2\right\}^{1/2}} \cong$$

$$\frac{1}{\sqrt{2}\left\{\frac{M^2}{1-M^2} - \tan^2\Lambda\right\}^{1/4}\left\{\frac{M}{\sqrt{1-M^2}}\,\frac{\left(\frac{x_a}{r_a}+M\right)}{\left(1+M\,\frac{x_a}{r_a}\right)} - \sqrt{\frac{M^2}{1-M^2} - \tan^2\Lambda}\right\}^{1/2}}$$

so that the part in curly brackets of the trailing-edge contribution to the directivity pattern in (3.14a) (the Fresnel integral vanishes since its argument vanishes) becomes

$$\frac{1}{\left[\frac{M}{\sqrt{1-M^2}}\frac{(\frac{x_a}{r_a}+M)}{(1+M\frac{x_a}{r_a})}-\sqrt{\frac{M^2}{1-M^2}-\tan^2\Lambda}\right]^{1/2}}$$

thus cancelling that from the leading edge. If we now look at the high-frequency behavior of the term inside the large curly brackets, we obtain that for large k_x, it becomes

$$\frac{1}{\sqrt{2}\left\{\frac{M^2}{1-M^2}-\tan^2\Lambda\right\}^{1/2}}$$

$$\left\{-i+\frac{(1+i)\sqrt{1-M^2}}{2\sqrt{k_x}}\left[\frac{e^{\frac{-4ik_x}{1-M^2}\sqrt{\frac{M^2}{1-M^2}-\tan^2\Lambda}}}{\sqrt{\frac{M^2}{1-M^2}-\tan^2\Lambda}+\frac{M}{\sqrt{1-M^2}}\frac{(\frac{x_a}{r_a}+M)}{(1+M\,x_a/r_a)}}\right]^{1/2}\right\}$$

We conclude that in the high-frequency limit $k_x=\infty$, the far-field we have calculated for supersonic trace speeds is well behaved everywhere, even along the direction given by (3.16). However, since the limiting processes cannot be interchanged, that is, the solution is not well behaved if we first approach the direction of (3.16) and then let $k_x\to\infty$, we note that for supersonic trace speeds the uniform convergence promised by Landahl[11] in two dimensions does not carry to three.

We notice from (3.13) and (3.14a,b), that for large k_x the predicted acoustic spectrum (not including w_0) decays as $1/k_x$, the behavior of the second term on the right side of

(3.14b) in the expression for $G/\sqrt{1-M^2}$. this large-k_x behavior has an associated small-time behavior for the transient signal which may or may not be correct - recall that the present aerodynamic model does not predict well radiation from tip dipoles. However, as we will see in chapter 5, where we develop a better aerodynamic model for the blade tip edge, the $1/k_x$ behavior is the correct one after all; so that in fact, for small times the expressions in (3.13), (3.14a,b) are off by at most a multiplicative constant.

Since the trailing-edge part of the solution hardly contributes for small times (the high-frequency behavior is given by the leading-edge solution, whose directivity does not depend on frequency), essentially all the phase information in contained in $G/\sqrt{1-M^2}$, which can be traced back to the λ_2 transform of the spanwise linear loading. Also, since $G/\sqrt{1-M^2} = L/2$ at $k_x=0$, we see that the predicted spectrum takes on a constant value at $k_x=0$.

We now express (3.14a,b) for the case of a subsonic trace speed of disturbances. Also, we introduce the spherical coordinate system (r_a, γ, ϕ) shown in fig. 3.2, in order to define the position of a listener on the ground.

We have then, that

$$D_{3\text{-}D}(\gamma,\phi) = \cos\phi \left\{ \frac{1}{\left[\frac{M}{\sqrt{1-M^2}}\left(\frac{\sin\phi\,\cos\gamma}{1+M\,\sin\phi\,\cos\gamma}\right) + i\sqrt{\tan^2\Lambda - \frac{M^2}{1-M^2}}\right]^{1/2}} + \right.$$

$$\left. \frac{i\sqrt{2}\left\{\tan^2\Lambda - \frac{M^2}{1-M^2}\right\}^{1/4}}{\left\{\tan^2\Lambda - \frac{M^2}{1-M^2} + \left[\frac{M}{\sqrt{1-M^2}}\,\frac{(\sin\phi\,\cos\gamma + M)}{1+M\sin\phi\cos\gamma}\right]^2\right\}^{1/2}} \cdot \left\{ 1-(1+i). \right.\right.$$

$$E^* \left[\frac{2k_x}{\sqrt{1-M^2}} \left(-i\sqrt{\tan^2\Lambda - \frac{M^2}{1-M^2}} - \frac{M}{\sqrt{1-M^2}} \frac{(\sin\phi\cos\gamma + M)}{(1+M\sin\phi\cos\gamma)} \right) \right] \Bigg\} \Bigg\} \quad (3.17a),$$

$$G\left[k_x \left(\frac{M\sin\phi\sin\gamma}{1+M\sin\phi\cos\gamma} - \tan\Lambda \right) \right] / \sqrt{1-M^2}$$

$$G\left[k_x \left(\frac{M\sin\phi\sin\gamma}{1+M\sin\phi\cos\gamma} - \tan\Lambda \right) \right] / \sqrt{1-M^2} = \frac{e^{-ik_x L \left(\tan\Lambda - \frac{M\sin\phi\sin\gamma}{1+M\sin\phi\cos\gamma}\right)^{-1}}}{L\left(k_x \left[\tan\Lambda - \frac{M\sin\phi\sin\gamma}{1+M\sin\phi\cos\gamma} \right] \right)^2}$$

$$+ \frac{i\, e^{-ik_x L \left(\tan\Lambda - \frac{M\sin\phi\sin\gamma}{1+M\sin\phi\cos\gamma}\right)}}{k_x \left(\tan\Lambda - M\sin\phi\sin\gamma/(1+M\sin\phi\cos\gamma)\right)} \quad (3.17b).$$

For large Λ, the imaginary term in the argument of the Fresnel integral dominates the real part. As a result, the Fresnel integral has essentially an Error-function behavior which, as a function of γ, ϕ, does not provide for much lobing in the directivity pattern - certainly not as much as we had in the two-dimensional patterns of chapter 2. This is generally apparent in part (a) of figs. 3.3-3.8 for the three-dimensional directivity function $D_{3\text{-}D}(\gamma, \phi)$ for a number of cases of interest. Actually, in order to make comparisons with the results from chapter 2, we have plotted here the quantity

$$\frac{(1-M^2)^{1/4}\sqrt{k_x}}{2\sqrt{\pi}} \quad \frac{D_{3\text{-}D}(\gamma,\phi)}{(1+M\sin\phi\cos\gamma)^2} \quad M$$

The difference in the acoustic spreading effect between two and three dimensions (the $1/\sqrt{r}$ and $1/r_a$ factors) is not taken into account in the comparison. In order to include this

effect, we would multiply the above expression by $1/\sqrt{r_a}$.

In fig. 3.3a-d we have selected a set of physical parameters $(M, A, \omega b/U)$ so that the resulting value of $|\mu^2|$ matches that of fig. 2.5a. Notice the decreased efficiency of the wing as an acoustic radiator for the present three-dimensional case with load fronts which travel subsonically through the still fluid. The $\cos\Phi\, G/\sqrt{1-M^2}$ part is then a slowly varying function of Υ, ϕ; essentially it has a radiation pattern on the plane $\Upsilon = 90°$, $-\pi/2 < \phi < \pi/2$ (normal to the flight direction) equivalent to that for a strong tip dipole plus a somewhat weaker dipole located at some distance inboard. On the plane parallel to the flight direction ($\gamma = 0°$, $-\pi/2 < \phi < \pi/2$), the contribution of $\cos\phi\, G/\sqrt{1-M^2}$ is just that of a simple dipole. As previously discussed, for the two-dimensional case from chapter 2 the speed of the disturbance through the fluid was supersonic, and so, every section along the blade's infinite span radiated noise.

Figs. 3.3, 3.4, and 3.5 show the differences in the directivity patterns for three different tones. The "rippling" increases with reduced frequency, and the magnitudes decrease. Figs. 3.4 and 3.6 illustrate the effect of a change in Mach number. Compressibility has the same effect of increasing the rippling of the pattern - again, bringing out the lumped character of compressibility and frequency effects for our noncompact blade. Another important high-speed effect is the increased forward enhancement of signals (compare fig. 3.4a to fig. 3.6a).

From figs. 3.5 and 3.7, we see the effect of a change in Λ, the interaction angle, on the radiation field. Notice that the greatest qualitative differences occur on the azimuth $\gamma=90^{\circ}$. This is consistent with the earlier interpretation of the radiation field on the plane normal to the flight direction as essentially due to a strong tip dipole and a weak inboard dipole: changes in mostly affect their difference in phase. Also, notice the reduced levels for $\Lambda=80^{\circ}$. The reason for this is somewhat more subtle: for larger , the effective trace Mach number of the load fronts has a lower value; as a result $G/\sqrt{1-M^2}$ in (3.17b) is farther for $\Lambda=80^{\circ}$ than for $\Lambda=62^{\circ}$ from assuming its peaky maximum value for a given frequency. Physically, there can be more cancellation of acoustic signals for the greater value of $\Lambda=80^{\circ}$.

Finally, in fig. 3.8 we consider a case in which the trace speed of sources through the fluid is nearly transonic: we choose our parameters $M,\Lambda,\omega b/U$ so that μ^2 takes on the relatively small value of -1. Since the imaginary part of the Fresnel integral in (3.17a) is then small ($\tan\Lambda\tilde{=}M/\sqrt{1-M^2}$, or $\sin\Lambda\tilde{=}M$), we would expect the latter to behave as one, rather than as an Error function. The observed complexity of the pattern for $\gamma=180^{\circ}$, $0<\phi<\pi/2$ clearly shows the increased participation of the trailing-edge part of the solution. For the $\gamma=135^{\circ}$, 150° azimuths, we notice that $G/\sqrt{1-M^2}$ is reaching its peaky behavior, indicating physically that a preferred direction of strong radiation is about to appear normal to the load fronts (the transonic Mach plane).

Application of leading-edge theory to prediction of noise for a potential vortex

We consider a potential vortex in the still fluid oriented at interaction angle Λ, measured from the leading edge (fig. 3.9a). The vortex is located a distance h chords below the plane of flight, where it induces the upwash pattern in a plane normal to its own axis indicated in fig. 3.9b, and given by the Biot-Savart law:

$$w(\xi) = -\frac{\Gamma/b}{2\pi} \quad \frac{\xi}{\xi^2+h^2} \tag{3.18},$$

where Γ is the vortex strength, in ft^2/sec. By Fourier's theorem, we may express this upwash as a sum of sinusoidal gusts

$$w(\xi) = \int_{-\infty}^{\infty} dk e^{-ik\xi} W(k) \tag{3.19}.$$

Since $\xi = x_a \cos\Lambda + y\sin\Lambda$, we have that

$$W(k) = \int\int_{-\infty}^{\infty} \frac{dx_a\,dy}{(2\pi)^2} \; e^{ik_x x_a + ik_y y} \; w(x_a\cos\Lambda + y\sin\Lambda) = \delta(k_y - k_x\tan\Lambda) \; \frac{W(k_x/\cos\Lambda)}{\cos\Lambda} \tag{3.20},$$

from which

$$w(x_a\cos\Lambda + y\sin\Lambda) = \int\int_{-\infty}^{\infty} dk_y dk_x \; e^{-ik_x x_a - ik_y y} \; W(k) = \int_{-\infty}^{\infty} dk_x \; e^{-ik_x x_a - ik_x \tan\Lambda y} \; \frac{W(k_x/\cos\Lambda)}{\cos\Lambda} \tag{3.21}.$$

If we now recall that $bx_a = bx - Ut$, where x is fixed on the wing, we see that (3.21) becomes

$$w(x\cos\Lambda+y\sin\Lambda) = \int_{-\infty}^{\infty} dk_x \, e^{\frac{ik_x U t}{b}} \, w_o(k_x/\cos\Lambda) \, e^{-ik_x x - ik_x \tan\Lambda \, y} \tag{3.22}$$

where we have called $W(k_x/\cos\Lambda)/\cos\Lambda = w_o(k_x/\cos\Lambda)$, and identified it as the magnitude of the convected gust (as seen by an observer on the airfoil) in all our work up to this point. Notice that $k_x U/b = \omega$, the acoustic frequency if $k_x = \omega b/U$, the reduced frequency.

In chapter 2 and the first part of the present chapter we have determined the tone emitted by the passage of a blade through a gust, the integrand in (3.22). In order to calculate the acoustic field for the passage over the vortex, we simply superpose the solution of the gust problems properly weighted by the function $w_o(k_x/\cos\Lambda)$. We have then, for the transient signal $\bar{p}(\bar{r},t)$, that

$$\bar{p}(\bar{r},t) = \int_{-\infty}^{\infty} dk_x \, P(\bar{r},t;k_x) \tag{3.23}$$

We now want to evaluate $\bar{p}(\bar{r},t)$ for the model developed in this chapter, that is, for $P(\bar{r},t;k_x)$ given by (3.16), (3.17a,b). We have shown that for the high part of the spectrum P may be adequately approximated by the leading-edge part of the solution, which we rewrite here for convenience with a few changes in notation:

$$P(\bar{r},t;k_x) = -\frac{i\rho_o U}{2\pi} \frac{w_o(k_x/\cos\Lambda)\,(1-M^2)^{1/4}}{\sqrt{1-i|\tan\Lambda|}\left\{1-\frac{M^2}{\sin^2\Lambda}\right\}^{1/2}} \frac{M\cos\phi}{(1+M\sin\phi\cos\gamma)^2}$$

$$\frac{1}{\left\{\frac{M\ (\sin\phi\cos\gamma+M)}{1+M\sin\phi\cos\gamma} + i\,|\tan\Lambda|\sqrt{1-\frac{M^2}{\sin^2\Lambda}}\right\}^{1/2}} \quad e^{\frac{ik_x U}{b}} \quad \frac{\tau}{(1+M\sin\phi\cos\gamma)}$$

$$\int_0^L dy'\ e^{-ik_x \frac{y'}{L}\left(\tan\Lambda - \frac{M\sin\phi\cos\gamma}{1+M\sin\phi\cos\gamma}\right)y'} \qquad (3.24),$$

where $\tau = t - br/c_0$, the source, or retarted time.

If we now let $\tau^* = \tau/(1+M\sin\phi\cos\gamma)$, substitute for P into (3.23) and apply the convolution theorem, we find that

$$\bar{p}(\bar{r},\tau^*) = \int_{-\infty}^{\infty} \frac{d\tau'}{2\pi} g(\tau')\ f(\tau^*-\tau') \qquad (3.25),$$

where

$$g(\tau^*) = \frac{2\pi\tau^*}{L} \quad \text{for } 0<\tau^*<L \quad \tan\Lambda - \frac{M\sin\phi\sin\gamma}{1+M\sin\phi\cos\gamma} \qquad (3.26a),$$

$$f(\tau^*) = \int_{-\infty}^{\infty} dk_x\ e^{ik_x\tau^*}\ w_0\ (k_x/\cos\Lambda) \qquad (3.26b).$$

For a potential vortex, we find that

$$w_0\left(\frac{k_x}{\cos\Lambda}\right) = \frac{-i\Gamma/b}{4\pi\cos\Lambda}\ \frac{k_x}{|k_x|}\ e^{\frac{-h}{\cos\Lambda}|k_x|} \qquad (3.27);$$

so that

$$f(\tau^*) = \frac{\Gamma/b}{2\pi\cos\Lambda}\ \frac{\tau^*}{\tau^{*2} + (h/\cos\Lambda)^2} \qquad (3.28).$$

With f and g so given, the integral in (3.25) may be evaluated in closed form. The final result for the acoustic

signature which a listener on the ground hears br_a/c_o time units after the blade has passed over the vortex is

$$\bar{p}\,(\bar{r},\tau)=-i\,\frac{\rho_o U}{2\pi}\,\frac{(1-M^2)^{1/4}}{\sqrt{1-i\,\sqrt{1-M^2}\left\{\tan^2\Lambda-\frac{M^2}{1M^2}\right\}^{1/2}}}\,\frac{1}{r_a}\,\frac{\cos\phi}{(1+M\sin\phi\cos\gamma)^2}$$

$$\frac{1}{\left\{\frac{M(\sin\phi\cos\gamma+M)}{1+M\sin\phi\cos\gamma}+i|\tan\Lambda|\sqrt{1-\frac{M^2}{\sin^2\Lambda}}\right\}^{1/2}}\,\frac{\Gamma/b}{L\cos\Lambda}\left\{-L\left(\frac{\tan\Lambda-M\sin\phi\sin\gamma}{1+M\sin\phi\cos\gamma}\right)+\right.$$

$$\frac{h}{\cos\Lambda}\arctan\left[\frac{\bar{\tau}/(1+M\sin\phi\cos\gamma)}{h/\cos\Lambda}\right]-\frac{h}{\cos\Lambda}\arctan\left[\frac{\bar{\tau}}{1+M\sin\phi\cos\gamma}-L\,\frac{\left(\tan\Lambda-\frac{M\sin\phi\sin\gamma}{1+M\sin\phi\cos\Lambda}\right)}{h/\cos\Lambda}\right]$$

$$-\bar{\tau}/[2\,(1+M\sin\phi\cos\gamma)]\Bigg\}$$

$$\log\left[\frac{\left(\frac{\bar{\tau}}{1+M\sin\phi\cos\gamma}-L\,\frac{(\tan\Lambda-M\sin\phi\sin\gamma)}{1+M\sin\phi\cos\gamma}\right)^2+(h/\cos\Lambda)^2}{[\bar{\tau}/(1+M\sin\phi\cos\gamma)]^2+(h/\cos\Lambda)^2}\right]\frac{M(1-M^2)^{1/4}}{2\pi\left[\tan\Lambda-\frac{M\sin\phi\sin\gamma}{1+M\sin\phi\cos\gamma}\right]^2}$$

where $\bar{\tau}=\tau U/b$ (3.29).

For the present noncompact situation, there is no guarantee that the maximum values of the acoustic signal (3.29) will coincide with the field point where its tones individually reach their maximum amplitudes. From figs. 3.3-3.5, we see that the far-field point where each tone had its maximum is not a very strong function of frequency; so that essentially they all had large amplitudes at $\phi=65°, \gamma=180°$, for the cases in figs. 3.3-3.5. Still, the phases of the spectral components could conspire to cause a great deal of cancellation, and the far-field point of maximum peak level might be where we least expect it: at some point where the tone amplitudes are not particularly high,

but where their phases reinforce strongly.

Such fears and suspicions prompted the calculation of part the directivity pattern, shown in fig. 3.10, of the peak signal for the case of M=.8, $\Lambda=62^{\circ}$, the case corresponding to the tones of figs. 3.3-3.5. We used a value of 238 ft^2/sec for the maximum sectional circulation (assumed occurring at the 75% span). For M=.8 this choice implies a maximum sectional lift $L_{max}=\rho_o M c_o \Gamma=498$ lb/ft, which, if assumed as acting at the blade tip and decreasing linearly to zero at the hub, gives a value of 3735 lb of lift for each 15-ft blade.

We find that although the point $\phi=65^{\circ}, \gamma=180^{\circ}$ is in fact where the signature reaches its maximum level, substantial variations exist: for example, the peak level at $\phi=70^{\circ}, \gamma=150^{\circ}$ was only 114 dB for h/b=.1, compared to that at $\phi=65^{\circ}, \gamma=180^{\circ}$, where the signal had the maximum level of 131 dB for the same value of blade-vortex separation h. From just looking at the patterns in parts (a) and (e), for $\phi=65^{\circ}$, $\gamma=70^{\circ}$, respectively, of figs. 3.3-3.5, one should never have expected such a large difference.

Fig. 3.11a,b shows predicted signatures at the point $\phi=65^{\circ}, \gamma=180^{\circ}$, where the signal was loudest for h/b=.1 (fig. 3.11b). The value of r_a is 1000 ft. The case for h/b=.5 (fig. 3.11a) had a lower peak value of 126 dB. This is to be expected, since dF/dt on the blade should then be less.

The purpose of fig. 3.11c is to show, upon comparison to fig. 3.11b, that our closed-form solution (3.29) contains

the Doppler-shift information of the blade-slap signature. As indicated, the signal in fig. 3.11c was evaluated at a point also on the plane parallel to the flight direction (for $\gamma=180^{\circ}$, $0<\phi<\pi/2$), but at a higher elevation angle ϕ so that it should be less shifted. And it is.

Fig. 3.12 shows the spectra of signals corresponding to the M, Λ cases of figs. 3.3-3.8. They were calculated at the field position where each tone reached its maximum amplitude. As previously noted, for $M=0.8$, $\Lambda=62^{\circ}$ this point coincided with the maximum peak level; the same may not be true of the others. The main objective of the figure is to show the large differences which exist in the rates of decay of the spectra between the h/b=.5 and h/b=.1 cases, and to indicate, for one of the cases, the value of frequency above which the present noncompact model is valid. We recall from the discussion at the end of chapter 2 that effects of noncompactness become significant for $\mu > .7$, for supersonic trace speeds, and for μ greater than some value less than .7 for subsonic trace speeds. For $\Lambda=62^{\circ}$, $M=.8$, $\mu>.7$ for $f>819$ Hz. This is the section of the spectrum which should be predicted using a noncompact theory; as we clearly see, for h/b=.1 it contains a substantial amount of the signature's acoustic energy.

Chapter 4: Quarter-infinite plate with side edge passing through a gust

The acoustic model developed in chapter 3 overestimated the strength and phase of acoustic dipoles near the tip of a rotating blade. This must be so, since there we simply cut off the loading abruptly at the tip, where in reality we know it must vanish as $\sqrt{L-y}$. Yet, when the load fronts due to the interaction travel subsonically through the fluid, that is, for $M/\sin\Lambda<1$, only outboard sections actually radiate sound. Because this type of interaction is generally believed to occur often in single-rotor helicopters, it is important, therefore, that we be able to model the strength of tip dipoles more accurately than we did in chapter 3. That is the purpose of the present chapter.

The model we develop here is more rudimentary in some ways than that worked out earlier: for simplicity we remove the trailing edge and allow the wing to have a semi-infinite span; also we cannot model blade rotation here. Still, the theory we develop below for a quater-infinite plate passing through a gust proves itself useful in chapter 5, where we make a rational simplification which allows us to reintroduce the trailing edge and so, to predict acoustic radiation from a blade of semi-infinite span with correct side-edge loading passing through a gust.

We start here by stating the boundary-value problem for the three-dimensional velocity potential field Φ, due to the interaction of a quarter-infinite plate with side edge with an oblique gust. Again, the oblique gust is that wavenumber

component of amplitude w_o of the upwash on the plane of flight induced by a vortex convected at angle of obliqueness Λ by a subsonic freestream (fig. 4.1). The governing equation - the linearized convected-wave equation, and the boundary conditions are

$$\Phi_{xx}+\Phi_{yy}+\Phi_{zz}-\frac{1}{c_o^2}\frac{D^2\Phi}{Dt^2}=0 \qquad (4.1),$$

$$\Phi_z(x>0,y>0,0,t) = -w_o s\, e^{i\omega t - ik_x x - ik_x \tan\Lambda\, y} \qquad (4.2a),$$

$$\Phi(x,y<0,0,t) = \Phi(x<0,y,0,t) = 0 \qquad (4.2b);$$

where we use the symbol k_x for the reduced frequency as we did in chapters 2 and 3. Here however, $k_x=\omega s/U$, s being a characteristic length in the problem which at this point we leave unspecified. The reason for this ambiguity is that although the only characteristic length for now is the acoustic wavelength itself, in chapter 5 we reintroduce the trailing edge, and with it, the blade semichord - a more useful characteristic length for the model.

The three-dimensional pressure field P(x,y,z,t) is also required to satisfy (4.1) and (4.2b). In addition, we expect it to have the following behavior near the edges

$$P(x\to 0+,y>0,0,t) \sim 1/\sqrt{x} \qquad (4.3a),$$

$$P(x>0,y\to 0+,0,t) \sim \sqrt{y} \qquad (4.3b).$$

As before in chapter 3, we let $\Phi = \phi_* \exp[i(\omega t + k_x M^2 x/(1-M^2))]$; notice, however, that the $\exp[-ik_x \tan\Lambda y]$ term is not included. We make the changes $y = Y/\sqrt{1-M^2}$, $z = Z/\sqrt{1-M^2}$. Similar changes are made for P. The boundary-value problem for ϕ_* becomes

$$\phi_{*xx} + \phi_{*yy} + \phi_{*ZZ} + K^2\phi_* = 0 \qquad (4.4),$$

with

$$\phi_{*Z}(x>0, Y>0, 0) = \frac{-w_0 s}{\sqrt{1-M^2}} \; e^{\frac{-ik_x x}{1-M^2}} - \frac{ik_x \tan\Lambda Y}{\sqrt{1-M^2}} \qquad (4.5a),$$

$$\phi_*(x<0, y, 0) = \phi_*(x, y<0, 0) = 0 \qquad (4.5b).$$

We define the transform pair

$$\phi_*(x,Y,Z) = \int_{C_2} \frac{d\lambda_2}{\sqrt{2\pi}} \; e^{-i\lambda_2 Y} \int_{C_1} \frac{d\lambda_1}{\sqrt{2\pi}} \; e^{-i\lambda_1 x} \; \tilde{\phi}(\lambda_1, \lambda_2; Z) \qquad (4.6a),$$

$$\tilde{\phi}(\lambda, \lambda_2; Z) = \int_{-\infty}^{\infty}\int \frac{dx\, dY}{2\pi} \; e^{i\lambda_1 x + i\lambda_2 Y} \; \phi_*(x, Y, Z) \qquad (4.6b);$$

where C_1, and C_2 denote complex integration contours in the λ_1, λ_2 planes, respectively. We apply (4.6b) to (4.4). The solution for positive Z is

$$\phi_*(x,Y,Z) = \int_{C_1} \frac{d\lambda_1}{\sqrt{2\pi}} e^{i\lambda_1 x} \int_{C_2} \frac{d\lambda_2}{\sqrt{2\pi}} \; e^{-i\lambda_2 Y} - Z\sqrt{\lambda_1^2+\lambda_2^2-K^2} \; \tilde{\phi}(\lambda_1, \lambda_2; 0+) \qquad (4.7).$$

Since $\phi_*(x,Y<0,0)=0$, it follows from (4.7) with Z=0 that $\tilde{\phi}(\lambda_1,\lambda_2)$ must be an analytic function of λ_2 in the upper half λ_2 plane. Using standard nomenclature, we therefore say that $\tilde{\phi}=\tilde{\phi}_{\oplus}$. From (4.7) we may calculate $\frac{\partial\tilde{\phi}}{\partial Z}(x,Y,0)$, the vertical velocity field from the solution on the plane of the plate:

$$\tilde{\phi}_{*_Z}(x,Y,0+)= -\int_{C_1}\frac{d\lambda_1}{\sqrt{2\pi}}e^{-i\lambda_1 x}\int_{C_2}\frac{d\lambda_2}{\sqrt{2\pi}}e^{-i\lambda_2 Y}\;\tilde{\phi}_{\oplus}(\lambda_1,\lambda_2;0+)\;\sqrt{\lambda_1^2+\lambda_2^2-K^2} \qquad (4.8).$$

The boundary-value problem posed by (4.4), (4.5a,b) cannot be solved exactly for subsonic flow by any simple analytical procedure known. The assumptions which follow, however, allow us to obtain an approximate solution which later we show is valid and useful for short acoustic wavelengths; effectively, by making them we relax the requirement of $\phi_*(x<0,Y,Z)=0$. We let

$$-\tilde{\phi}(\lambda_1,\lambda_2,0+)\;\sqrt{\lambda_1^2+\lambda_2^2-K^2} = \tilde{r}(\lambda_1,\lambda_2)+\tilde{v}(\lambda_1,\lambda_2) \qquad (4.9),$$

where

$$r(x,Y) = \begin{cases} 0 \text{ for } Y<0 \\ \text{2-D UPWASH for } Y>0 \end{cases} \qquad (4.10a),$$

$$v(x,Y) = \begin{cases} ? \text{ for } Y<0 \\ 0 \text{ for } Y>0 \end{cases} \qquad (4.10b).$$

From chapter 2, equation (2.12), the upwash on the plane Z=0 of the two-dimensional solution turns out to be

$$r(x,Y,0) = \frac{-iw_0 s\, e^{-ik_x \tan\Lambda Y}}{2\pi\sqrt{1-M^2}} \frac{1}{\sqrt{\frac{k_x}{1-M^2}+\mu}} \int_{C_1} \frac{d\lambda_1}{\left(\lambda_1 - \frac{k_x}{1-M^2}\right)} e^{-i\lambda x} \cdot \sqrt{\lambda_1+\mu} \quad (4.11),$$

where C_1 is as C in fig. 2.2. We therefore find that

$$\tilde{r}(\lambda_1,\lambda_2) = \frac{A(\lambda_1)}{\lambda_2 - \frac{k_x \tan\Lambda}{\sqrt{1-M^2}}} \quad (4.12),$$

where

$$A(\lambda_1) = \frac{-w_0 s\sqrt{\lambda_1+\mu}}{2\pi\sqrt{1-M^2}\sqrt{\frac{k_x}{1-M^2}+\mu}} \frac{1}{\left(\lambda_1 - \frac{k_x}{1-M^2}\right)}$$

In the solution we are constructing, $v(x,Y>0)=0$ as stated in (4.10b). It follows, therefore, that $\tilde{v}(\lambda_1,\lambda_2)$ must be an analytic function of λ_2 in the lower half λ_2 plane, and so we write $\tilde{v}(\lambda_1,\lambda_2)=\tilde{v}_{\ominus}(\lambda_1,\lambda_2)$. Substituting for $\tilde{r}$ and $\tilde{v}$ in (4.9), and factoring the term $\sqrt{\lambda_1^2+\lambda_2^2-K^2}$, we have that

$$\phi_{\oplus}(\lambda_2)\sqrt{\lambda_2-(K^2-\lambda_1^2)^{1/2}} = \left\{\frac{A(\lambda_1)}{\lambda_2 - \frac{k_x\tan\Lambda}{\sqrt{1-M^2}}}\right\} \frac{1}{\sqrt{\lambda_2+(K^2-\lambda_1^2)^{1/2}}} + \frac{\tilde{v}_{\ominus}(\lambda_2)}{\sqrt{\lambda_2+(K^2-\lambda_1^2)^{1/2}}} \quad (4.13),$$

where we have written $\tilde{\phi}_{\oplus}(\lambda_2)$ instead of $\tilde{\phi}_{\oplus}(\lambda_1,\lambda_2)$ to avoid confusion as to the meaning of the symbol $\oplus$, which refers here to the analyticity of $\tilde{\phi}$ in the upper half of the λ_2 plane, not the λ_1 plane.

We recall now that since an $\exp(i\omega t)$ behavior for the harmonic time dependence was made, the condition of outward wave propagation requires us, to allow ω, and so k_y and μ, to have a small negative imaginary part. Also, we notice from (4.13) that the two radicals $\sqrt{\lambda_2-(K^2-\lambda_1^2)^{1/2}}$ and $\sqrt{\lambda_2+(K^2-\lambda_1^2)^{1/2}}$ contain

the quantity $\sqrt{K^2-\lambda_1^2}$, a function of λ_1 which has branch points at $\lambda_1=\pm K$. We choose that branch of $\sqrt{\lambda_1^2-K^2}$ with vanishing argument as $|\lambda_1|\to\infty$ along the C_1 contour. This choice now implies two new branch cuts in the λ_1 plane, which now is as shown in fig. 4.2a. Fig. 4.2b indicates the position of the singularities in the λ_2 plane and the corresponding regions of $\ominus$ and $\oplus$ analyticity.

If we split in the usual way the first term on the right side of (4.13) into a sum of two functions, one $\oplus$ and the other $\ominus$, we obtain a Wiener-Hopf equation of the form $\oplus=\ominus$ from which we may find $\tilde{\phi}_{\oplus}$ in a straightforward manner; the details parallel those for the leading-edge problem in chapter 2 and so will not be repeated here. We find that

$$\tilde{\phi}_{\oplus}(\lambda_2) = \frac{-A(\lambda_1)}{\sqrt{\frac{k_x\tan\Lambda}{\sqrt{1-M^2}} + (K^2-\lambda_1^2)^{1/2}}} \frac{1}{\sqrt{\lambda_2-(K^2-\lambda_1^2)^{1/2}}} \frac{1}{\left(\lambda_2-\frac{k_x\tan\Lambda}{\sqrt{1-M^2}}\right)} \quad (4.14).$$

Substituting for A and by means of (4.7) we obtain $\tilde{\phi}(x,Y,Z)$. From the linearized relation between pressure and velocity potential $p_*=-(\rho_0 U/s)((ik_x/(1-M^2)\phi_*+\partial\phi_*/\partial x)$, we may also calculate $p_*(x;Y,Z+)$. The final results are:

$$\phi_*(x,Y,Z) = -\frac{w_0 s}{4\pi^2\sqrt{1-M^2}} \frac{1}{\sqrt{\frac{k_x}{1-M^2}+\mu}} \int_{C_1} \frac{d\lambda_1 e^{-i\lambda_1 x}\sqrt{\lambda_1+\mu}}{\left(\lambda_1-\frac{k_x}{1-M^2}\right)\sqrt{\frac{k_x\tan\Lambda}{\sqrt{1-M^2}}+(K^2-\lambda_1^2)^{1/2}}}$$

$$\int_{C_2} \frac{d\lambda_2 e^{-i\lambda_2 Y - Z\sqrt{\lambda_1^2+\lambda_2^2-K^2}}}{\left(\lambda_2-\frac{k_x\tan\Lambda}{\sqrt{1-M^2}}\right)} \frac{1}{\sqrt{\lambda_2-(K^2-\lambda_1^2)^{1/2}}} \quad (4.15),$$

$$p_*(x,Y,Z) = -\frac{i\rho_0 w_0 U}{4\pi^2\sqrt{1-M^2}}\frac{1}{\sqrt{\frac{k_x}{1-M^2}+\mu}}\int_{C_1}\frac{d\lambda_1 e^{-i\lambda_1 x}\sqrt{\lambda_1+\mu}}{\sqrt{k_x\tan\Lambda/\sqrt{1-M^2}+(K^2-\lambda_1^2)^{1/2}}}$$

$$\int_{C_2}\frac{d\lambda_2 e^{-i\lambda_2 Y - Z\sqrt{\lambda_1^2+\lambda_2^2-K^2}}}{(\lambda_2-k_x\tan\Lambda/\sqrt{1-M^2})}\frac{1}{\sqrt{\lambda_2-(K^2-\lambda_1^2)^{1/2}}} \qquad (4.16).$$

Asymptotic behavior of solution near the edges

By construction, the integrand of the λ_2 integral is an analytic function of λ_2 in the upper half λ_2 plane, and consequently $p_*(x,Y<0,0)=0$. However, the integrand of the λ_1 integral is not an analytic function of λ_1 in the upper half λ_1 plane. As a result, the solution in (4.16) does not satisfy the condition of $p_*(x<0,Y,0)=0$. The next step in our analysis is to determine how severely the result in (4.16) violates this upstream condition and also to find whether it has the required behavior near the edges. We therefore set $Z=0+$ and obtain from (4.16), after evaluating the λ_2 integral in closed form, that

$$p_*(x,Y>0,0+) = \frac{(i-1)\rho_0 w_0 U}{2\pi\sqrt{1-M^2}\sqrt{\frac{k_x}{1-M^2}+\mu}}\, e^{\frac{-ik_x\tan\Lambda Y}{\sqrt{1-M^2}}} \cdot \int_{C_1}\frac{d\lambda_1}{\sqrt{\lambda_1-\mu}}\, e^{-i\lambda_1 x}\left[E\left(Y\left(\frac{k_x\tan\Lambda}{\sqrt{1-M^2}}-\sqrt{K^2-\lambda_1^2}\right)\right)\right] \qquad (4.17)$$

In order to investigate the solution for small values of x, that is, near the leading edge, we look at the large-λ_1 asymptotic form for the integrand (at the same time with Y not small). Expanding the Fresnel integral for large argument, we have

$$p_*(x,Y>0,0) = -\frac{\rho_0 w_0 U}{2\pi\sqrt{1-M^2}}\frac{1}{\sqrt{\frac{k_x}{1-M^2}+\mu}}\left\{e^{\frac{-ik_x\tan Y}{\sqrt{1-M^2}}}\int_{C_1}\frac{d\lambda_1}{\sqrt{\lambda_1-\mu}}\, e^{-i\lambda_1 x}\right.$$

$$+\frac{e^{\frac{-3\pi i}{4}}}{\sqrt{\pi}}\sum_{n=0}^{\infty}\frac{(-i)^n(2n+1)!}{2^{2n}n!}\frac{1}{Y^{n+1/2}}\left\{\int_{C_1}\frac{d\lambda_1 e^{-i\lambda x-Y\sqrt{\lambda_1^2-K^2}}}{\sqrt{\lambda_1-\mu}}\left(\frac{k_x\tan\Lambda}{\sqrt{1-M^2}}-\sqrt{K^2-\lambda_1^2}\right)^{n+1/2}\right\} \quad (4.18),$$

so that the leading term in the behavior near the leading edge is the two-dimensional leading-edge solution in chapter 2's equation (2.15), which vanishes for $x<0$ and behaves as $1/\sqrt{x}$ for $x=0+$. The part of the solution which does not vanish upstream of the plate appears as an asymptotic series in inverse powers of Y, the distance from the side edge normalized by the characteristic length s; it also represents the three dimensional effect of the side edge on the loading $p_*(x,Y>0,0)$.

To calculate the coefficients of the asymptotic series in (4.18), we must evaluate the integral

$$I_n(x,Y>0)=\int_{C_1}\frac{d\lambda_1}{\sqrt{\lambda_1-\mu}}\,e^{-i\lambda_1 x-Y\sqrt{\lambda_1^2-K^2}}\left\{\frac{k_x\tan\Lambda}{\sqrt{1-M^2}}-\sqrt{K^2-\lambda_1^2}\right\}^{n+1/2} \quad (4.19)$$

for $Y>0$, $x\to 0+$. By the convolution theorem, we may rewrite it as

$$I_n(x,Y>0)=-i\sqrt{\frac{\pi}{2}}\int_{-\infty}^{\infty}d\xi H_1^{(2)}\left(K\sqrt{(x-\xi)^2+Y^2}\right)\frac{KY}{\sqrt{(x-\xi)^2+Y^2}}f_n(\xi) \quad (4.20),$$

where

$$f_n(x)=\int_{C_1}\frac{d\lambda_1}{\sqrt{2\pi}}\,\frac{e^{-i\lambda_1 x}}{\sqrt{\lambda_1-\mu}}\left\{\frac{k_x\tan\Lambda}{\sqrt{1-M^2}}-\sqrt{K^2-\lambda_1^2}\right\}^{n+1/2} \quad (4.21).$$

The integrand in $f_n(x)$ has branch-point singularities at

$\lambda_1 = \pm K$. Besides these, we also find that as $\lambda_1 \to \pm\mu$

$$\left\{\frac{1}{\frac{k_x \tan\Lambda}{\sqrt{1-M^2}} - \sqrt{K^2-\lambda_1^2}}\right\}^{n+1/2} \simeq \left(\frac{2k_x\tan\Lambda}{\sqrt{1-M^2}}\right)^{n+1/2} \frac{1}{(\lambda_1^2-\mu^2)^{n+1/2}} \quad (4.22),$$

so that in addition we have a pole of order n+1 at $\lambda_1 = \mu$ and another branch point at $\lambda_1 = -\mu$. We write therefore that

$$f_n(x) = f_n^{\pm\mu}(x) + f_n^{\pm K}(x) \quad (4.23a),$$

$$I_n(x) = I_n^{\pm\mu}(x) + I_n^{\pm K}(x) \quad (4.23b);$$

where

$$f_n^{\pm\mu}(x) = \frac{1}{\sqrt{2\pi}} \left(\frac{2\,k_x\tan\Lambda}{\sqrt{1-M^2}}\right)^{n+1/2} \int_{C_1} \frac{d\lambda_1\, e^{-i\lambda_1 x}}{(\lambda_1-\mu)^{n+1}} \frac{1}{(\lambda_1+\mu)^{n+1/2}} \quad (4.24a),$$

$$f_n^{\pm K}(x) = \frac{1}{\sqrt{2\pi}} \int_{\text{Branch line at } \lambda_1=\pm K} \frac{d\lambda_1\, e^{-i\lambda_1 x}}{\sqrt{\lambda_1-\mu}} \left\{\frac{i}{\frac{k_x\tan\Lambda}{\sqrt{1-M^2}} - \sqrt{K^2-\lambda_1^2}}\right\}^{n+1/2} \quad (4.24b);$$

and

$$I_n^{\pm\mu}(x,Y) = -i\sqrt{\frac{\pi}{2}} \int_{-\infty}^{\infty} d\xi H_1^{(2)}\left(K\sqrt{(x-\xi)^2+Y^2}\right) \frac{KY}{\sqrt{(x-\xi)^2+Y^2}} f_n^{\pm\mu}(\xi) \quad (4.25a),$$

$$I_n^{\pm K}(x,Y) = -i\sqrt{\frac{\pi}{2}} \int_{-\infty}^{\infty} d\xi H_1^{(2)}\left(K\sqrt{(x-\xi)^2+Y^2}\right) \frac{KY}{\sqrt{(x-\xi)^2+Y^2}} f_n^{\pm K}(\xi) \quad (4.25b).$$

For n=0,1 $f_n^{\pm\mu}(x)$ can be calculated by deforming the contour C_1 in fig. 4.3 to C_1^*, or C_1^{**}, for x>0, x<0, respectively.

We then obtain

$$f_0^{\pm\mu}(x) = \frac{1}{\sqrt{2\pi}} \left(\frac{2k_x \tan\Lambda}{\sqrt{1-M^2}}\right)^{\frac{1}{2}} \frac{(-2\pi i)}{\sqrt{2\mu}} e^{-i\mu x} \begin{cases} 1 & \text{for } x>0 \\ 1 - (1+i)\, E^*[2\mu(-x)] & \text{for } x<0 \end{cases} \quad (4.26a),$$

$$f_1^{\pm\mu}(x) = \frac{1}{\sqrt{2\pi}} \left(\frac{k_x \tan\Lambda}{\sqrt{1-M^2}}\right)^{3/2} \frac{(-2\pi i)}{(2\mu)^{3/2}} e^{-i\mu x}$$

$$\begin{cases} -ix - \frac{3}{4\mu} & \text{for } x>0 \\ -i \int_{(-x)}^{\infty} d\xi [1-(1+i)\, E^*(2\mu\xi)] - \frac{1}{2\mu}[1-(1+i)E^*\{2\mu(-x)\}] + \\ -\frac{(1+i)}{\sqrt{2\mu}}\, e^{2i\mu x} \sqrt{\frac{2}{\pi}}\, \sqrt{-x} & \text{for } x<0 \end{cases} \quad (4.26b).$$

We have been able to calculate $f_n^{\pm\mu}(x)$ analytically for n=0,1. Unfortunately, the same cannot be done for the more complicated integrals in $f_n^{\pm K}(x)$, the contributions to $f_n(x)$ from the branch cuts at $\lambda_1 = \pm K$. However, we notice that these branch points are weak, and so, their contribution to $f(\xi)$ for large ξ should be small in comparison to that from $f_n^{\pm\mu}(\xi \to \infty)$. With this in mind we make the following approximation in (4.25b):

$$I_n^{\pm K}(x,Y) = -i\sqrt{\frac{\pi}{2}} \int_{-1/K}^{+1/K} d\xi H_1^{(2)}\left(K\sqrt{(x-\xi)^2 + Y^2}\right) \frac{KY}{\sqrt{(x-\xi)^2 + Y^2}} f_n^{\pm K}(\xi) \quad (4.27),$$

where we may now replace $f_n^{\pm K}(\xi)$ by its small-ξ behavior. The latter may be calculated by deforming C_1 to C_1^* and C_1^{**} in fig. 4.4 for x>0, x<0, respectively. The integrals which

result turn out to be related to the well-known Exponential integral, which for small argument (here, Kx=0) has the behavior indicated by Bender and Orszag,[26] pp. 251-252. The final expressions for $f_{\eta}^{\pm K}(\xi)$ are

$$f_{\eta}^{\pm K}(\xi) = \begin{cases} -\sqrt{\frac{2}{\pi}}\; i^{\eta} \sin\left[\frac{\pi}{2}(\eta+\frac{1}{2})\right] \frac{1}{K^{\eta}} \left[\frac{(-1)^{\eta+1}}{\eta!}\left(\gamma_o + \frac{\pi}{2} - \sum_{j=1}^{\eta}\frac{1}{j}\right)[K(-\xi)]^{\eta}\right. \\ \left. + \frac{(-1)^{\eta+1}}{\eta!}[K(-\xi)]^{\eta}\ln[K(-\xi)] - \sum_{\substack{j=0 \\ j\neq\eta}}^{\infty}(-i)^{j}\frac{i^{-\eta}}{j!}\frac{[K(-\xi)]^{j}}{(j-\eta)}\right] \text{for } \xi<0 \\ -\sqrt{\frac{2}{\pi}}\; i^{\eta+1}\sin\left[\frac{\pi}{2}(\eta+\frac{1}{2})\right]\frac{1}{K^{\eta}}\left[\frac{(-1)^{\eta+1}}{\eta!}\left(\gamma_o+\frac{\pi}{2}-\sum_{j=1}^{\eta}\frac{1}{j}\right)(K\xi)^{\eta}\right. \\ \left. + \frac{(-1)^{\eta+1}}{\eta!}(K\xi)^{\eta}\ln(K\xi) - \sum_{\substack{j=0 \\ j\neq\eta}}^{\infty}\frac{(-1)^{j}i^{-\eta}}{j!\,(j-\eta)}(K\xi)^{j}\right] \text{for } \xi>0 \end{cases} \qquad (4.28),$$

where γ_o is Euler's constant, approximately .577.

Since we are interested in the small-x and large-Y behavior of $I_{\eta}^{\pm\mu}(x,Y)$, we may approximate the Hankel function in (4.20) by its form for large argument. Equation (4.25a) then becomes

$$I_{\eta}^{\pm\mu}(x,Y) \cong \frac{K}{\sqrt{KY}}\, e^{\frac{i\pi}{4} - iKY}\int_{-\infty}^{\infty} d\xi\; e^{\frac{ikx\xi}{Y}} f_{\eta}^{\pm\mu}(\xi) \qquad (4.29),$$

and similarly for $I_{\eta}^{\pm K}(x,Y)$, but with limits of integration -1/K and +1/K. In $I_{\eta}^{\pm K}(x,Y)$ we may also make the approximation $\exp(iKx\,\xi/Y)=1+iKx\,\xi/Y$.

Performing the integrations in $I_{\eta}^{\pm\mu}$ and $I_{\eta}^{\pm K}$, and substituting the resulting expressions into (4.18), we obtain the first two terms in the asymptotic expansion for the

loading as we approach the leading edge

$$p_* = p_{*2\text{-}D} + \frac{(i-1)\,\rho_0 w_0}{2\pi\sqrt{1-M^2}} \frac{U}{\sqrt{\frac{k_x}{1-M^2}+\mu}} \frac{e^{-\frac{i\pi}{4} - iKY}}{\sqrt{Y}} \frac{1}{\sqrt{KY}} \left\{ \left[\left(\frac{K}{\mu}\right) \right.\right.$$

$$\left.\left. \left(\frac{k_x \tan\Lambda}{\sqrt{1-M^2}}/\mu\right)^{\frac{1}{2}} \frac{1}{\left(1-\frac{Kx}{\mu Y}\right)} \left\{ \frac{\sqrt{2}}{\sqrt{1+\frac{Kx}{\mu Y}}} - 2 \right\} \frac{-i}{\pi} \left(C_1^\circ + \frac{ix}{Y} C_2^\circ\right) \right] + \right.$$

$$\left(\frac{\lambda_{sound}}{y}\right) \left[\frac{3i\sqrt{1-M^2}}{2\pi} \left\{ \left(\frac{K}{\mu}\right)^2 \left(\frac{k_x \tan\Lambda}{\sqrt{1-M^2}}/\mu\right)^{3/2} \right\} \frac{1}{\left(1-\frac{Kx}{\mu Y}\right)} \cdot \right.$$

$$\left(\frac{2}{\left(1-\frac{Kx}{\mu Y}\right)} \left(\frac{\sqrt{2}}{\sqrt{1+\frac{Kx}{\mu Y}}} - 2 \right) - 3 \frac{+\sqrt{2}}{\sqrt{1+\frac{Kx}{\mu Y}}} \right) - \frac{\sqrt{2}}{\left(1+\frac{Kx}{\mu Y}\right)^{3/2}} \Bigg\}$$

$$\left. \left. - \frac{2}{\pi} e^{-i\pi/4} \left(C_1^1 + C_2^1 \frac{ix}{Y}\right) \right\} \right] + O\left(\frac{\lambda_{sound}}{y}\right)^2 \Bigg\} \qquad (4.30);$$

where λ_{sound} stands for the acoustic wavelength and

$$C_1^\circ = -\left(\frac{\pi}{2} + \gamma_\circ\right) + 1 - \sum_{j=1}^{\infty} \frac{(-i)^j}{j!\,j\,(j+1)} \qquad (4.31a),$$

$$C_2^\circ = -\frac{1}{2}\left(\frac{\pi}{2} + \gamma_\circ\right) + \frac{1}{4} - \sum_{j=1}^{\infty} \frac{(-i)^j}{j!\,j} \frac{1}{(j+2)} \qquad (4.31b),$$

$$C_1^1 = \frac{1}{2}\left(\gamma_\circ + \frac{\pi}{2} - \frac{1}{2}\right) - i - \sum_{j=2}^{\infty} \frac{(-i)^{j+1}}{j!\,(j-1)} \frac{1}{(j+1)} \qquad (4.31c),$$

$$C_2^1 = \frac{1}{3}\left(\gamma_\circ + \frac{\pi}{2} - \frac{2}{3}\right) - \frac{i}{2} - \sum_{j=2}^{\infty} \frac{(-i)^{j+1}}{j!\,(j-1)(j+2)} \qquad (4.31d).$$

Figure 4.5a is a plot vs. x/y of the magnitude of the first term in square brackets for n=0 in the asymptotic series (4.30) for the correction to the two-dimensional loading near the leading edge; the values of M and Λ are 0.8

and 62°. Since we interested here in the case of subsonic trace speed of the disturbance, in the plot the quantity μ has been replaced by $-i\sqrt{-\mu^2}$, as previously discussed. Note that the first corrective term is larger on the plate side than upstream, as we should expect. Figure 4.5b is a similar graph for the second term in square brackets appearing in (4.30), corresponding to the n=1 term in the asymptotic. As indicated, this term is to be multiplied by the ratio of the acoustic wavelength to the distance from the side edge.

Next we investigate the behavior of (4.17) near the side edge Y=0+. Expanding the Fresnel integral for small arguments we have that as Y approaches 0+

$$p_*(\bar{x},Y>0,0) = \frac{(i-1)\,\rho_0 w_0}{2\pi\sqrt{1-M^2}}\,\frac{U}{\sqrt{\frac{k_x}{1-M^2}+\mu}}$$

$$\sqrt{\frac{2}{\pi}}\sum_{\eta=0}^{\infty}(-i)^{\eta}\,\frac{2^{2\eta}\,\eta!}{(2\eta+1)!}\,Y^{\eta+1/2}\int_{C_1}\frac{d\lambda_1 e^{-i\lambda_1 x}}{\sqrt{\lambda_1-\mu}}\left[\frac{(k_x\tan\Lambda}{\sqrt{1-M^2}}-\sqrt{K^2-\lambda_1^2}\right]^{\eta+1/2} \quad (4.32).$$

We now call

$$\tilde{I}_{\eta}(x) = \int_{C_1}\frac{d\lambda_1 e^{-i\lambda_1 x}}{\sqrt{\lambda_1-\mu}}\left(\frac{k_x\tan\Lambda}{\sqrt{1-M^2}}-\sqrt{K^2-\lambda_1^2}\right)^{\eta+1/2} \quad (4.33),$$

and recall (4.22) in order to study the contributions from the points $\lambda_1=\pm\mu$. It follows that

$$\tilde{I}_{\eta}^{\pm\mu}(x) = \frac{1}{\left(\frac{2\,k_x\tan\Lambda}{\sqrt{1-M^2}}\right)^{\eta+1/2}}\int_{C_1} d\lambda_1 e^{-i\lambda_1 x}(\lambda_1-\mu)^{\eta}(\lambda_1+\mu)^{\eta+1/2} \quad (4.34);$$

which indicates that $\tilde{I}_n^{\pm\mu}(x>0)=0$. For $x<0$ we deform C_1 to C_1^{**} in fig. 4.3 and find that

$$\tilde{I}^{\pm\mu}(x>0) = \frac{(-i)\, e^{-i\mu x}}{\left(2\frac{k_x\tan\Lambda}{\sqrt{1-M^2}}\right)^{n+1/2}} \frac{d^n}{d(-x)^n} \int_{C_1^{**}} d\lambda_1 e^{i(\lambda_1-\mu)} (-x)^{(\lambda_1+\mu)^{n+1/2}}$$

$$= \frac{2\,(-1)^n \sin\left[\pi\left(n+\frac{1}{2}\right)\right]\Gamma\left(n+\frac{3}{2}\right)}{\left(2\frac{k_x\tan\Lambda}{\sqrt{1-M^2}}\right)^{n+1/2}} \frac{d^n}{d(-x)^n} \frac{e^{i\mu}(-x)}{(-x)^{n+\frac{3}{2}}} \qquad (4.35).$$

In order to calculate $\tilde{I}_n^{\pm K}(x)$ for $x>0$ and $x<0$, we deform C_1 to C_1^* and C_1^{**} in figure 4.4, respectively. The results are

$$\tilde{I}_n^{\pm K}(x) = (1-i)\sqrt{\pi}\left(\frac{k_x\tan\Lambda}{\sqrt{1-M^2}}\right)^{n-\frac{1}{2}} \sqrt{\frac{K}{K-\mu}}\left(n+\frac{1}{2}\right)\frac{e^{-iKx}}{x^{3/2}} \quad \text{for } x>0 \qquad (4.36a),$$

$$\tilde{I}_n^{\pm K}(x) = -(1+i)\sqrt{\pi}\left(\frac{k_x\tan\Lambda}{\sqrt{1-M^2}}\right)^{n-1/2}\sqrt{\frac{K}{K+\mu}}\,(n+1/2)\frac{e^{iKx}}{(-x)^{3/2}} \quad \text{for } x<0 \qquad (4.36b).$$

Substituting for $\tilde{I}_n^{\pm\mu}(x)$ and $\tilde{I}_n^{\pm K}(x)$ back into (4.32), we obtain the behavior of p_* near the side edge (the n=0 term):

$$p_* \cong \frac{(i-1)\,\rho_0 w_0}{4\sqrt{\pi}\sqrt{1-M^2}} \frac{U}{\sqrt{\frac{k_x}{1-M^2}+\mu}} \frac{\gamma^{1/2}}{\sqrt{\frac{k_y\tan\Lambda}{(1-M^2)^{1/2}}}}$$

$$\begin{cases} \left[(1-i)\, e^{i\mu x} - (1+i)\sqrt{\frac{K}{K+\mu}}\, e^{iKx}\right]\frac{1}{(-x)^{3/2}} & \text{for } x<0 \\ (1-i)\sqrt{\frac{K}{K-\mu}}\, e^{-iKx}\,\frac{1}{x^{3/2}} & \text{for } x>0 \end{cases} \qquad (4.37),$$

which has the required behavior for Y=0+ for x>0. For both x<0 and x>0 we see that the solution behaves as $1/|x|^{3/2}$, where x, recall, is normalized by the acoustic wavelength.

In summary, in this chapter we have obtained an approximate solution for the pressure field surrounding a quarter-infinite plate passing at high speed through an oblique gust. The problem was motivated by the need for a better model for the strength of acoustic dipoles near the tip of a blade passing over a vortex when the interaction angle is such that the resulting disturbance travels subsonically through the still fluid; that developed in chapter 3 overestimated the strength of these tip acoustic dipoles.

We arrived at an expression for the loading on the plate (eqn. (4.17)) which we later went on to show satisfied the required edge conditions. Also, we showed that away from the side edge this result approached asymptotically that obtained earlier in chapter 2 for the two-dimensional loading, which vanishes upstream and has the $1/\sqrt{x}$ behavior on the plate; it turned out that this was by far the dominant term in the calculated asymptotic series. We conclude then that the result in (4.15), from which the loading was calculated by setting Z=0, is a good approximation for the pressure field for high-reduced frequencies.

Normally, the next step at this point would have been to translate the solution from the present reference frame fixed on the plate to one fixed on the ground or still fluid.

Unfortunately, the small amount by which we violate the upstream boundary condition of $P(x<0,y>0,0)=0$ then becomes unfairly magnified by the forward enhancement effect of traveling sources, essentially the same $(1+Mx_a/r_a)^{-2}$ factor present in eqn (3.14) for that other ground-frame solution. The only course left for us now seems to be to extract rationally from (4.17) an approximate representation for the loading which keeps the physical features we have worked so hard to get - the edge behaviors, but that at the same time vanishes upstream. This task we undertake in the first part of chapter 5 and obtain a relatively simple expression which allows us to reintroduce the trailing edge into the model. Since so much of the analysis in chapter 5 depends on the loading expression in (4.17), we rederive the latter next by an independent method, a method based on the idea of source cancellations and first used by Landahl[10] to solve unsteady transonic flow problems.

Appendix: Calculation of loading by source cancellations

We seek a load function $p_*^{(s)}(x,Y,0)$ which when added to $p_*^{(1)}(x,Y,0)$, the two-dimensional loading from the leading-edge problem given in eqn. (2.15), we will have $p_*^{(1)}+p_*^{(s)}=0$ for $Y<0$. The superscript s stands for "side-edge". The boundary-value problem for $p_*^{(s)}$ is

$$p_{*xx}^{(s)} + p_{*YY}^{(s)} + p_{*ZZ}^{(s)} + K^2 p_*^{(s)} = 0 \qquad (4.38),$$

with

$$p_*^{(s)}(x,Y<0,0) = - p_*^{(1)}(x,Y,0) \qquad (4.39a),$$

$$p_{*Z}^{(s)}(x,Y>0,0) = 0 \qquad (4.39b),$$

We define the transform pair

$$\tilde{p}_*^{(s)}(\lambda_1,Y,0) = \int_{-\infty}^{\infty} \frac{dx}{\sqrt{2\pi}}\, e^{i\lambda_1 x}\, p_*^{(s)}(x,Y,0) \qquad (4.40a),$$

$$p_*^{(s)}(x,Y,0) = \int_{-\infty}^{\infty} \frac{d\lambda_1}{\sqrt{2\pi}}\, e^{-i\lambda_1 x}\, \tilde{p}_*^{(s)}(\lambda_1,Y,0) \qquad (4.40b),$$

and apply (4.40a) to (4.38) and (4.39a,b). The resulting boundary-value problem for $\tilde{p}_*^{(s)}$ is

$$\tilde{p}_{*YY}^{(s)} + \tilde{p}_{*ZZ}^{(s)} + (K^2 - \lambda_1^2)\, \tilde{p}_*^{(s)} = 0 \qquad (4.41),$$

with

$$\tilde{p}_*^{(s)}(\lambda_1,Y<0,0) = - \tilde{p}_*^{(1)}(\lambda_1,Y,0) \qquad (4.42a),$$

$$\tilde{p}_{*Z}^{(s)}(\lambda_1,Y>0,0) = 0 \qquad (4.42b).$$

Landahl[19] has shown that $\tilde{p}_*^{(s)}(\lambda_1,Y>0)$ may be obtained by the integral

$$\tilde{p}_*^{(s)}(\lambda_1,Y>0,0) = -\frac{1}{\pi} \int_0^{\infty} d\eta\, \tilde{p}_*^{(1)}(\lambda_1,-\eta,0)\, \frac{e^{-i\sqrt{K^2-\lambda_1^2}\,(\eta+Y)}}{\eta+Y} \sqrt{\frac{Y}{\eta}} \qquad (4.43).$$

Substituting for $p_*^{(1)}$, which from eqn. (2.14) we see is (with the $\exp[-ik_x \tan\Lambda\, Y/\sqrt{1-M^2}]$ term included)

$$\tilde{p}_*^{(1)}(\lambda_1, Y, 0+) = -\frac{\rho_0 w_0}{\sqrt{2\pi}} \frac{U}{\sqrt{1-M^2}} \frac{1}{\sqrt{\frac{k_x}{1-M^2} + \mu}} \frac{1}{\sqrt{\lambda_1 - \mu}} e^{-\frac{ik_x \tan\Lambda\, Y}{\sqrt{1-M^2}}}$$

into (4.43) we obtain that for $Y>0$,

$$\tilde{p}_*^{(s)}(\lambda_1, Y>0, 0) = \frac{\rho_0 w_0}{\sqrt{2\pi}} \frac{1}{\sqrt{1-M^2}} \frac{1}{\sqrt{\frac{k_x}{1-M^2} + \mu}} \frac{1}{\sqrt{\lambda_1 - \mu}} e^{-\frac{ik_x \tan\Lambda\, Y}{\sqrt{1-M^2}}}$$

$$\cdot\{1 - (1-i)\, E\left[Y\left(\frac{k_x \tan\Lambda}{\sqrt{1-M^2}} - \sqrt{K^2 - \lambda_1^2}\right)\right]\} \qquad (4.44),$$

so that for $Y>0$

$$\tilde{p}_*^{(1)} + \tilde{p}_*^{(s)} = \frac{(i-1)\, \rho_0 w_0}{\sqrt{2\pi}} \frac{U\, e^{-\frac{ik_x \tan\Lambda\, Y}{\sqrt{1-M^2}}}}{\sqrt{1-M^2}\sqrt{\frac{k_x}{1-M^2} + \mu}} \frac{1}{\sqrt{\lambda_1 - \mu}} E\left[Y\left(\frac{k_x \tan\Lambda}{\sqrt{1-M^2}} - \sqrt{K^2 - \lambda_1^2}\right)\right] \qquad (4.45),$$

from which we finally find that

$$p_*^{(1)} + p_*^{(s)} = \frac{(i-1)\, \rho_0 w_0}{2\pi} \frac{U\, e^{-\frac{ik_x \tan\Lambda Y}{\sqrt{1-M^2}}}}{\sqrt{1-M^2}\sqrt{\frac{k_x}{1-M^2} + \mu}} \qquad (4.46).$$

$$\int_{-\infty}^{\infty} \frac{d\lambda_1}{\sqrt{\lambda_1 - \mu}} e^{-i\lambda_1 x} E\left[Y\left(\frac{k_x \tan\Lambda}{\sqrt{1-M^2}} - \sqrt{K^2 - \lambda_1^2}\right)\right]$$

Chapter 5: Aeroacoustic model for a blade of semi-infinite span with improved side-edge loading

In chapter 2 we saw that the effect of the passage of a two-dimensional airfoil through a gust is essentially one of diffraction. That is, the pressure field and loading for the interaction with a single gust of wavenumber $\omega b/U$ is given by a continuum of wavenumber solutions - recall eqn. (2.14) for the leading-edge effect, for example.

For the three-dimensional wing with side edge, a similar diffraction of the gust spanwise wavenumber $k_x \tan\Lambda$ must occur in the y direction. With $Z=0+$, the λ_2 integral in eqn. (4.16) gives the side-edge diffraction loading predicted in our model. We observe that besides the pole at $\lambda_2 = k_x \tan\Lambda/\sqrt{1-M^2}$, the integrand also has a branch point at $\lambda_2 = \sqrt{K^2-\lambda_1^2}$. For large Y, the pole term gives the predicted spanwise loading the same simple sinusoidal $\exp(-ik_x \tan\Lambda Y/\sqrt{1-M^2})$ behavior as that of the infinite-span wing - the spanwise variation of the input gust upwash; it is the only term present in the Y transform of the cut-off loading model later developed in this chapter (see eqn. (5.21) below). The branch point singularity at $\lambda_2 = \sqrt{K^2-\lambda_1^2}$, therefore, is responsible for the departure of the loading in (4.16) (for Z=0) from its two-dimensional form for arbitrary Y. We may say that this is the part of the λ_2 integrand which provides the spanwise diffraction effect for the loading: it allows the loading to behave in magnitude as $\sqrt{y}$ at the side edge and, as we find from the analysis below, causes it to have a phase variation near the side very

different from that assumed in chapter 3 and in the cut-off model of this chapter. Notice that (4.16) also indicates that the predicted leading- and side-edge diffractions are not independent (even for Z=0). If they were, the integrand would be a product of two functions: one depending on λ_1 alone; and the other on λ_2. Rather, we observe a coupling.

The analysis here begins with (4.17). Rationally, we make a high-frequency and large interaction angle Λ approximation which essentially eliminates the coupling between the leading- and side-edge effects. This allows us to obtain an approximate, but closed-form, lifting-surface theory for the passage of a quarter-infinite plate through an oblique gust. The resulting aerodynamic model predicts the strength and phase of tip dipoles more accurately than that of chapter 3. Yet, it is still simple enough to allow us to calculate the acoustic field in closed form.

As mentioned above, in this chapter we also develop a cut-off aeroacoustic model analogous to that of chapter 3: we look at the acoustic field due to a loading pattern given by the two-dimensional loading from chapter 2 for $y>0$, and by 0 for $y<0$.

Approximate lifting-surface theory

In chapter 4 we developed an approximate expression for the loading on a quarter-infinite plate passing through a gust. This result was derived first by the Wiener-Hopf technique and given in eqn. (4.17), and then again by the

method of source cancellations and presented in (4.46). For convenience we write it once more.

$$p_* = \frac{(i-1)\,\rho_0 w_0}{2\pi\sqrt{1-M^2}} \frac{U\, e^{\frac{-ik_x \tan\Lambda Y}{\sqrt{1-M^2}}}}{\sqrt{\frac{k_x}{1-M^2}+\mu}} \int_{-\infty}^{\infty} \frac{d\lambda}{\sqrt{\lambda-\mu}}\, e^{-i\lambda x}\, E\left[Y\left(\frac{k_x \tan\Lambda}{\sqrt{1-M^2}} - \sqrt{k^2-\lambda^2}\right)\right] \quad (5.1).$$

The integral in this solution may be re-expressed by means of the convolution theorem as

$$(i-1) \int_0^{\infty} \frac{d\xi}{\sqrt{\xi}}\, e^{-i\mu\xi}\, g(x-\xi) \quad (5.2),$$

where

$$g(x) = \int_{-\infty}^{\infty} \frac{d\lambda}{\sqrt{2\pi}}\, e^{-i\lambda x}\, E\left[Y\left(\frac{k_x \tan\Lambda}{\sqrt{1-M^2}} - \sqrt{K^2-\lambda^2}\right)\right] \quad (5.3).$$

We now split the integral in (5.3) into three segments, as indicated by (5.4); and then for each segment interchange orders of integration with the Fresnel integrals. The resulting set of integrals is given in (5.5).

$$\sqrt{2\pi}\, g(x) = \int_{-\infty}^{-K} + \int_{-K}^{K} + \int_{K}^{\infty} \quad (5.4).$$

$$\sqrt{2\pi}\, g(x) = \int_0^{Y\left[\frac{k_x \tan\Lambda}{\sqrt{1-M^2}} - K\right]} \frac{dt\, e^{it}}{\sqrt{2\pi t}} \int_{-K}^{K} d\lambda\, e^{-i\lambda x} +$$

$$\int_{Y\left[\frac{k_x \tan\Lambda}{\sqrt{1-M^2}} - K\right]}^{Y\frac{k_x \tan\Lambda}{\sqrt{1-M^2}}} \frac{dt\, e^{it}}{\sqrt{2\pi t}} \int_{-\sqrt{K^2-\left(\frac{t}{Y}-\frac{k_x \tan\Lambda}{\sqrt{1-M^2}}\right)^2}}^{+\sqrt{K^2-\left(\frac{t}{Y}-\frac{k_x \tan\Lambda}{\sqrt{1-M^2}}\right)^2}} d\lambda e^{-i\lambda x} +$$

$$\int_0^{Y\frac{k_x\tan\Lambda}{\sqrt{1-M^2}}} \frac{dt\, e^{it}}{\sqrt{2\pi t}} \int_K^{\infty} d\lambda e^{-i\lambda x} + \int_{Y\frac{k_x\tan\Lambda}{\sqrt{1-M^2}}}^{Y\frac{k_x\tan\Lambda}{\sqrt{1-M^2}}+i\infty} \frac{dt\, e^{it}}{\sqrt{2\pi t}} \int_{\sqrt{K^2-(\frac{t}{Y}-\frac{k_x\tan\Lambda}{\sqrt{1-M^2}})^2}}^{\infty} d\lambda e^{-i\lambda x}$$

$$+ \int_0^{Y\frac{k_x\tan\Lambda}{\sqrt{1-M^2}}} \frac{dte^{it}}{\sqrt{2\pi t}} \int_{-\infty}^{-K} d\lambda e^{-i\lambda x}$$

$$\int_{Y\frac{k_x\tan\Lambda}{\sqrt{1-M^2}}}^{Y\frac{k_x\tan\Lambda}{\sqrt{1-M^2}}+i\infty} \frac{dt\, e^{it}}{\sqrt{2\pi t}} \int_{-\infty}^{-\sqrt{K^2-(\frac{t}{Y}-\frac{k_x\tan\Lambda}{\sqrt{1-M^2}})^2}} d\lambda e^{-i\lambda x} \qquad (5.5).$$

These may be further manipulated into a new set of terms, (5.6), where we number each term (1) through (5) for ease of reference in the discussion which follows:

(1) $2\pi\delta(x)\, E\left[Y\left(\frac{k_x\tan\Lambda}{\sqrt{1-M^2}} - K\right)\right] +$

(2) $-2\,\frac{\sin Kx}{x}\left\{E\left[Y\,\frac{k_x\tan\Lambda}{\sqrt{1-M^2}}\right] - E\left[Y\left(\frac{k_x\tan\Lambda}{\sqrt{1-M^2}} - K\right)\right]\right\} +$

(3) $2\pi\delta(x) \int_{Y\frac{k_x\tan\Lambda}{\sqrt{1-M^2}}}^{Y\frac{k_x\tan\Lambda}{\sqrt{1-M^2}}+i\infty} \frac{dt\, e^{it}}{\sqrt{2\pi t}} +$

(4) $\int_{Y(\frac{k_x\tan\Lambda}{\sqrt{1-M^2}}-K)}^{Y\frac{k_x\tan\Lambda}{\sqrt{1-M^2}}} \frac{dt\, e^{it}}{\sqrt{2\pi t}} \int_{-\sqrt{K^2-(\frac{t}{Y}-\frac{k_x\tan\Lambda}{\sqrt{1-M^2}})^2}}^{\sqrt{K^2-(\frac{t}{Y}-\frac{k_x\tan\Lambda}{\sqrt{1-M^2}})^2}} d\lambda e^{-i\lambda x} +$

(5)

$$-\int_{Y\frac{k_x\tan\Lambda}{\sqrt{1-M^2}}}^{Y\frac{k_x\tan\Lambda}{\sqrt{1-M^2}}+i\infty}\frac{dt\,e^{it}}{\sqrt{2\pi t}}\int_{-\sqrt{K^2-(\frac{t}{Y}-\frac{k_x\tan\Lambda}{\sqrt{1-M^2}})^2}}^{\sqrt{K^2-(\frac{t}{Y}-\frac{k_x\tan\Lambda}{\sqrt{1-M^2}})^2}}d\lambda\,e^{-i\lambda x} \qquad (5.6).$$

Since $E(\infty)=(1+i)/2$, we observe that for large Y terms (2)-(5) vanish; we are left with (1) only.

For Y=0+, integrals (3) and (5) may be deformed in the complex t plane from the positive real axis to the positive imaginary axis (and the contribution from the arc at infinity is zero). We then obtain, for terms (3) and (5) respectively

$$-e^{i\pi/4}\int_0^\infty\frac{d\xi e^{-\xi}}{\sqrt{2\pi\xi}}\int_{-\sqrt{K^2+\xi^2/Y^2}}^{\sqrt{K^2+\xi^2/Y^2}}d\lambda e^{-i\lambda x} \qquad (5.7a),$$

$$e^{i\pi/4}\int_0^\infty\frac{d\xi e^{-\xi}}{\sqrt{2\pi\xi}}\cdot 2\pi\delta(x) \qquad (5.7b),$$

For $Y\to 0+$, the inside integral in (5.7a) becomes $2\pi\delta(x)$; so that the first-order contribution of (3) + (5) to (5.6) near the side edge is zero. Higher-order contributions vanish as well.

In order to obtain the behavior of integral (4) for $Y\to 0+$, we integrate by parts as follows:

$$\lim_{Y\to 0+}(4)\simeq\sqrt{\frac{2}{\pi}}\sqrt{t}\,e^{it}\int_{-\sqrt{K^2-(\frac{t}{Y}-\frac{k_x\tan\Lambda}{\sqrt{1-M^2}})^2}}^{\sqrt{K^2-(\frac{t}{Y}-\frac{k_x\tan\Lambda}{\sqrt{1-M^2}})^2}}d\lambda e^{-i\lambda x}\Bigg|_{t=Y\frac{k_x\tan\Lambda}{\sqrt{1-M^2}}}^{t=Y(\frac{k_x\tan\Lambda}{\sqrt{1-M^2}}-K)} \qquad (5.8a),$$

$$= \sqrt{\frac{2}{\pi}}\, e^{\frac{ik_x \tan\Lambda Y}{\sqrt{1-M^2}}} \sqrt{\frac{k_x \tan\Lambda Y}{(1-M^2)^{1/2}}}\ \frac{2\sin Kx}{x} \qquad (5.8b),$$

which may be interpreted as the small-Y behavior of

$$\lim_{Y\to 0+} (4) = \frac{2\sin Kx}{x}\, E\left[Y \frac{k_x \tan\Lambda}{\sqrt{1-M^2}} \right] \qquad (5.9).$$

We conclude that near the side edge integral (4) cancels the first term of (2); so that the behavior of the sum of all terms in (5.6) for $Y \to 0+$ is

$$\sqrt{2\pi}\, g(x) \simeq \{2\pi\delta(x) + \frac{2\sin Kx}{x}\} E\left[Y\left(\frac{k_x \tan\Lambda}{\sqrt{1-M^2}} - K\right)\right] \qquad (5.10a),$$

from which

$$\sqrt{2\pi}\ \ g(x-\xi) \simeq \left\{ 2\pi\delta(x-\xi) + \frac{2\sin [K(x-\xi)]}{x-\xi} \right\} E\left[Y\left(\frac{k_x \tan\Lambda}{\sqrt{1-M^2}} - K\right)\right] (5.10b).$$

We note now that near the leading edge ($x \to 0$), the second term in curly brackets in (5.10b) behaves essentially as $2K$ for $\xi = 0$. In the convolution (5.2), it contributes a term proportional to the constant $K/\sqrt{|\mu|}$, which besides being small for large interaction angles Λ ($|\mu| >> K$), does not contain the $1/\sqrt{x}$ singularity for the loading near $x=0+$, and so may be neglected in favor of the $2\pi\delta(x-\xi)$ term in (5.10b).

In summary, we find that for both near the side edge, and away from it, we may make the approximation

$$\sqrt{2\pi}\, g(x-\xi) = 2\pi\delta(x-\xi)\; E\left[\gamma\left(\frac{k_x \tan\Lambda}{\sqrt{1-M^2}} - K\right)\right]$$

Evaluating the convolution (5.2), we finally obtain the approximate lifting-surface result for a quarter-infinite plate passing through a gust a large interaction angle Λ (subsonic trace speed of disturbances):

$$p_*(x,Y>0,0) = i\sqrt{\frac{2}{\pi}}\,\frac{\rho_0 w_0 U}{\sqrt{1-M^2}}\,\frac{e^{-i\mu x - i\frac{k_x Y \tan\Lambda}{\sqrt{1-M^2}}}}{\sqrt{\frac{k_x}{1-M^2}+\mu}}\,\frac{1}{\sqrt{x}}\; E\left[\gamma\left(\frac{k_x \tan\Lambda}{\sqrt{1-M^2}} - K\right)\right] \quad (5.11a),$$

which, since $E(a \tilde{=} 0) \simeq \sqrt{\frac{2}{\pi}}\sqrt{a}\, e^{ia}$ indicates that

$$p_*(x,Y\to 0^+,0) \simeq i\,\frac{2}{\pi}\,\frac{\rho_0 w_0 U}{\sqrt{1-M^2}}\,\frac{1}{\sqrt{\frac{k_x}{1-M^2}+\mu}}\,\frac{e^{-i\mu x}}{\sqrt{x}}\; e^{-iKY}\sqrt{Y}\left(\frac{k_x \tan\Lambda}{\sqrt{1-M^2}} - K\right)^{1/2} \quad (5.11b).$$

We find that the Y variation of the loading phase near the side is given by $\exp(-iKY)$, rather than by $\exp(-ik_x \tan\Lambda Y/\sqrt{1-M^2})$, as in chapter 3 and in the cut-off model developed later in the present chapter. Since the rate of decay of the dipole strength near the side is given by the constant $(k_x \tan\Lambda - K)^{1/2}$, which is $>>K$ for large Λ, we notice that the spanwise variation of dipole phase is small throughout the region we call the "tip region" (fig. 5.1). For large Λ, therefore, the phase of the spanwise loading may be regarded as constant for Y=0+.

The uncoupling of the load into the product of a function of x and one of Y allows us now to cancel the

solution in the wake by the procedure used in chapter 2 for the trailing-edge problem. As we would expect at this point, the expression for the pressure distribution on the semi-infinite span blade with side edge turns out to be

$$p_*(x>0,Y>0,0) = i\sqrt{\frac{2}{\pi}}\,\frac{\rho_0 w_0\, U}{\sqrt{\frac{k_x}{1-M^2}+\mu}}\; e^{\frac{-ik_x \tan\Lambda\, Y - i\mu x}{\sqrt{1-M^2}}}$$

$$E\left[\frac{Y(k_x\tan\Lambda}{\sqrt{1-M^2}} - K)\right]\left\{\frac{1}{\sqrt{x}} - \frac{1}{\sqrt{2}}\left[1-(1+i)\,E^*\left[2\mu(2-x)\right]\right]\right\} \qquad (5.12).$$

which becomes the two-dimensional loading far from the side edge as it should.

Acoustic field for a semi-infinite span blade with side edge passing through an oblique gust

As we noted above, the simplified loading expression allows us to solve a new trailing edge problem; the details of this analysis are no different from those in chapter 2 and so will be omitted here. We now define a pressure $P(x,Y,Z,t)=\tilde{p}_*(x,Y,Z,t)\exp(i\omega t+ik_x M^2 x/(1-M^2))$, which is a solution of

$$\tilde{p}_{*xx} + \tilde{p}_{*YY} + \tilde{p}_{*ZZ} + K^2\tilde{p}_* = 0 \qquad (5.13),$$

subject to

$$\tilde{p}_*(x,Y,0) = p_*(x,Y,0) \qquad (5.14),$$

the load we have calculated above for a semi-infinite blade passing through a gust. The solution procedure of this boundary-value problem is similar to that in chapter 3 for the rectangular rotating blade. Only one new integral comes up which we did not have before: the Fourier transform of a Fresnel integral;

$$\int_0^\infty dY\, e^{i(\lambda_1 - \frac{k_x \tan\Lambda}{\sqrt{1-M^2}})Y}\, E\left[Y\left(\frac{k_x \tan\Lambda}{\sqrt{1-M^2}} - K\right)\right] \qquad (5.15),$$

which exists for $Im(\lambda_2) > Im(k_x \tan\Lambda/\sqrt{1-M^2})$ and may be readily calculated either by integration by parts, or by interchanging orders of integration. Thus, we obtain that it is equal to

$$\frac{\sqrt{\pi}\, e^{\frac{3\pi i}{4}} \sqrt{\frac{k_x \tan\Lambda}{\sqrt{1-M^2}} - K}}{\left(\lambda_2 - \frac{k_x \tan\Lambda}{\sqrt{1-M^2}}\right)\sqrt{\lambda_2 - K}} \qquad (5.16),$$

At this point we allow $r_a = \sqrt{x_a^2 + y^2 + z^2} \to \infty$, and obtain the far-field pressure by the method of stationary phase. The procedure is completely analogous to that presented in detail in chapter 3. The final result for the acoustic signal $P(r_a, \gamma, \phi, t)$ perceived by an observer on the ground is

$$P(r_a, \gamma, \phi, t) \underset{r_a \to \infty}{\sim} -i \frac{\rho_0 w_0 U M}{2\pi \sqrt{\frac{k_x}{1-M^2} + \mu}} \sqrt{\tan\Lambda - \frac{M}{\sqrt{1-M^2}}}\, \frac{e^{\frac{i\omega}{1+M\sin\phi\cos\gamma}(t - br_a/c_a)}}{r_a} \cdots D_{\sqrt{\gamma}}(\gamma, \phi) \qquad (5.17),$$

where the "$\sqrt{y}$" subscript on $D_{\sqrt{y}}(\gamma,\phi)$ stands for $\sqrt{y}$-load behavior at the side edge. $D_{\sqrt{y}}(\gamma,\phi)$ was found to be

$$D_{\sqrt{y}}(\gamma,\phi) =$$

$$\cos\phi \left\{ \frac{1}{\left\{ \frac{M}{\sqrt{1-M^2}} \left(\frac{\sin\phi\cos\gamma+M}{1+M\sin\phi\cos\gamma} \right) + i\sqrt{\tan^2\Lambda - \frac{M^2}{1-M^2}} \right\}^{1/2} + \right.$$

$$\frac{i\sqrt{2}\left[\tan^2\Lambda - \frac{M^2}{1-M^2}\right]^{1/4}}{\left\{ \tan^2\Lambda - \frac{M^2}{1-M^2} + \left[\frac{M}{\sqrt{1-M^2}} \left(\frac{\sin\phi\cos\gamma + M}{1+M\sin\phi\cos\gamma} \right) \right]^2 \right\}^{1/2}} \cdot \left[\right.$$

$$\left. \left. 1 - (1+i)\, E^* \left[\frac{2k_x}{\sqrt{1-M^2}} \left\{ -i\sqrt{\tan^2\Lambda - \frac{M^2}{1-M^2}} - \frac{M}{\sqrt{1-M^2}} \left(\frac{\sin\phi\cos\gamma+M}{1+M\sin\phi\cos\gamma} \right) \right\} \right] \right] \right\}$$

$$\left(\frac{1}{\frac{M\sin\phi\sin\gamma}{1+M\sin\phi\cos\gamma} - \tan\Lambda} \right) \frac{1}{\sqrt{1 - \frac{(1-M^2)^{1/2}\sin\phi\sin\gamma}{1+M\sin\phi\cos\gamma}}} \qquad (5.18),$$

the three-dimensional function which describes the acoustic directivity pattern in terms of the spherical angles γ, ϕ in fig. 5.2.

Notice that the blade's tip is located at the origin, so that its semi-infinite span extends out from Y=0. This is in contrast to the system we had in chapter 3, where the blade tip was rightfully "outboard." Still, here as in chapter 3 the interaction angle Λ is such that the trace velocity of the unsteady blade loading is in the positive Y direction.

Acoustic field for a semi-infinite blade with square cut-off loading

Here we write down the solution of the boundary-value problem for $\tilde{p}_*(x,Y,Z)$:

$$\tilde{p}_{*_{XX}} + \tilde{p}_{*_{YY}} + \tilde{p}_{*_{ZZ}} + K^2\tilde{p}_* = 0 \qquad (5.19),$$

with

$$\tilde{p}_*(x,Y,0) = p_{*_{2-D}}(x,Y,0) \quad \text{for } Y > 0 \qquad (5.20a),$$

$$\tilde{p}_*(x,Y,0) = 0 \text{ for } Y<0 \qquad (5.20b);$$

where $\tilde{p}_{*_{2-D}}(x,Y,0)$ is given in eqn. (3.4).

In the solution process for the present problem, we find that the spanwise Y transform of the loading reduces to the evaluation of the simple integral

$$\int_0^\infty dY\, e^{i\left(\lambda_2 - \frac{k_x \tan\Lambda}{\sqrt{1-M^2}}\right)Y} = \frac{i}{\left(\lambda_2 - \frac{k_x \tan\Lambda}{\sqrt{1-M^2}}\right)} \qquad (5.21),$$

which converges for $\mathrm{Im}(\lambda_2) > \mathrm{Im}(k_x \tan\Lambda \sqrt{1-M^2})$. Multiplied by $(1+i)/2$, this result for the cut-off solution replaces that in (5.16) for the spanwise spectrum of the blade loading with improved side-edge behavior.

The acoustic far field for a semi-infinite span wing with square cut-off of the loading at the side edge is

$$P \sim \frac{\rho_o w_o \; U}{2\pi\sqrt{1-M^2}} \; \frac{M(1-M^2)^{1/4}}{\sqrt{\frac{k_x}{1-M^2} + \mu}} \; \frac{1}{\sqrt{k_x}} \; \frac{e}{r_a}^{\frac{i\omega\left(t-\frac{br_a}{c_o}\right)}{1+M\sin\phi\cos\gamma}} \; \frac{D_{c.o}(r,\phi)}{(1+M+in\phi\cos\;)^2} \qquad (5.22),$$

where the "c.o." subscript in $D_{c.o}(\gamma, \phi)$ denotes "cut off." $D_{c.o}(\gamma, \phi)$ was found to be

$$D_{c.o.}(\gamma,\phi) = \cos\phi \left\{ \frac{1}{\left\{ \frac{M}{\sqrt{1-M^2}} \left(\frac{\sin\phi\cos\gamma + M}{1+M\sin\phi\cos\gamma} \right) + i\sqrt{\tan^2\Lambda - \frac{M^2}{1-M^2}} \right\}^{1/2} + \right.$$

$$\frac{i\sqrt{2}\left\{\tan^2\Lambda - \frac{M^2}{1-M^2}\right\}^{1/4}}{\left\{\tan^2\Lambda - \frac{M^2}{1-M^2} + \left[\frac{M}{\sqrt{1-M^2}}\left(\frac{\sin\phi\cos\gamma + M}{1+M\sin\phi\cos\gamma}\right)\right]\right\}^{1/2}} \left[1-(1+i)\right.$$

$$\left. E^*\left[\frac{2k_x}{\sqrt{1-M^2}}\left\{-i\sqrt{\tan^2 - \frac{M^2}{1-M^2}} - \frac{M}{\sqrt{1-M^2}}\left(\frac{\sin\phi\cos\gamma + M}{1+M\sin\phi\cos\gamma}\right)\right\}\right]\right\}$$

$$\frac{1}{\left(\frac{M\sin\phi\sin\gamma}{1+M\sin\phi\cos\gamma} - \tan\Lambda\right)} \qquad (5.23).$$

Predicted directivity patterns for $D_{\sqrt{y}}$ and $D_{c.o.}$

The examples we show next of $D_{\sqrt{y}}$ and $D_{c.o.}$ focus on the acoustic effect of satisfying the side-edge loading condition. We do not, therefore, investigate here again the effect of the trailing edge on radiation (see fig. 3.8), because this is a chordwise effect. Nor do we look for changes due to variations of Mach number - although most compressibility effects cannot be extricated from those of

frequency, we saw in chapter 3 that changes only in the Mach number affect the forward enhancement of the signal; so that we may choose to regard M as really a chordwise, or flight-direction parameter.

Here we investigate the acoustic effect of reduced frequency k_x, which affects the phase and magnitude of the loading near the side; and of Λ, which besides also affecting the side-edge loading, controls the trace speed $U/\tan\Lambda$ of disturbances along the span and the absolute speed $U/\sin\Lambda$ of load fronts through the still fluid for a given M. If we change Λ and keep M constant, we may compare the degree of cancellation of signals radiated by the semi-infinite blade span for the blade with improved side-edge loading, to that for the blade with cut-off loading.

So that we may also compare $D_{\sqrt{y}}(\gamma, \phi)$ to those for the rotating wing of chapter 3, we have plotted the quantity

$$D^*_{\sqrt{y}}(\gamma,\phi) = \frac{\sqrt{M}\sqrt{1-M^2}}{2\sqrt{\pi}\sqrt{k_x}} \sqrt{\tan\Lambda - \frac{M}{\sqrt{1-M^2}}} \; \frac{D_{\sqrt{y}}(\gamma,\phi)}{(1+M\sin\phi\cos\gamma)^2}$$

in figs. 5.3-5.5; and for a similar reason, the quantity $D^*_{c.o.}(\gamma, \phi)$

$$D^*_{c.o.}(\gamma,\phi) = \frac{M(1-M^2)}{2\sqrt{\pi}\sqrt{k_x}} \; D_{c.o.}(\gamma,\phi)$$

in figs. 5.6-5.8. As in chapter 3, every figure shows the

above functions in five planes, each corresponding to a fixed value of the azimuth γ.

From figs. 5.3 and 5.6 for the correct side-edge loaded blade and the blade with cut-off loading, respectively, we note that $D^*_{c.o.}$ is generally greater than $D^*_{\sqrt{y}}$ on the planes shown in parts (a)-(c) of the figures. $D^*_{\sqrt{y}}$ ($\gamma=150°, 0<\phi<\pi/2$) in fig. 5.3e, however, takes on values larger than those for $D^*_{c.o.}$ ($\gamma=150°, 0<\phi<\pi/2$) in fig. 5.6e. This perhaps unexpected peak in $D^*_{\sqrt{y}}(\gamma=150°, \phi=79°)$ can be attributed to a local reinforcement of acoustic signals - recall that the spanwise variation of the phase of tip dipoles is different for the models from which $D^*_{\sqrt{y}}$ and $D^*_{c.o.}$ were calculated.

As we noted earlier, we would expect the differences in the directivity patterns between the two models to increase as Λ increases, because even though the region near the tip where dipole strengths differ substantially is reduced in extent, the differences in spanwise variation of the phase of tip dipoles are then larger. This is in fact the case, as we may see from figs. 5.4 and 5.7: the differences in radiation patterns between cut-off and improved side-edge loadings are greater for $\Lambda=80°$ than for $\Lambda=62°$. Notice also that for both types of loading the overall radiation for $\Lambda=80°$ is substantially reduced. As in chapter 3, we attribute this reduction to the fact that the effective Mach number of load fronts $M/\sin\Lambda$ far from the side edge is lower for $\Lambda=80°$ than for $\Lambda=62°$; so that in both loading cases there is then more cancellation in the acoustic field radiated by the

semi-infinite span of the blade. We conclude that the differences due to changes in $M/\sin\Lambda$ in spanwise loading phase between the correct and cut-off models may cause significant differences in the predicted acoustic fields.

By varying Λ while keeping $\omega b/U$ and M constant, we observed differences between $D^*_{\sqrt{y}}$ and $D^*_{c.o.}$ essentially due to the different way each of the two acoustic models reacted to a change in the absolute Mach number $M/\sin\Lambda$ of load fronts far from the side edge. But the tip-loading expressions derived earlier indicate that a change in K (by changing $\omega b/U$, with $M/\sin\Lambda$ constant), also affects the differences in spanwise variation of tip-loading phase between the two models, and should, therefore, also affect their acoustic fields. Figs. 5.5 and 5.8 show $D^*_{\sqrt{y}}$ and $D^*_{c.o.}$, respectively, for $\omega b/U=10$ while keeping the same M and Λ values of figs. 5.4 and 5.6. They indicate that the differences between $D^*_{\sqrt{y}}$ and $D^*_{c.o.}$ for $\omega b/U=10$ are not much greater than those for $\omega b/U=4$; so that pure frequency effects on spanwise phase differences between the two models have a lesser acoustic effect than does a change in $M/\sin\Lambda$.

Finally, we observe from (5.17) and (5.22) that the acoustic models developed in this chapter share with that of chapter 3 the $1/k_x$ behavior for large k_x. This means that they all predict acoustic signals which are qualitatively similar for small times. We note, however, that for $k_x=0$ (large times) the models developed in this chapter for a wing of semi-infinite span are not well behaved. The physical

reason for the large-time breakdown of the theories is that an infinitely long time is required for pulses radiated near $y=\infty$ to reach the observer, and so, to contribute to the signature which he hears. This issue of convergence in time did not arise in chapter 3 because the blade there was of finite span.

Chapter 6: Summary and Conclusions

We have developed here three basic aeroacoustic models for noncompact blade-gust interaction in subsonic flow. We now briefly summarize our results and draw some conclusions.

Infinite-span airfoil passing through a gust

In chapter 2 we found that frequency and compressibility effects combine into a single parameter which sets the criterion for chordwise noncompactness. We observed that an airfoil responds to an input single-wavelength gust essentially as an aerodynamically diffracting surface - the solution has a continuous wavenumber spectrum. The closed-form expression we have derived for the acoustic field in a laboratory frame indicates that tone radiation patterns from compact, and noncompact airfoil loadings may differ dramatically. The complicated lobing present in the noncompact case is caused by the reinforcement and cancellation of signals from a chordwise distribution of dipoles with large differences in phase. The unsteady loading for an airfoil which is acoustically compact may be represented by a simple dipole, which in turn radiates a simple dipole acoustic field.

We verified the expected lack of acoustic field for interaction angle-Mach number combinations which give load fronts a propagation speed less than that of sound.

Rotating blade of finite span passing through a gust

In chapter 3 we used chapter 2's two-dimensional solution in a superposition scheme to model radiation from a rotating blade of finite span. We found that the acoustic field could be calculated only for cases with subsonic disturbances; the impossibility of extending the analysis to include supersonic trace speeds is an artifact of the solution procedure, which is based on Landahl's[10] edge independence concept. We studied Mach number, frequency, and interaction-angle effects on the radiation pattern of a single tone. The results were presented on the ground, or in the acoustic frame of reference. We refer the reader to the discussion at the end of that chapter for detailed conclusions. We found that for a given set of physical parameters describing the wing-gust interaction, ie. M, Λ, and gust amplitude w_o, the noncompact theory predicts that the tone amplitude at every field point decays algebraically as $1/k_x$, where k_x is the reduced frequency. This is in contrast to the high-frequency behavior of the tone amplitude predicted by compact theories (see, e.g. ref. 3); these predict that for given values of M, Λ, w_o at high frequencies the tone amplitude "levels off" asymptotically to a constant value.

We applied the leading-edge part of the theory to predict the transient signal emmitted by a finite-span blade passing over a potential vortex. We found that the level of

the signature was a sensitive function of spatial position. We attributed this sensitivity of the total signal to cancellation and reinforcement effects of the tones making it up - another consequence of having a noncompact loading.

Semi-infinite rectangular blade with improved side-edge loading

Although we realized in chapter 3 that the model developed there overestimated the strength of dipoles near the blade tip, we had no way of knowing how badly we were modelling the spanwise variation of the loading phase. In chapter 4 we calculate an approximate solution for the three-dimensional pressure field surrounding a corner plate passing through a gust. We find that for large interaction angles the spanwise component of tip-loading phase is nearly constant. The actual variation of the tip-loading phase implies a different pattern of reinforcement and cancellation for signals in the far field.

In chapter 5 we simplify further the aerodynamic result of chapter 4; we then use the new result to calculate the acoustic field for a semi-infinite span rectangular blade, with improved side-edge loading, passing through a gust. We also calculate the acoustic field for a similar blade, but with loading given by the two-dimensional response of chapter 2 abruptly cut off at the tip. This cut off loading is analogous to that used in chapter 3 for a finite blade in that the spanwise loading contains only the spanwise wavenumber of the input gust. We find that the directivity

patterns differ mostly when Λ , the interaction angle, is large. The difference can be explained by noting that the two models then differ greatly in the way they predict the phase of tip dipoles.

We observed that the three-dimensional models developed in chapter 5 share with that of chapter 3 the $1/k_x$ decay of the tone amplitude as a function of high-reduced frequency. As discussed above in chapter 3's summary, this algebraic falloff indicates a fundamental difference in the way radiation patterns are predicted by noncompact and compact models; for given values of M, Λ, and w_o the latter predict that at high-reduced frequencies the amplitude of a tone reaches a constant value.

Conclusions

The signal from a blade which radiates as a noncompact acoustic source probably has a maximum peak value which is smaller than that for a similar signal from a blade which radiates as a compact source. This conclusion is based on comparison of the high-frequency behavior of the amplitude of tones which make up the acoustic signal as predicted by compact theories developed elsewhere[4] with that predicted by the noncompact theories developed here. Unfortunately, because the predicted signals in ref. 4 were calculated for supersonic trace speeds only, direct comparison of those results to those computed here is not possible.

As noted above in the summaries of chapter 3 and 5, for

given values of M, Λ, w_o, we expect a rapid decrease of the level of high-frequency components for a noncompact situation. For given values of M, Λ, w_o, compact theories predict a spectrum which reaches a constant value at high-reduced frequencies, thus suggesting that tone reinforcement could result in a louder signal.

REFERENCES

1. George, A.R., "Helicopter Noise - State of the Art," AIAA Paper 77-1337, Oct. 1977.

2. Boxwell, D.A., Schmitz, F.H., and Hanks, M.L., "In-Flight Far-Field Measurement of Helicopter Impulsive Noise," Presented at the First European Rotorcraft and Powered Lift Aircraft Forum, Sept. 22-24, 1975.

3. Widnall, S.E., "Helicopter Noise due to Blade-Vortex Interaction," The Journal of the Acoustical Society of America, Vol. 50, No. 1, 1971, Pt. 2.

4. Widnall, S.E. and Wolf, T., "Effect of Tip-Vortex Structure on Helicopter Noise due to Blade-Vortex Interaction," Journal of Aircraft, Vol. 17, Oct. 1980, pp. 705-711.

5. Kaji, S., "Noncompact Source Effects on the Prediction of Tone Noise from a Fan Rotor," AIAA Paper 75-446, 2nd Aeroacoustics Conference, March 24-26, 1975.

6. Ahmadi, A.R., "An Asymptotic Unsteady Lifting-Line Theory with Energetics and Optimum Motion of Thrust-Producing Surfaces," MIT Fluid Dynamics Research Laboratory, Rept. 80-2, Sept. 1980.

7. Chu, S. and Widnall, S.E., "Prediction of Unsteady Airloads for Oblique Blade-Gust Interaction in Compressible Flow, AIAA Journal, Vol. 12, Sept. 1974, pp. 1228-1235.

8. Chu, S. and Widnall, S.E., "Lifting-Surface Theory for a Semi-Infinite Wing in Oblique Gust," AIAA Journal, Vol. 12, Dec. 1974, pp. 1672-1678.

9. Martinez, R. and Widnall, S.E., "Unified Aerodynamic-Acoustic Theory for a Thin Rectangular Wing encountering a Gust," AIAA Journal, Vol. 18, June 1980, pp. 636-645.

10. Landahl, M.T., Unsteady Transonic Flow, Pergamon Press, N.Y., 1961, pp. 28-29.

11. Landahl, M.T., "Theoretical Studies of Unsteady Transonic Flow-IV. The Oscillating Rectangular Wing with Control Surface," Aeronautical Research Institute of Sweden (FFA), Rept. 80, 1958.

12. Adamczyk, J.J. and Brand, R.S., "Scattering of Sound by an Aerofoil of Finite Span in a Compressible Stream," Journal of Sound and Vibration, Vol. 25, No. 1, Nov. 1972, pp. 139-156.

13. Adamczyk, J.J., "The Passage of an Infinite-Swept Airfoil through an Oblique Gust," NASA CR-2395, May 1974.

14. Paterson, R.W. and Amiet, R.K., "Acoustic Radiation and Surface Pressure Characteristics of an Airfoil due to Incident Turbulence," AIAA Paper 76-571, 3rd Aeroacoustic Conference, July 20-23, 1976.

15. Amiet, R.K., "Noise Produced by Turbulent Flow into a Propeller or Helicopter Rotor," AIAA Journal, Vol. 15, March 1977, pp. 307-308.

16. Amiet, R.K., "High-Frequency Thin Airfoil Theory for Subsonic Flow," AIAA Journal, Vol. 14, Aug. 1976, pp. 1076-1082.

17. Lima, L., "A Compressible, High-Frequency Numerical Model of Helicopter Noise due to Blade-Vortex Interaction," Masters Thesis with S.E. Widnall, June 1980.

18. Betz, A., NACA Tech. Memo. 713, 1932.

19. Miles, J.W., "The Oscillating Rectangular Airfoil at Supersonic Speeds," Quart. J. App. Math., Vol. 9, 1951, pp. 47-65.

20. Carrier, G.F., "Analytic Approximation Techniques in Applied Mathematics," S.I.A.M., Vol. 13, March 1965, pp.91-95.

21. Goldstein, M.E., Aeroacoustics, McGraw-Hill, N.Y., 1976, p. 122, second term of equation below (3.23).

22. Carrier, Krook, and Pearson, Functions of a Complex Variable, Theory and Technique, McGraw-Hill, N.Y., 1966, pp.382-383.

23. Noble, B., Methods based on the Wiener-Hopf Technique, International Series of Monographs on Pure and Applied Mathematics, Pergamon Press, N.Y., 1958, pp. 34-35.

24. Graham, J.M.R., "Similarity Rules for Thin Aerofoils in Nonstationary Flows," Journal of Fluid Mechanics, Vol. 43, Oct. 1970, pp. 753-766.

25. Whitham, G.B., Linear and Nonlinear Waves, Wiley, N.Y., 1974, p. 382.

26. Bender, C.M. and Orszag, S.A., Advanced Mathematical Methods for Scientists and Engineers, McGraw-Hill, N.Y., 1978, pp. 251-252.

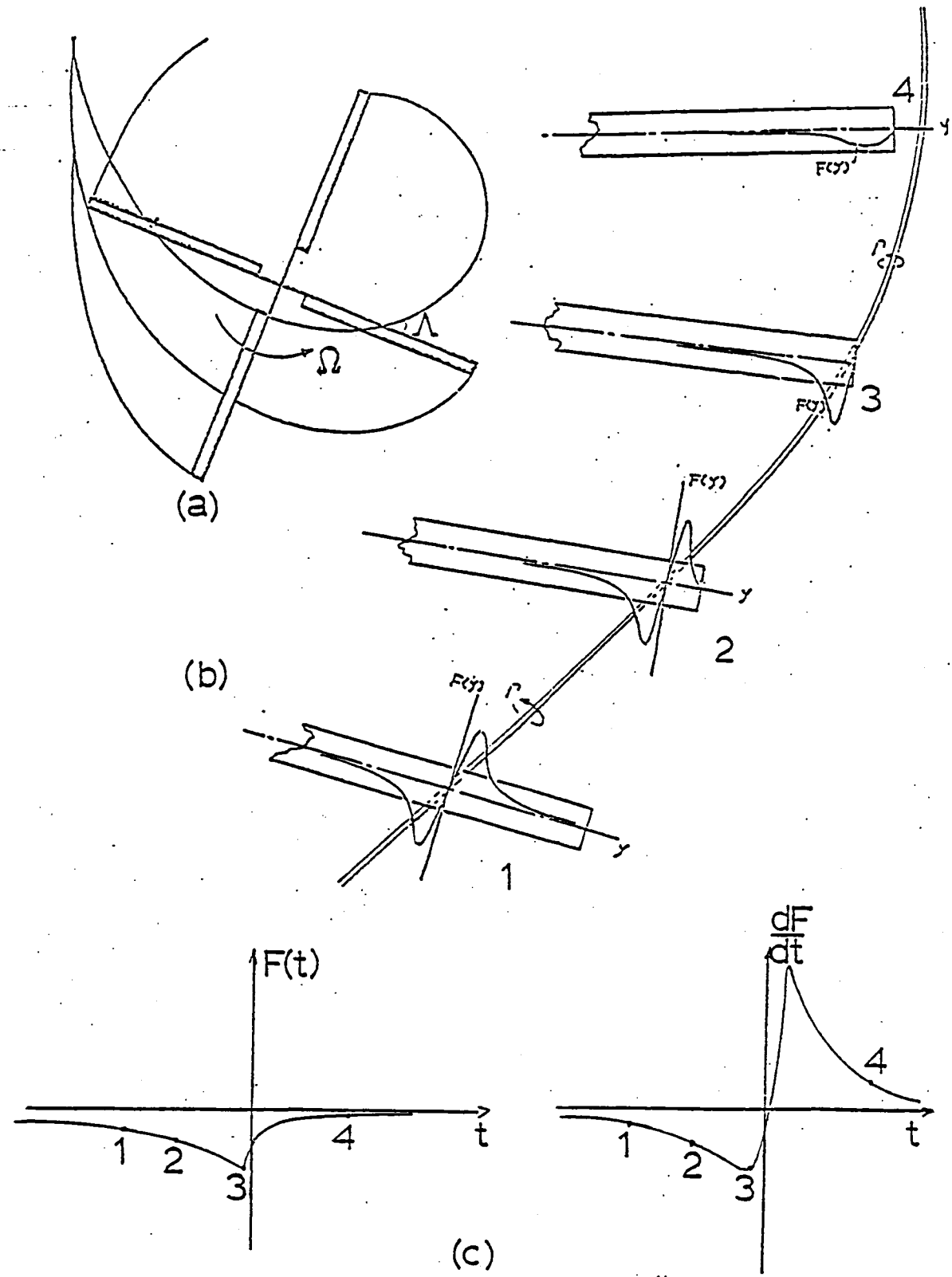

Fig. 1.1 (a) Relative positions of blades and vortices for a single-rotor helicopter; (b) Stages of a blade-vortex interaction; (c) unsteady blade force and its time derivative.

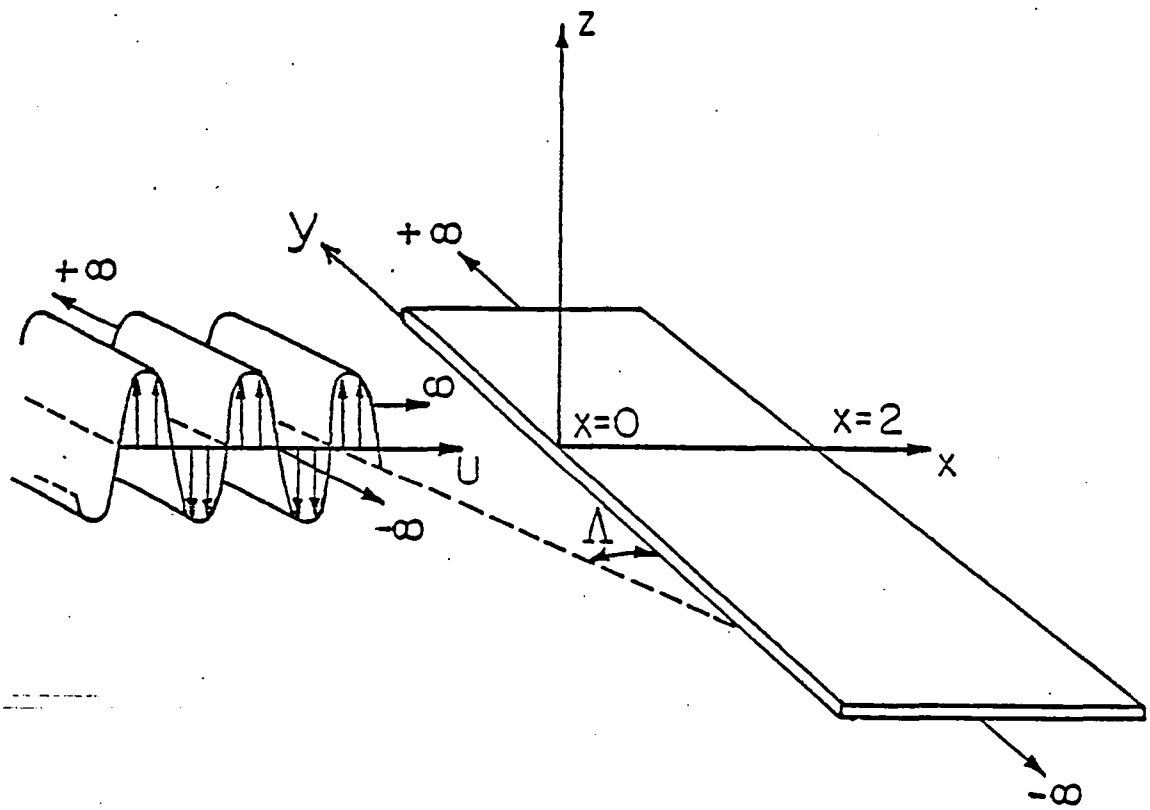

Fig. 2.1 The passage of an infinite-span wing through an oblique gust.

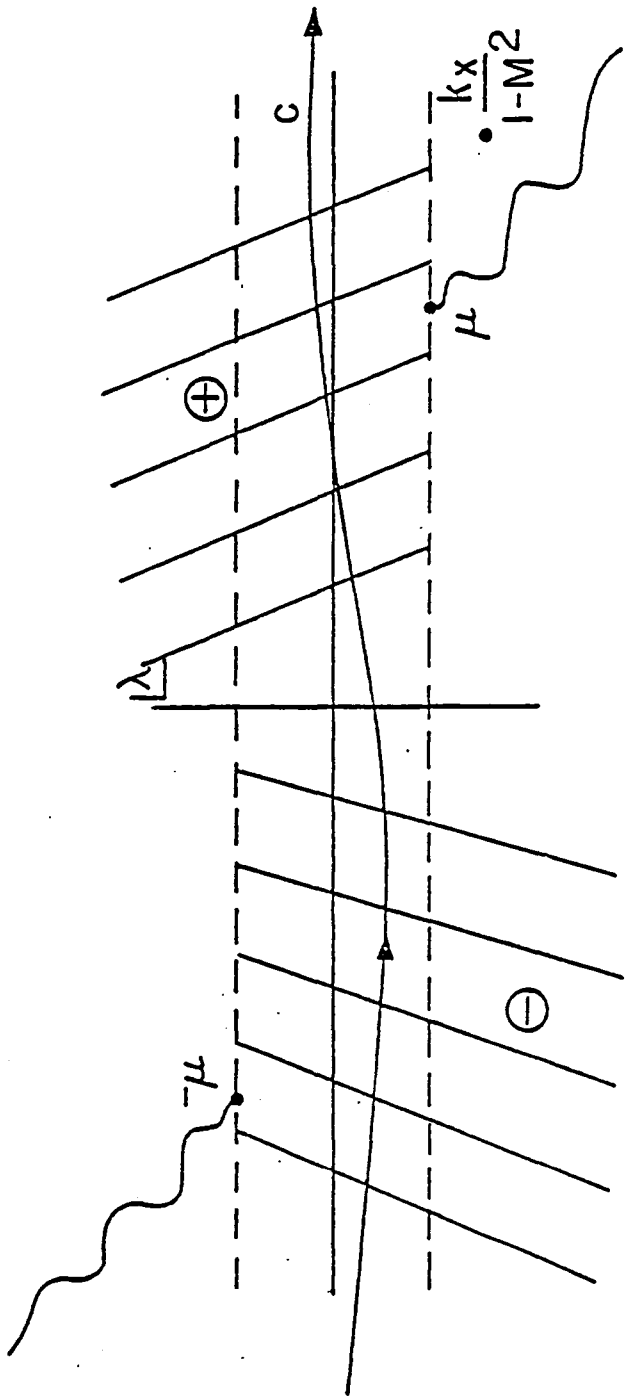

Fig. 2.2 Regions of analyticity ⊖, ⊕ and complex contour C.

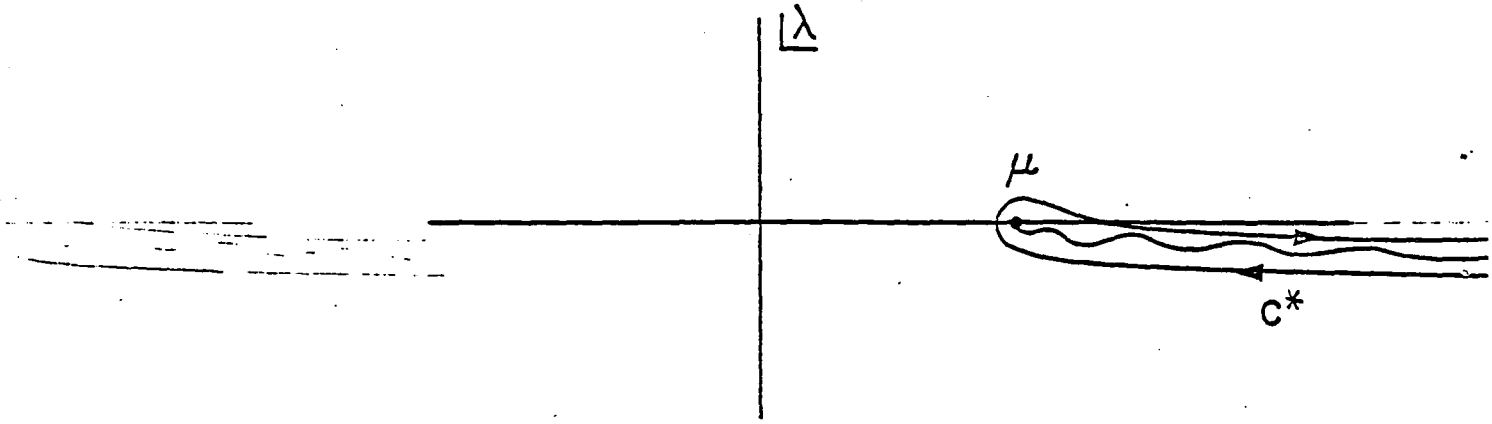

Fig. 2.3 Deformed contour C*, for x>0.

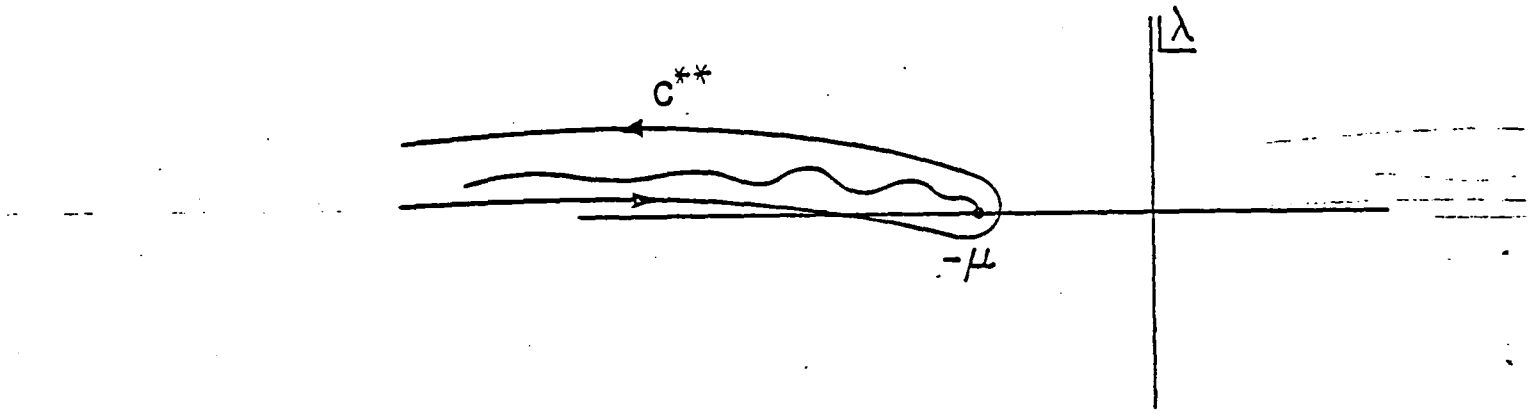

Fig. 2.4 Deformed contour C**, for x<2.

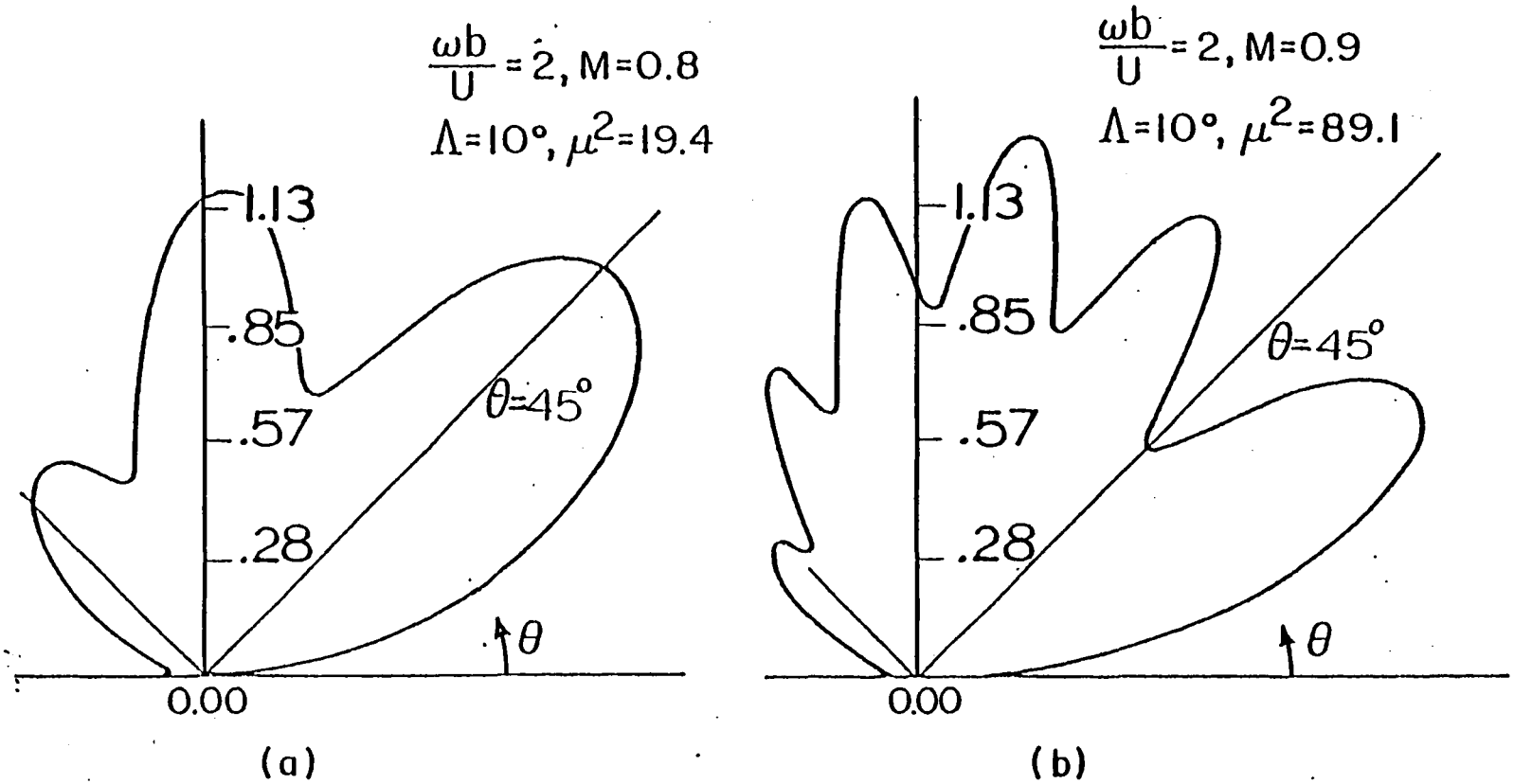

Fig. 2.5 Magnitude of two-dimensional acoustic directivity, $D(\theta)$, in the airfoil frame of reference.

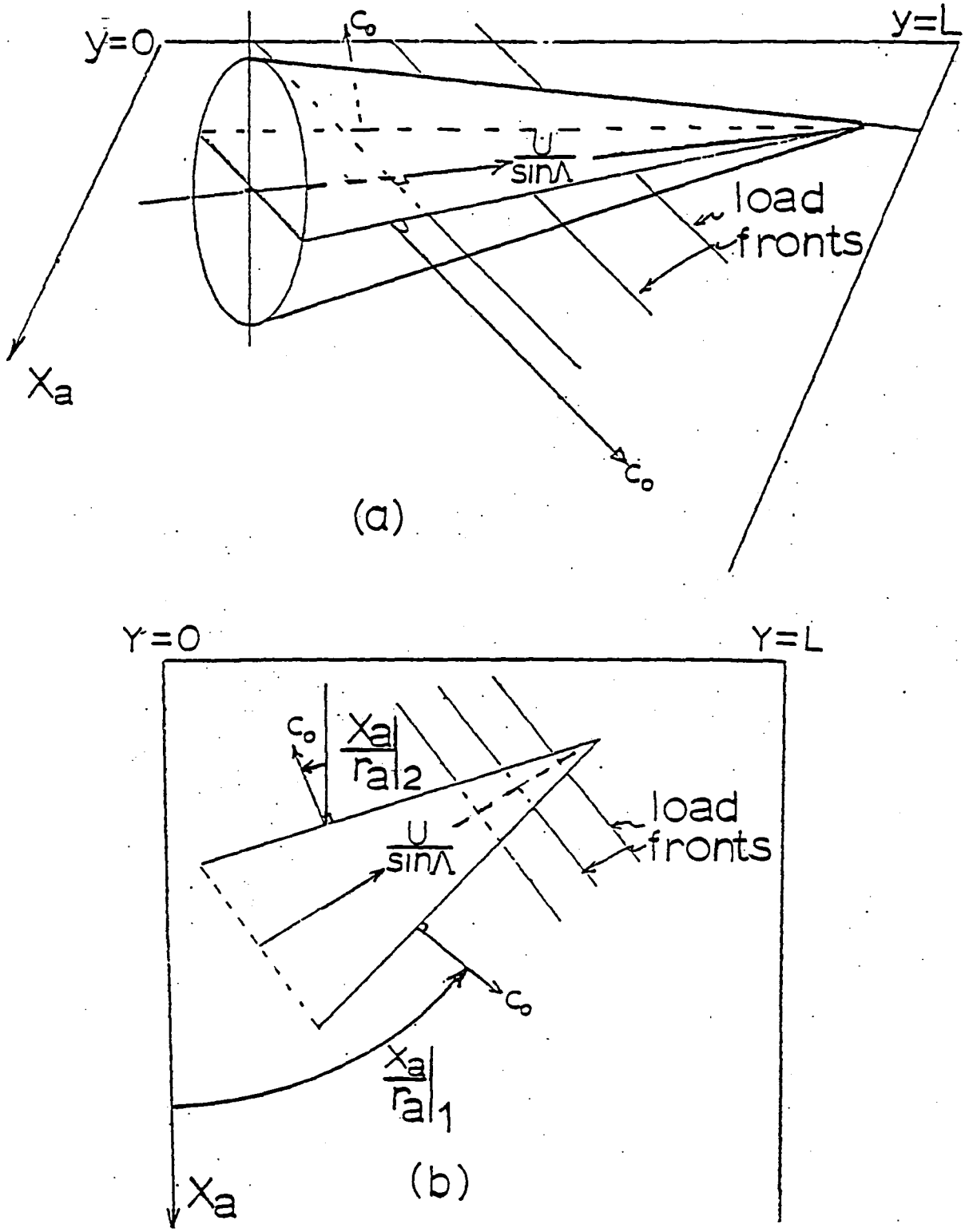

Fig. 3.1a,b Typical acoustic Mach cone for a source travelling supersonically through the still fluid; (b) shows top view and propagation directions given by eqns. (3.15), (3.16).

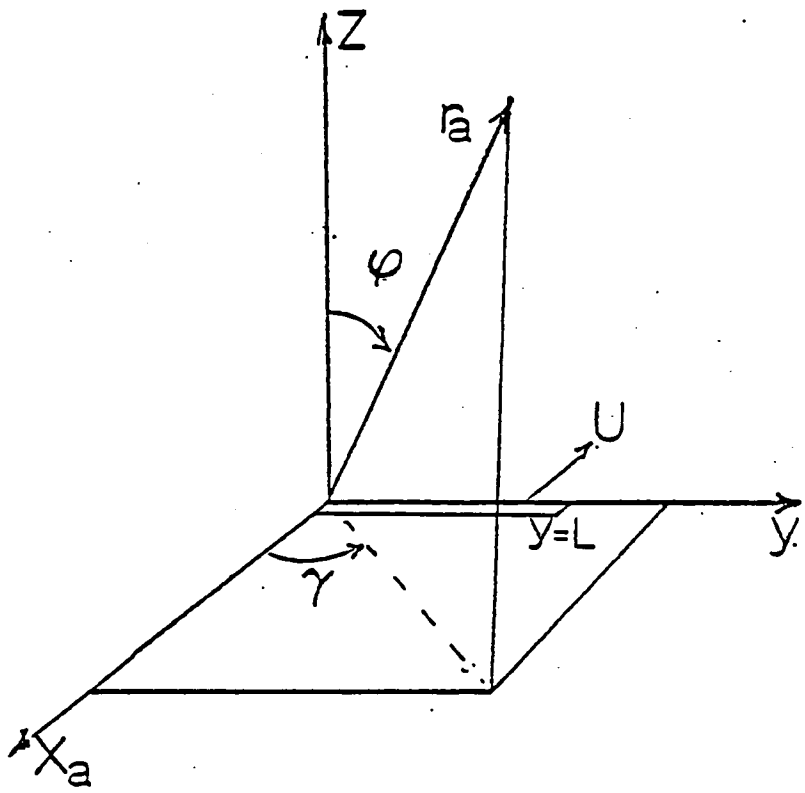

Fig. 3.2 Spherical coordinate system defining the position of a listener in the ground reference frame.

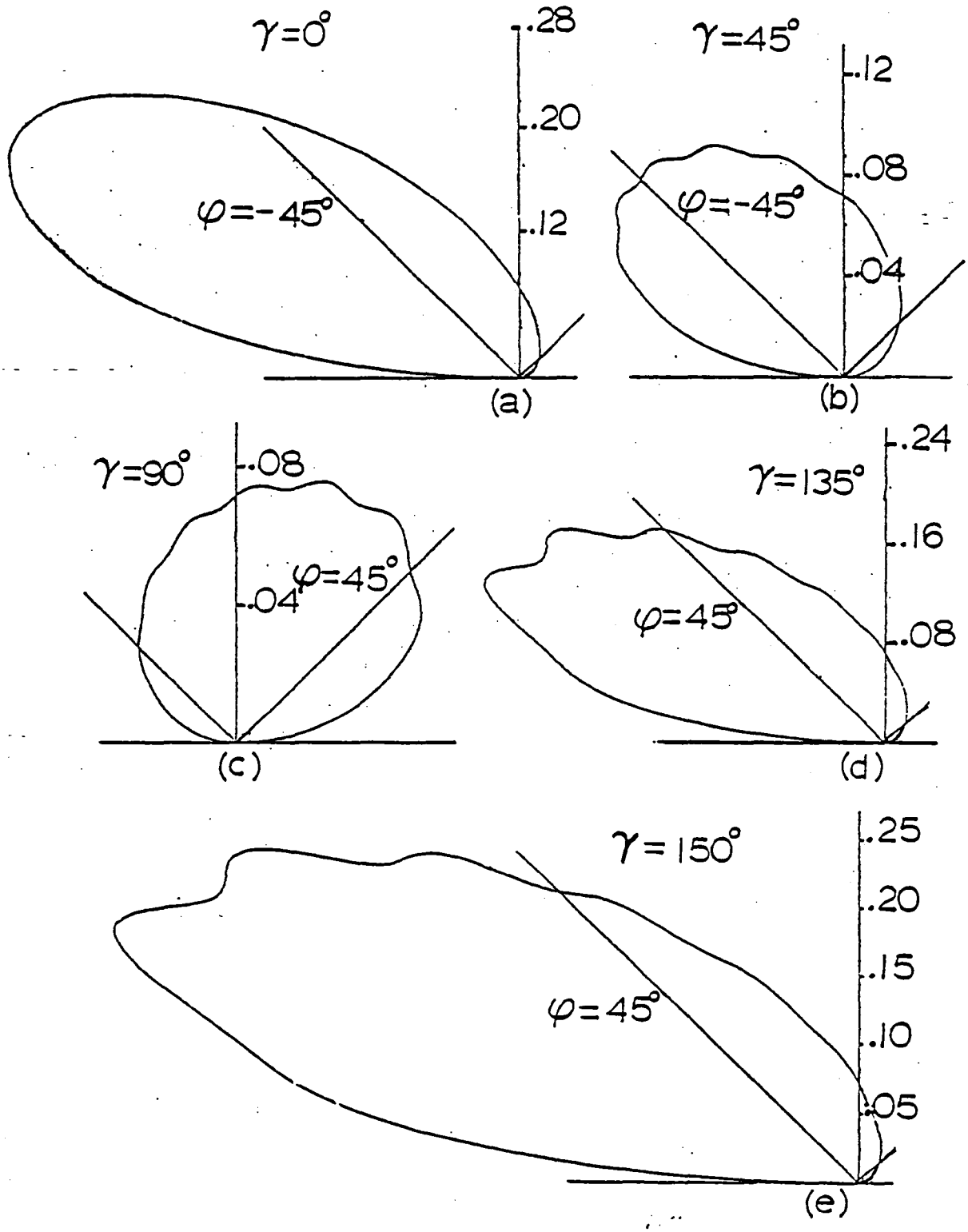

Fig. 3.3a-e Plot of the magnitude of three-dimensional acoustic directivity $D_{3\text{-}D}(\gamma, \phi)$ for $k_x=2$, M=.8, $\Lambda=62°$, L/b=15.

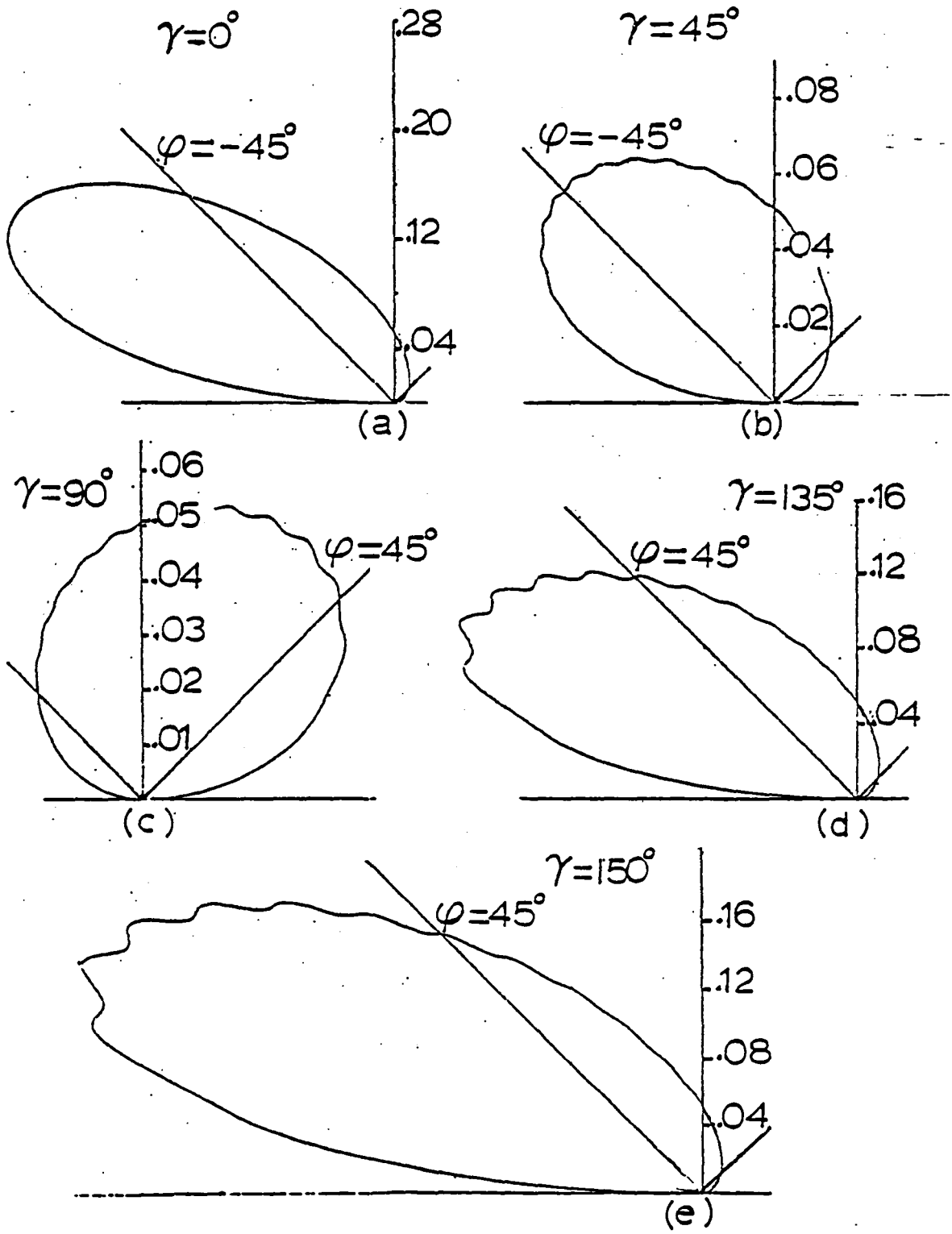

Fig. 3.4a-e Plot of the magnitude of the three-dimensional acoustic directivity $D_{3-D}(\gamma,\phi)$ for $k_x=4$, M=.8, $\Lambda=62°$, L/b=15.

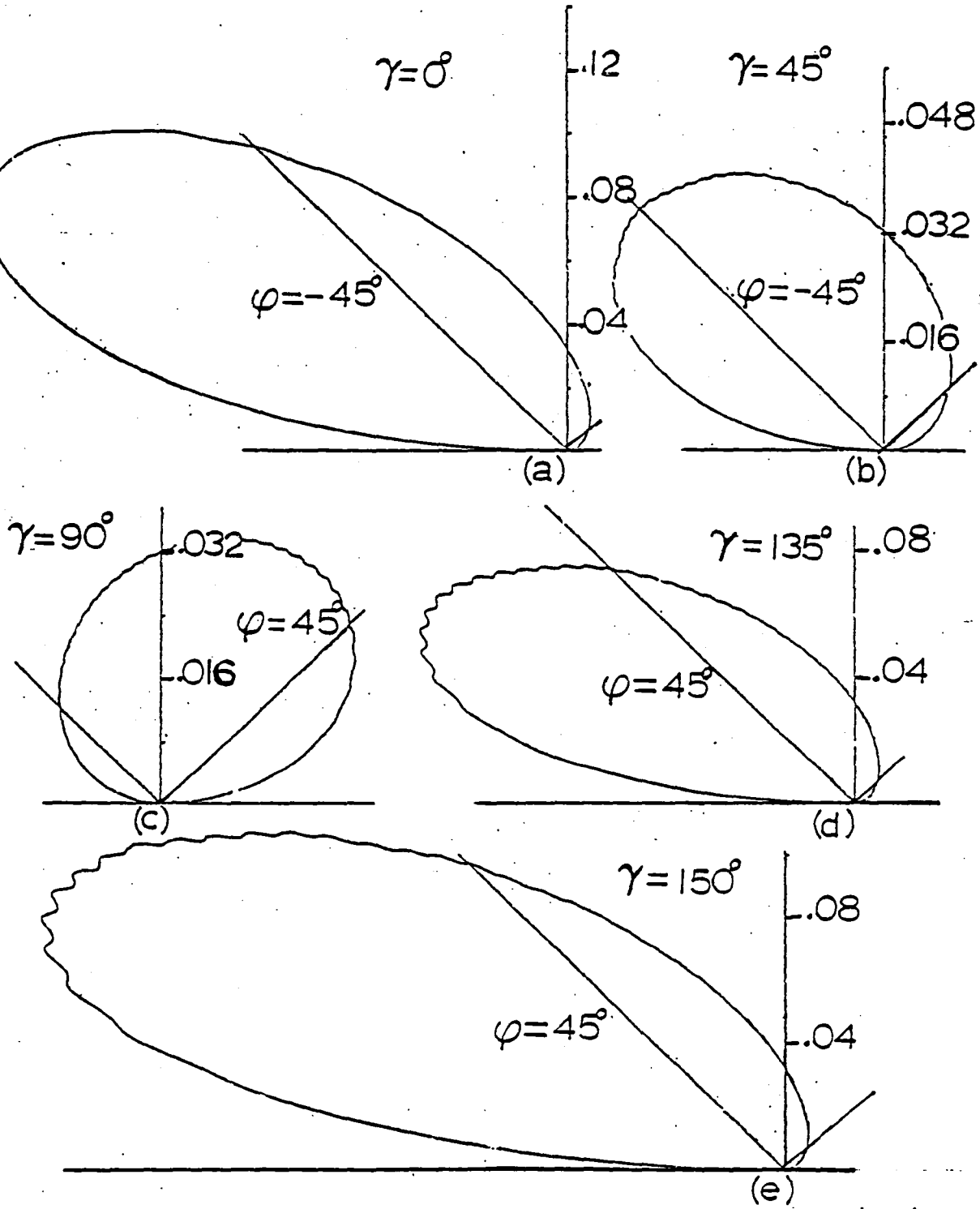

Fig. 3.5a-e Plot of the magnitude of the three-dimensional acoustic directivity $D_{3-D}(\gamma,\phi)$ for $k_x=10$, M=.8, $\Lambda=62°$, L/b=15.

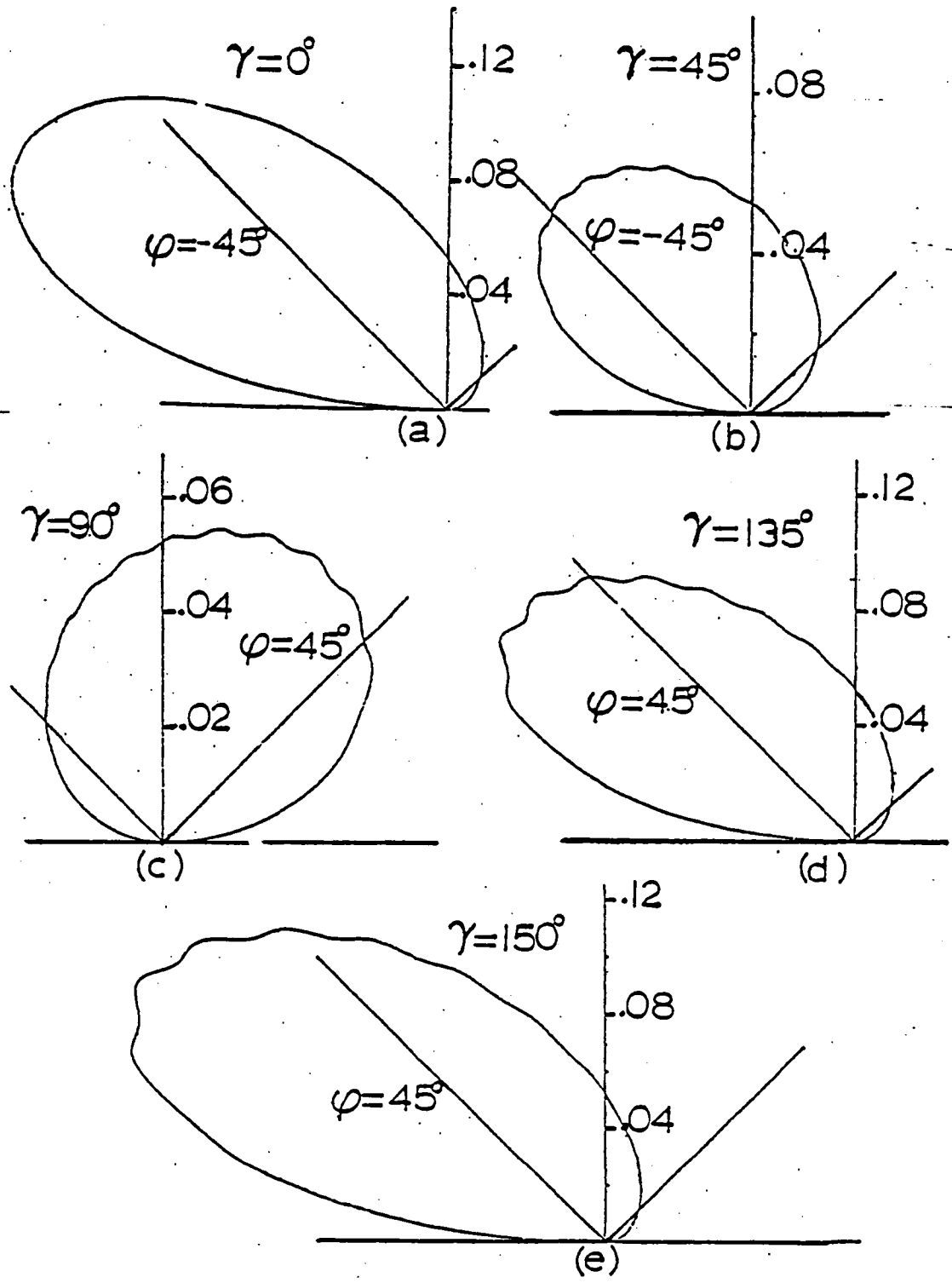

Fig. 3.6a-e Plot of the magnitude of the three-dimensional acoustic directivity $D_{3-D}(\gamma,\phi)$ for $k_x=4$, M=.7, $\Lambda=62°$, L/b=15.

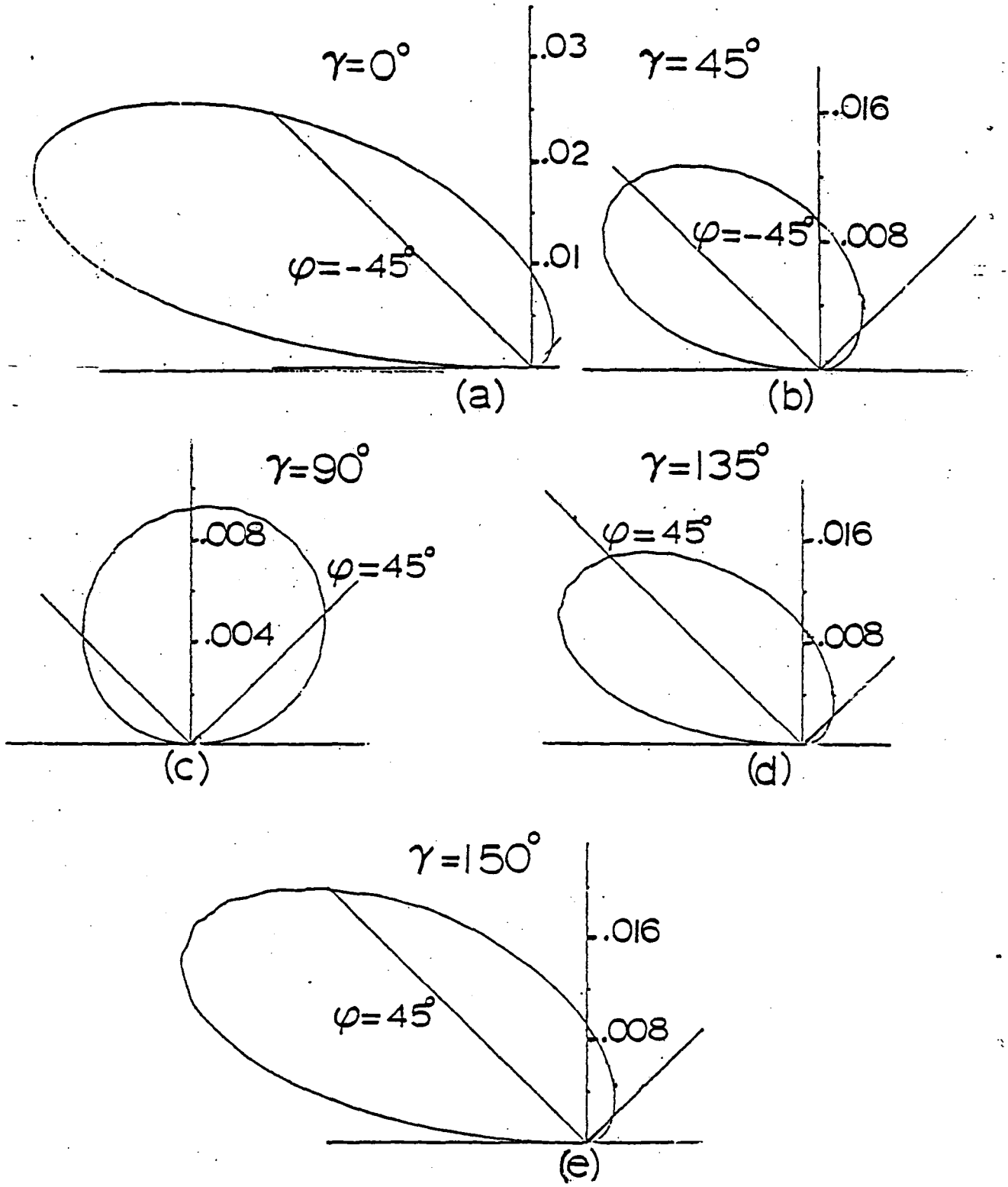

Fig. 3.7a-e Plot of the magnitude of the three-dimensional acoustic directivity $D_{3-D}(\gamma,\phi)$ for $k_x=4$, M=.8, $\Lambda=80°$, L/b=15.

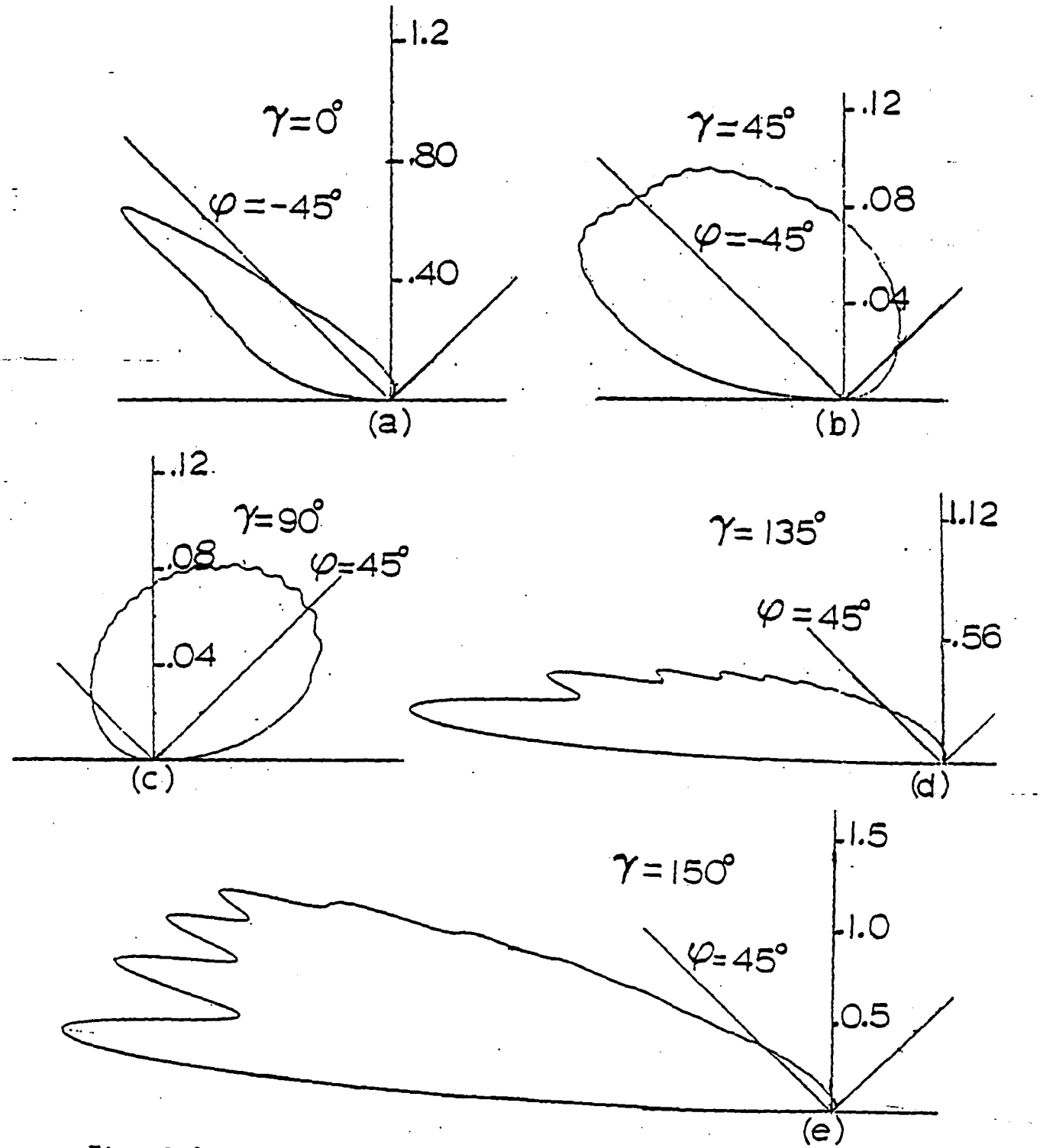

Fig. 3.8a-e Plot of the magnitude of the three-dimensional acoustic directivity $D_{3-D}(\gamma,\phi)$ for $k_x=6$, $M=.8$, $\Lambda=53°$, $L/b=15$.

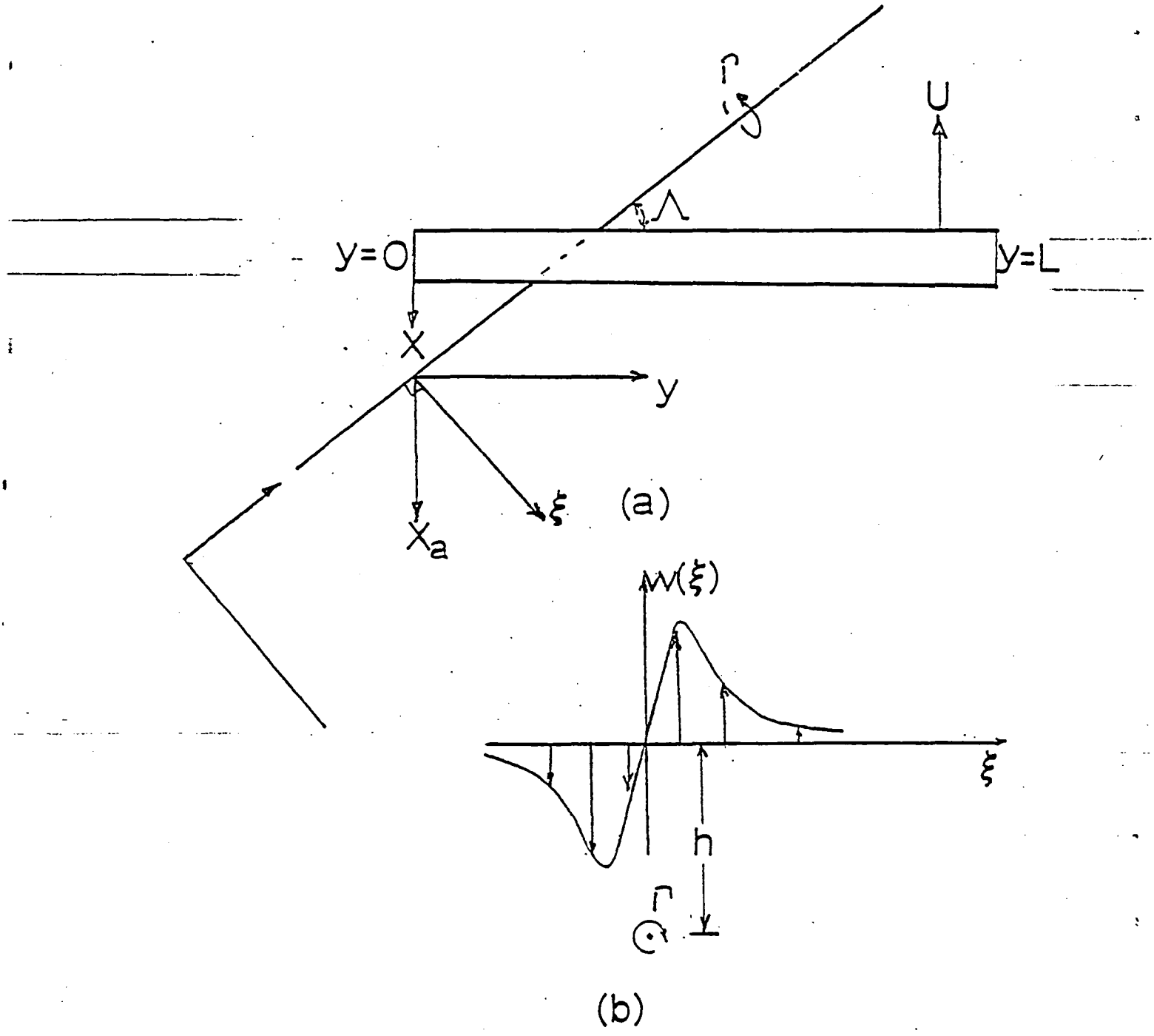

Fig. 3.9a,b Coordinate systems used to model the blade-vortex interaction of fig.1.1a,b.

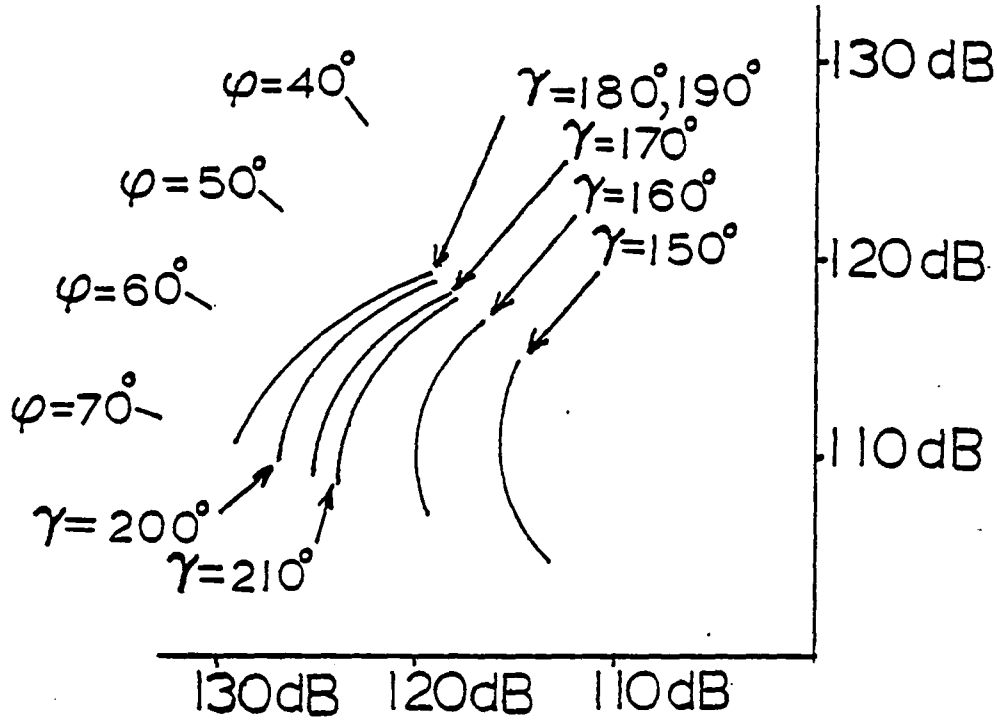

Fig. 3.10 Part of the directivity pattern of the peak signal as predicted by eqn. (3.29).

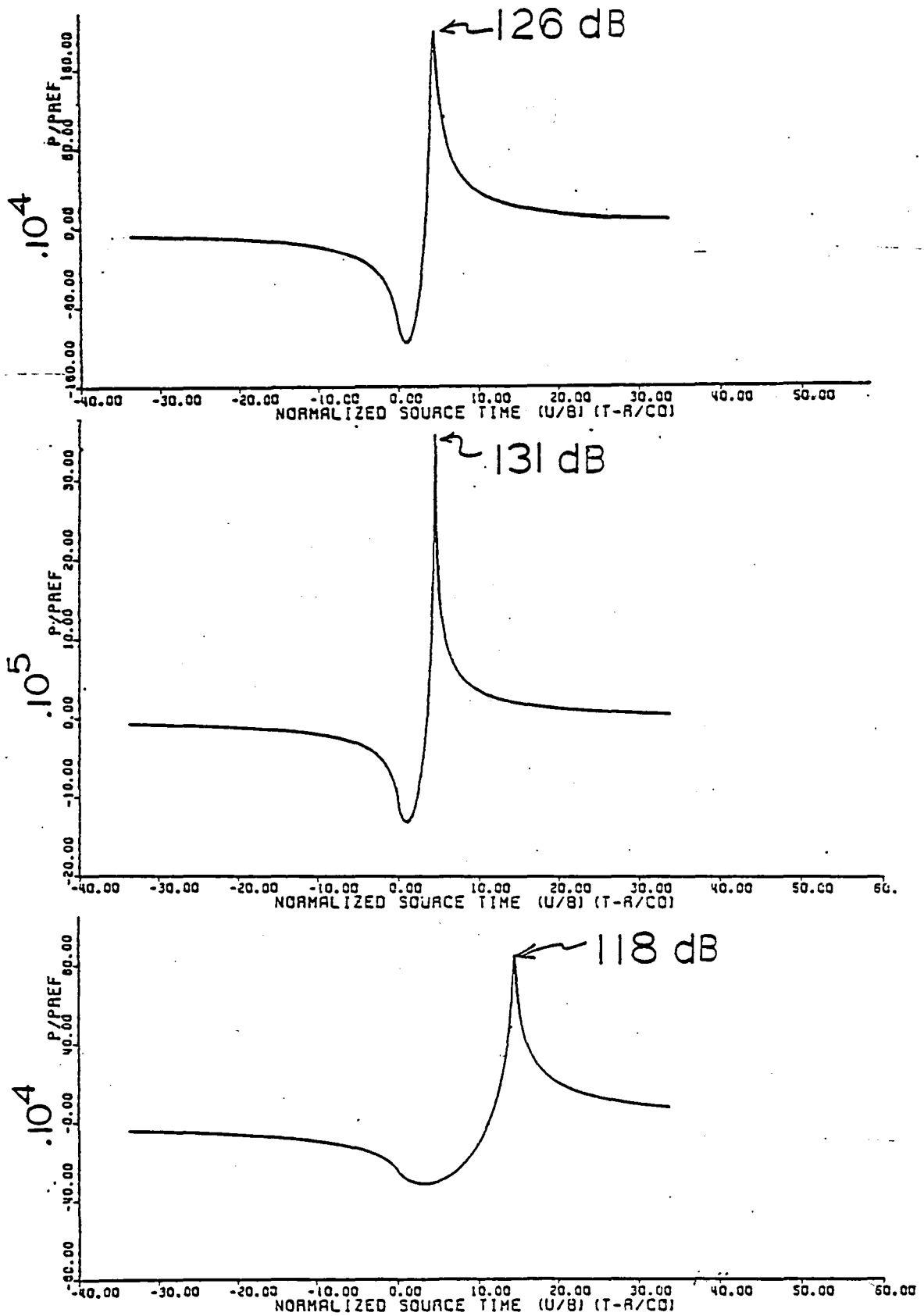

Fig. 3.11a-c Predicted acoustic signatures (from closed-form result (3.29)) for r_a=1000 ft, M=.8, Λ=62°, L/b=15, at (a) γ=180°,ϕ=65° with h/b=.5; (b) γ=180°,ϕ=65° with h/b=.1; (c) γ=180°,ϕ=10° with h/b=.1. Reference pressure is .0002 microbar.

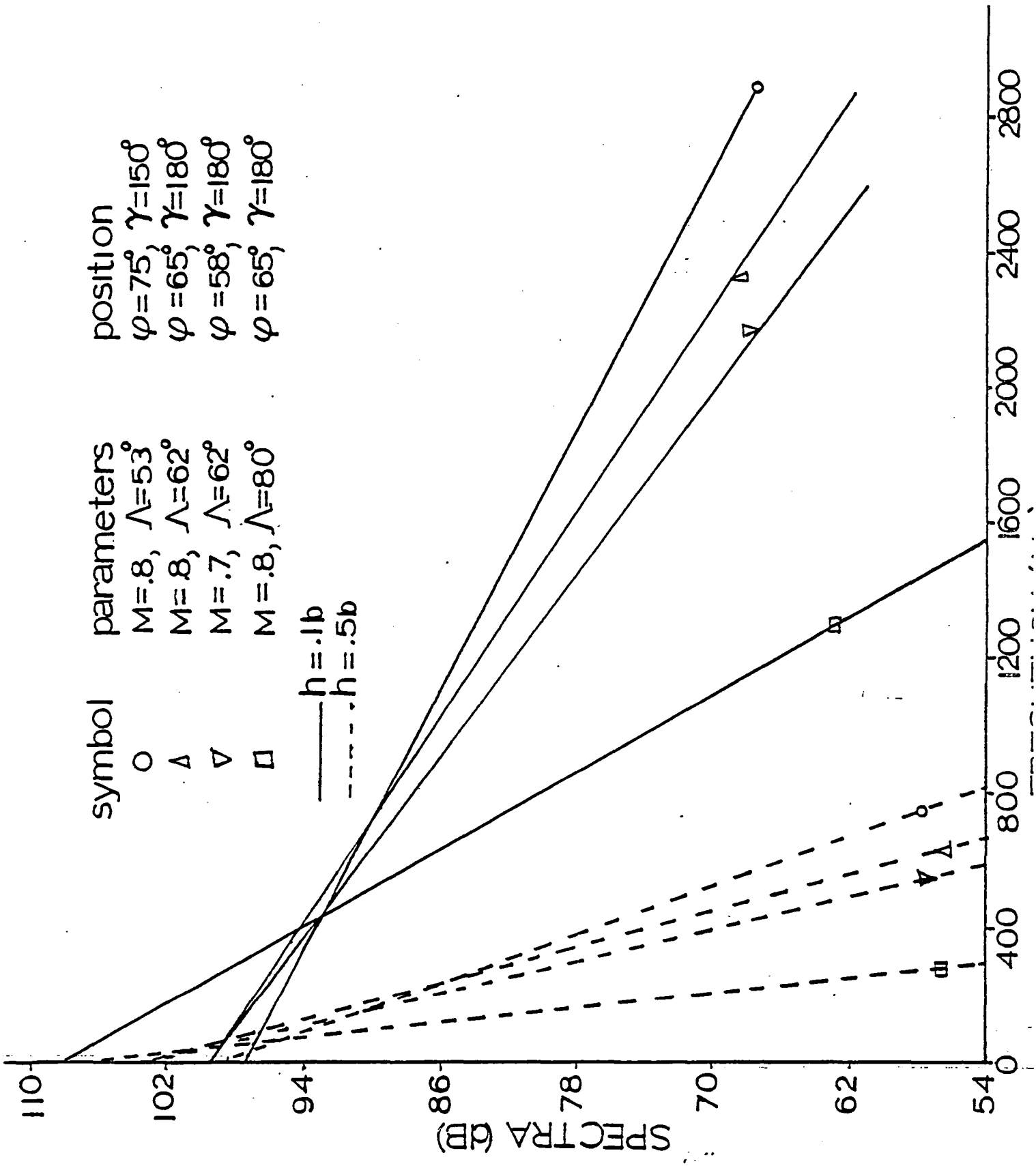

Fig. 3.12 Predicted spectra of signatures at positions indicated for h/b=.5 and h/b=.1.

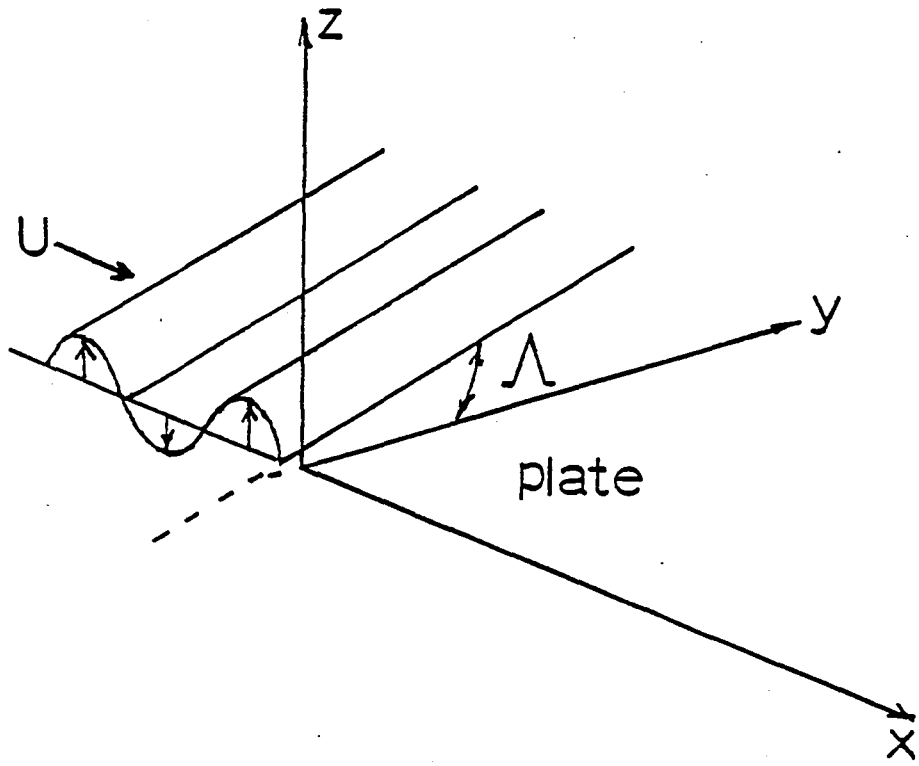

Fig. 4.1 The passage of a quarter-infinite flat-plate wing through an oblique gust.

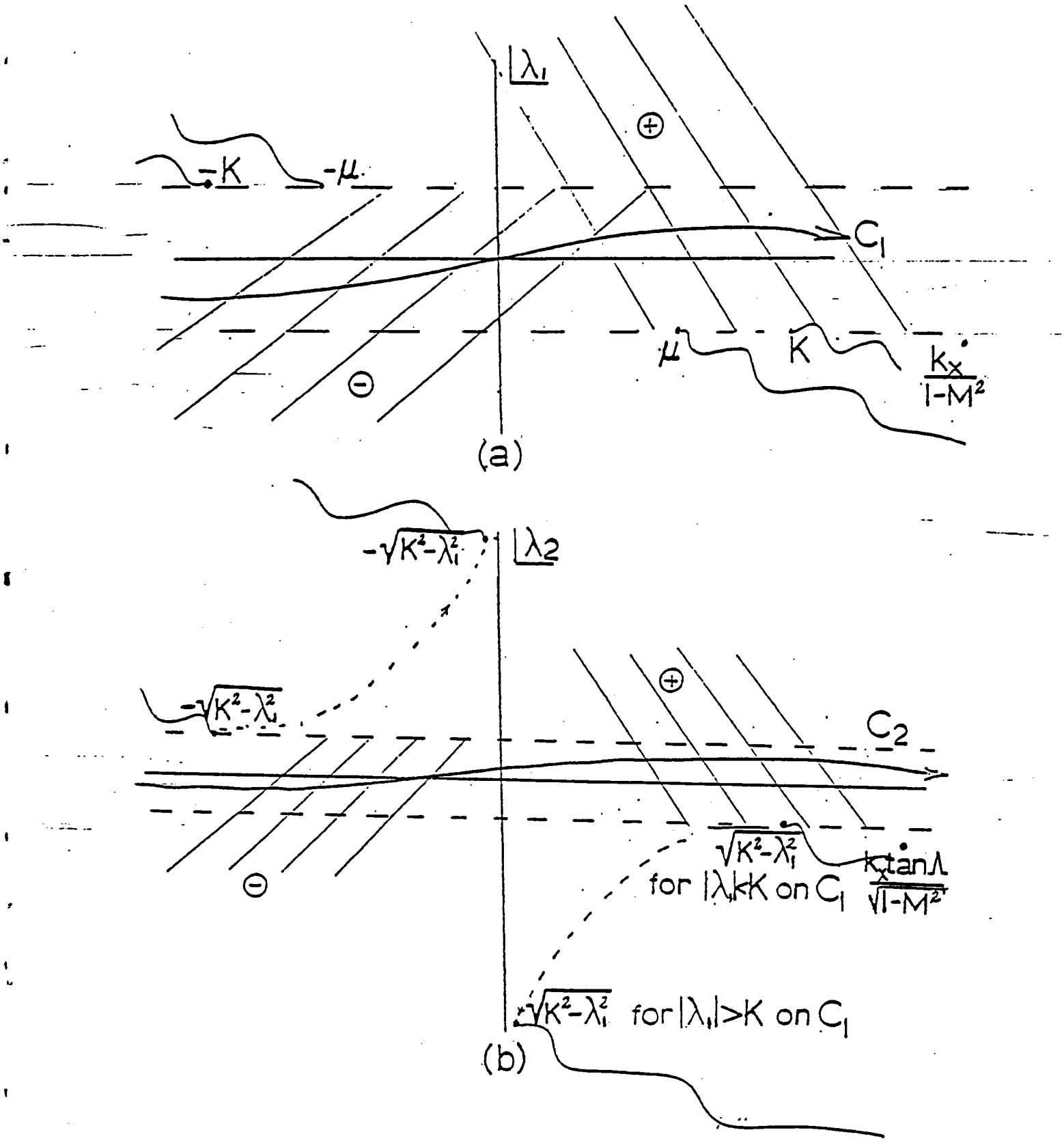

Fig. 4.2a,b Regions of ⊖ and ⊕ analyticity in the complex λ_1, λ_2 planes. Integration contours C_1, C_2 are indicated.

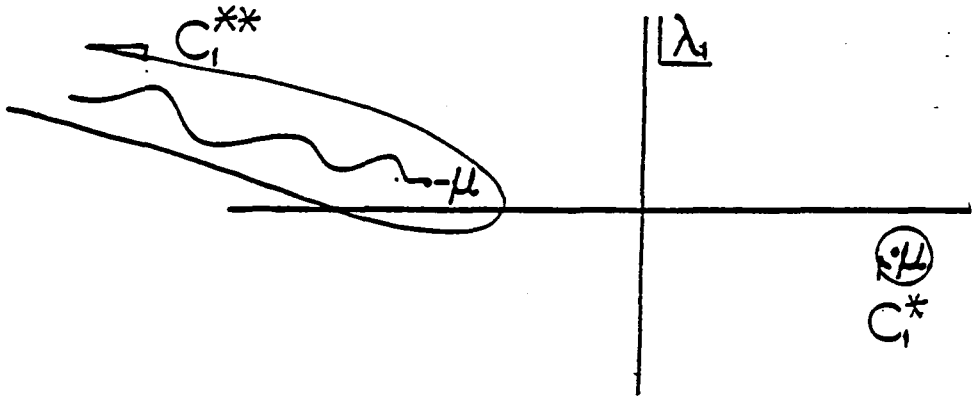

Fig. 4.3 Deformed contours C_1^*, C_1^{**} for $x>0$, $x<0$, respectively.

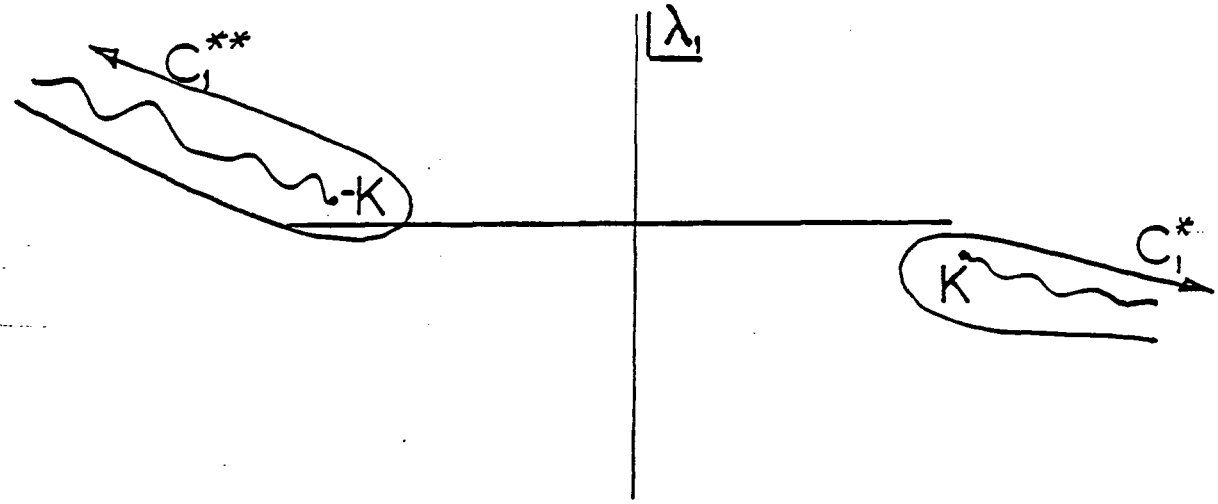

Fig. 4.4 Deformed contours C_1^*, C_1^{**} for $x>0$, $x<0$, respectively.

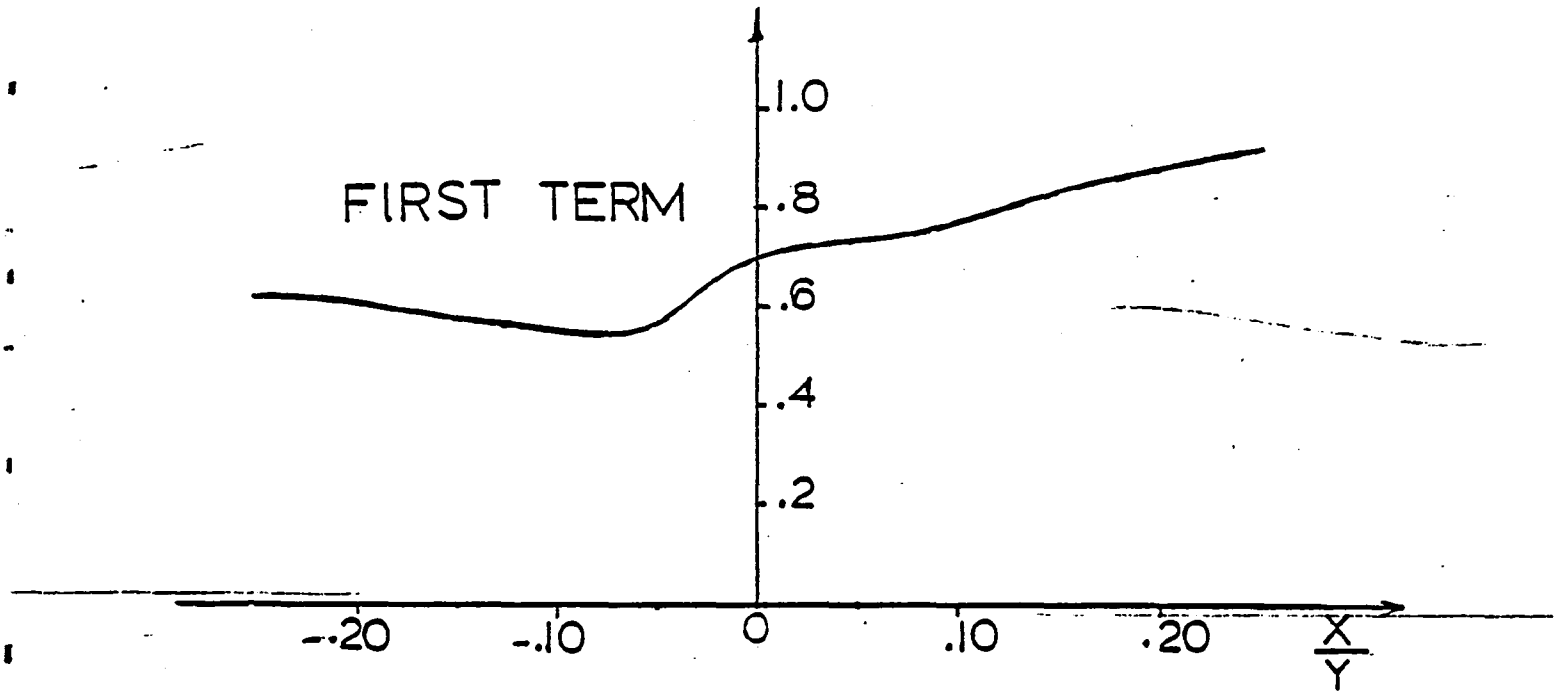

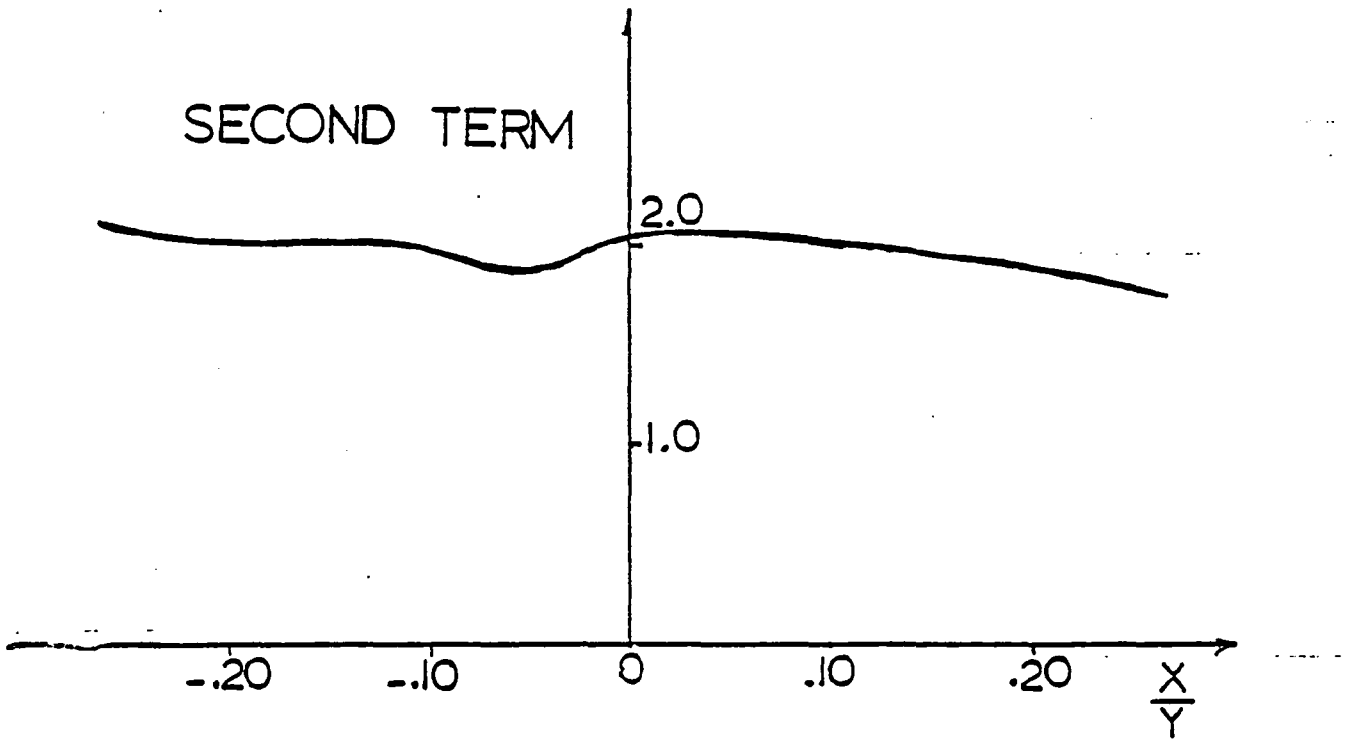

Fig. 4.5a,b Plots of first, and second terms in brackets in eqn. (4.30).

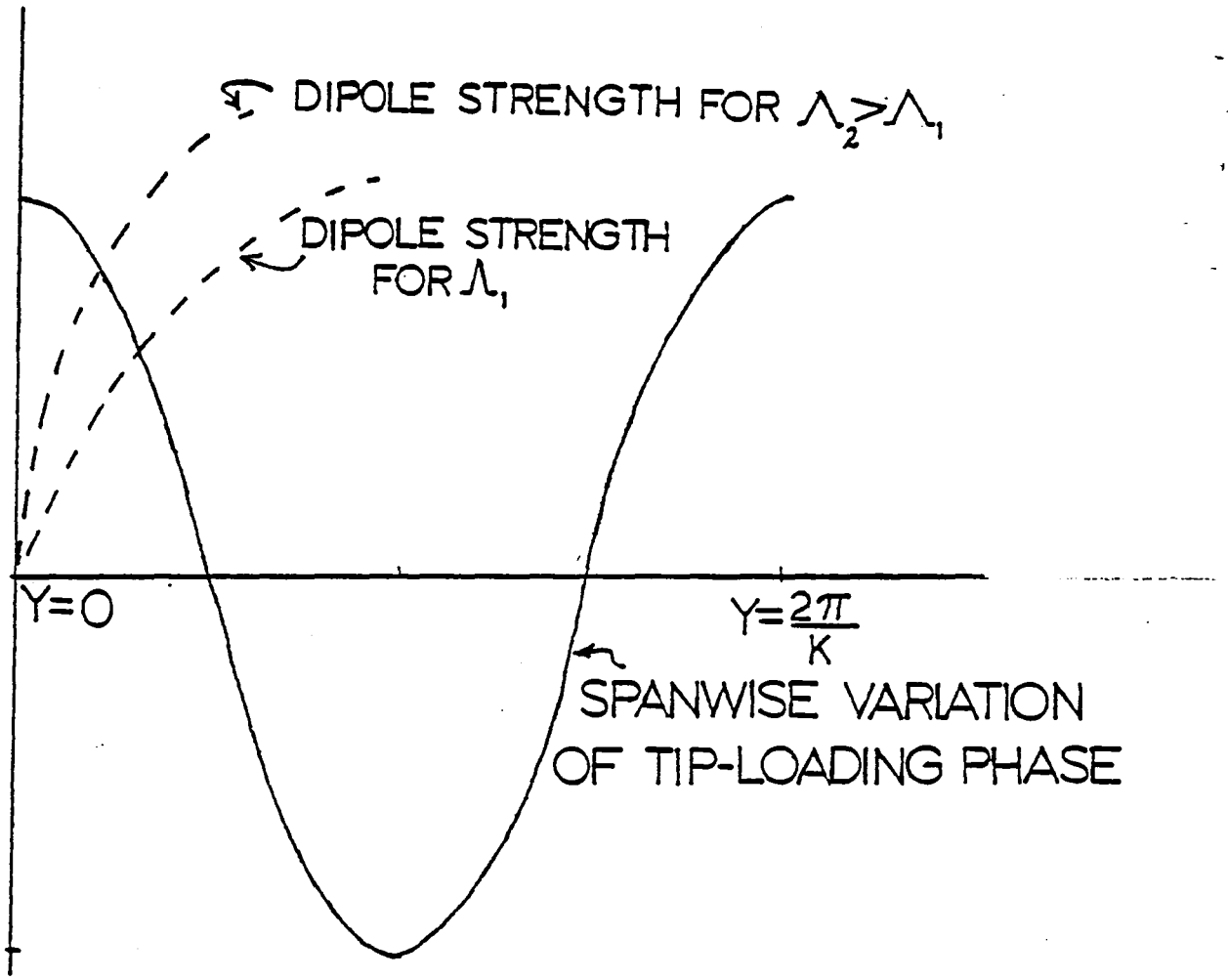

Fig. 5.1a,b Spanwise loading predicted by (5.11a,b): magnitude and phase for $\Lambda_2 > \Lambda_1$. in the ground reference frame.

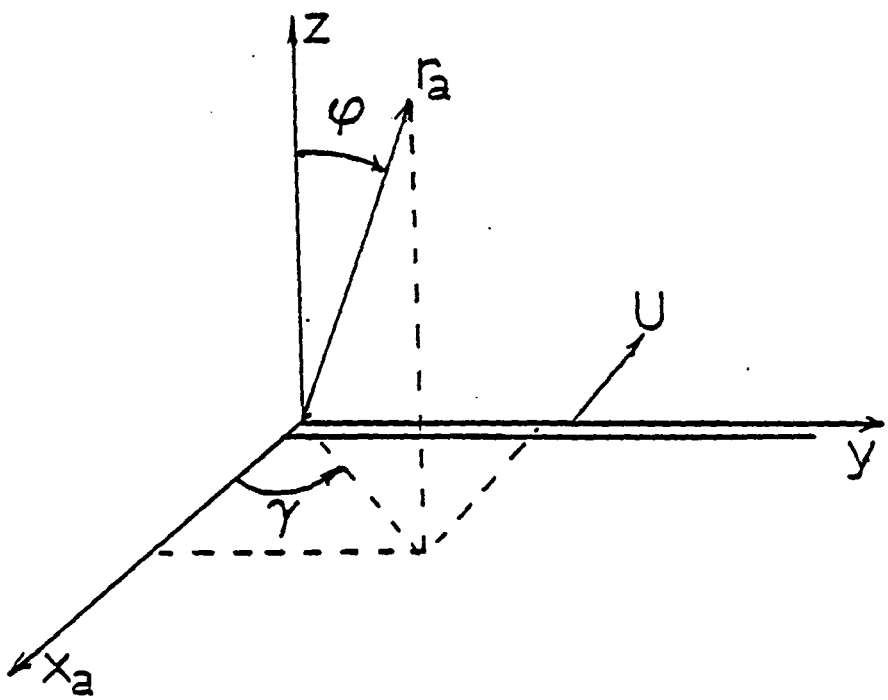

Fig. 5.2 Spherical coordinate system defining the position of a listener in the ground reference frame.

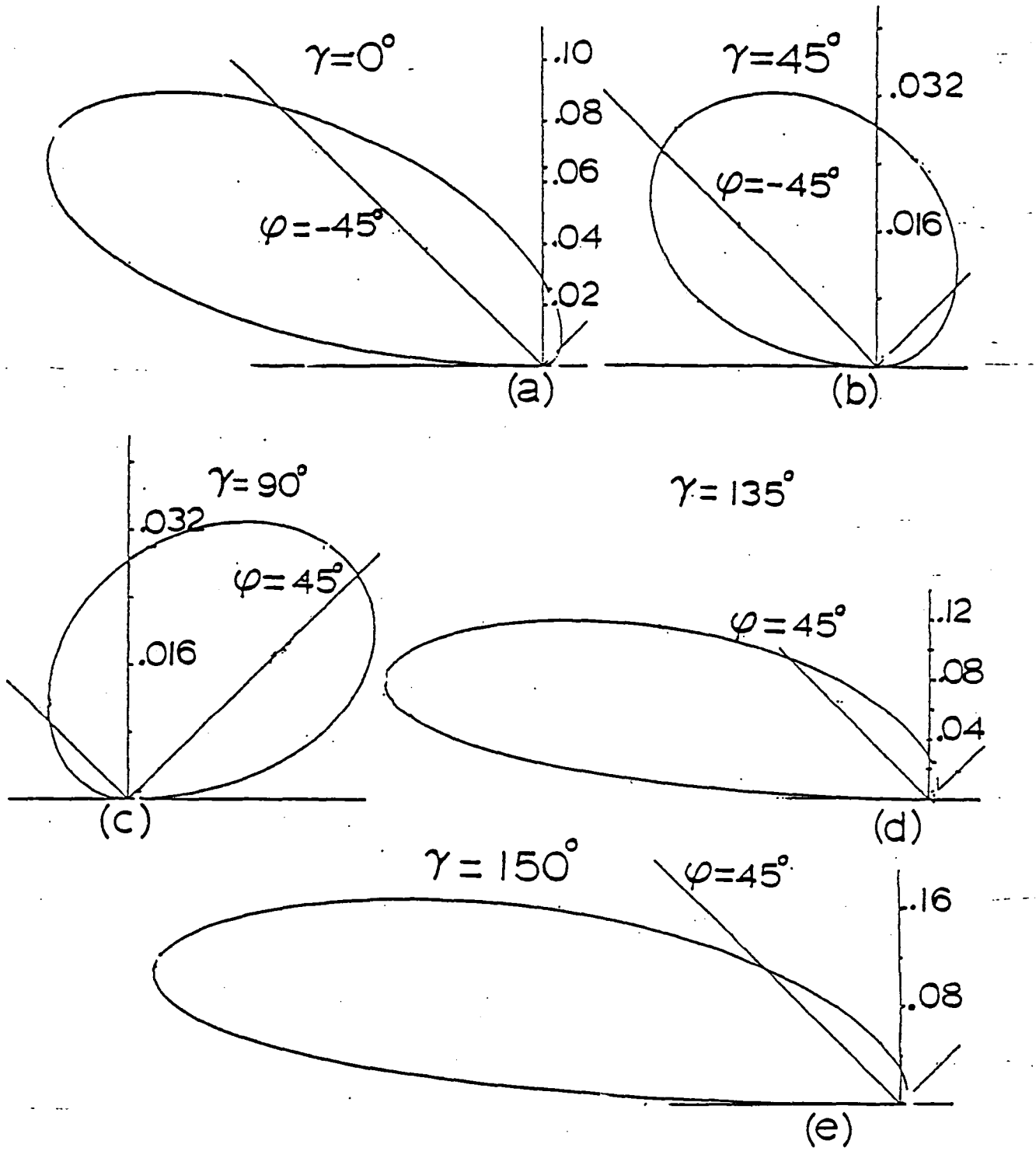

Fig. 5.3a-e Plot of the magnitude of the three-dimensional acoustic directivity $D^*_{\sqrt{y}}(\gamma, \phi)$ for $k_x=4$, $M=.8$, $\Lambda=62°$.

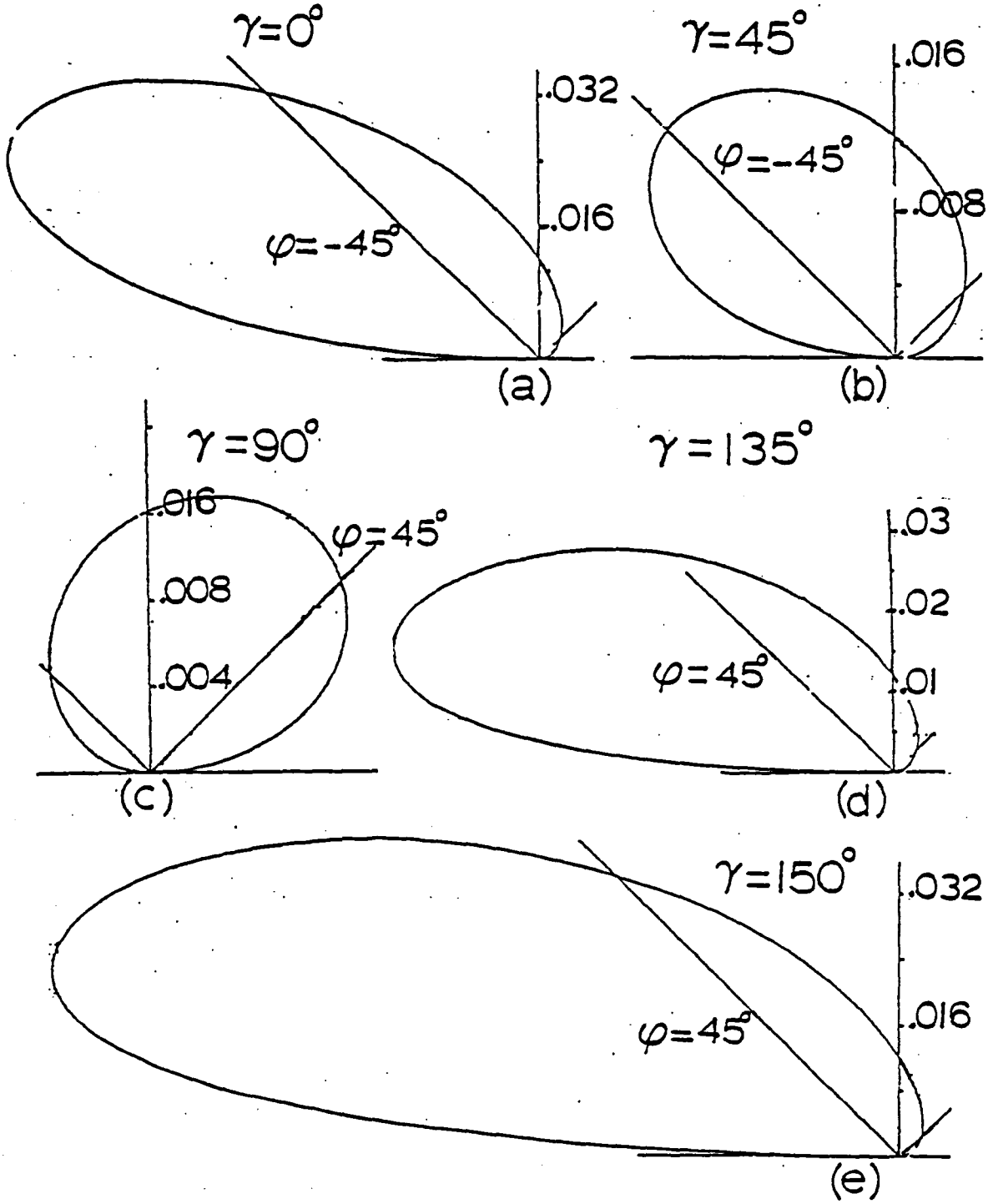

Fig. 5.4a-e Plot of the magnitude of the three-dimensional acoustic directivity $D^*_{\sqrt{y}}(\gamma,\phi)$ for $k_x=4$, M=.8, $\Lambda=80°$.

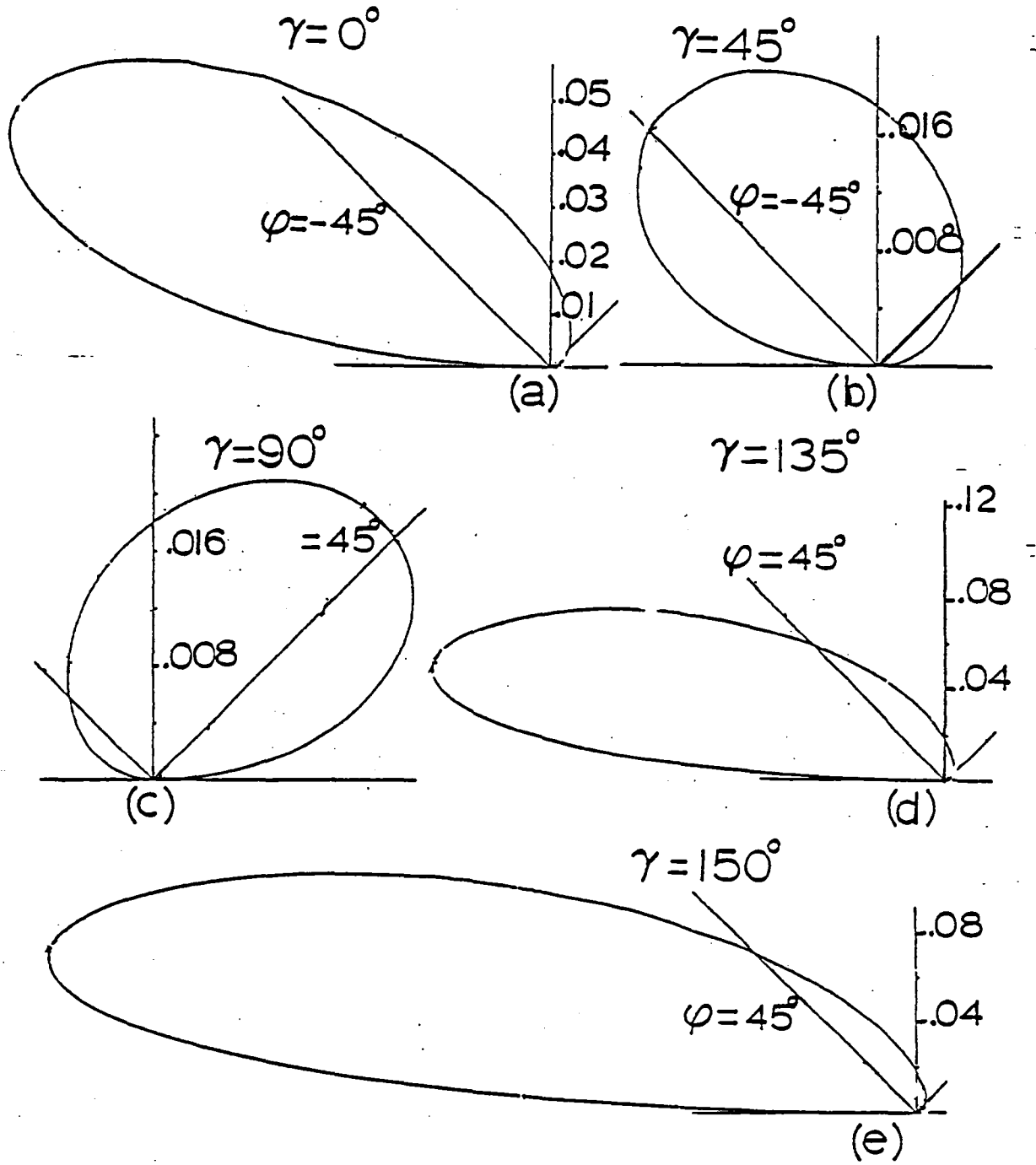

Fig. 5.5a-e Plot of the magnitude of the three-dimensional acoustic directivity $D^{*}_{\gamma}(\gamma, \phi)$ for $k_x=10$, $M=.8$, $\Lambda=62°$.

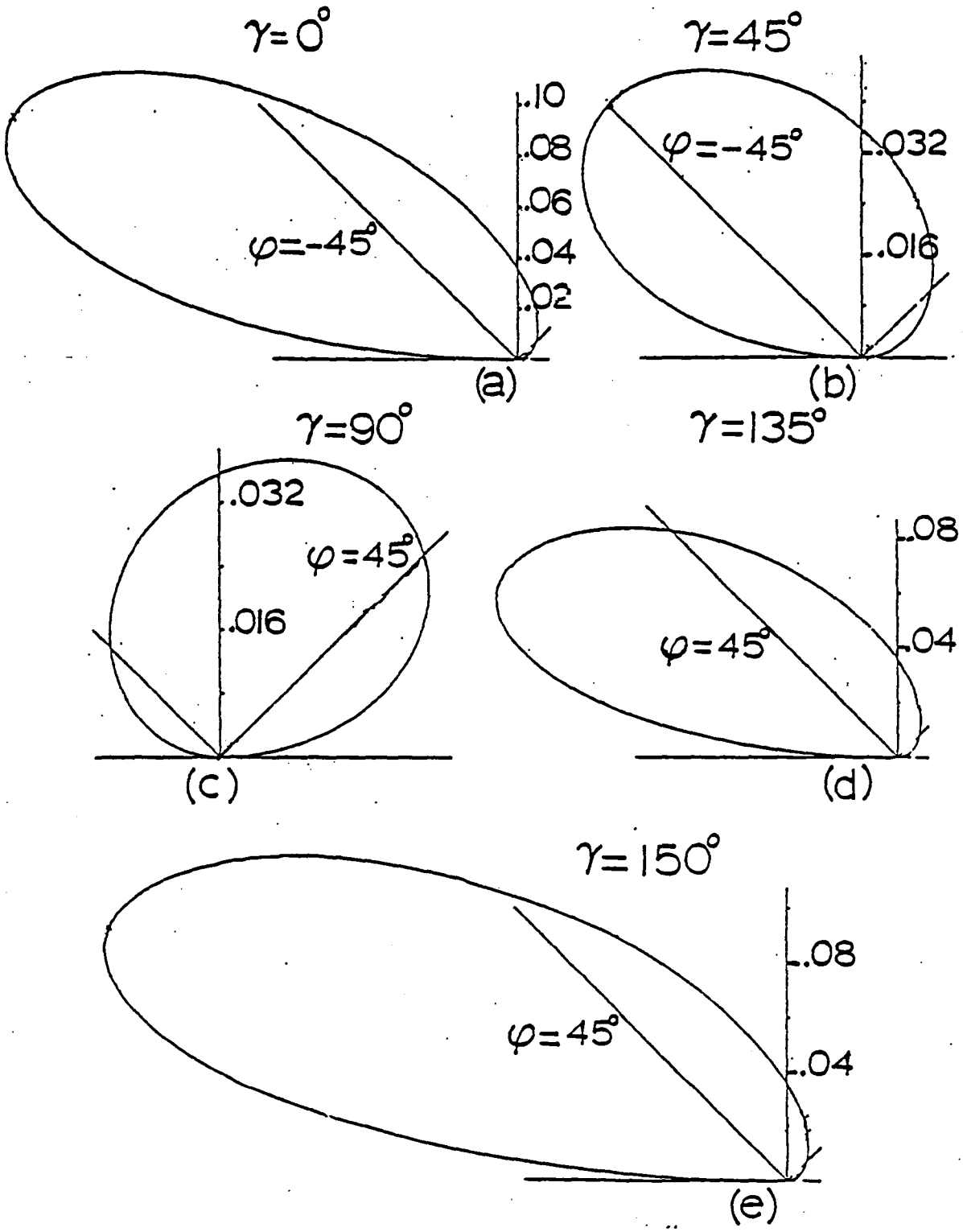

Fig. 5.6a-e Plot of the magnitude of the three-dimensional acoustic directivity $D^{*}_{c.o.}(\gamma, \phi)$ for $k_x=4$, $M=.8$, $\Lambda=62°$.

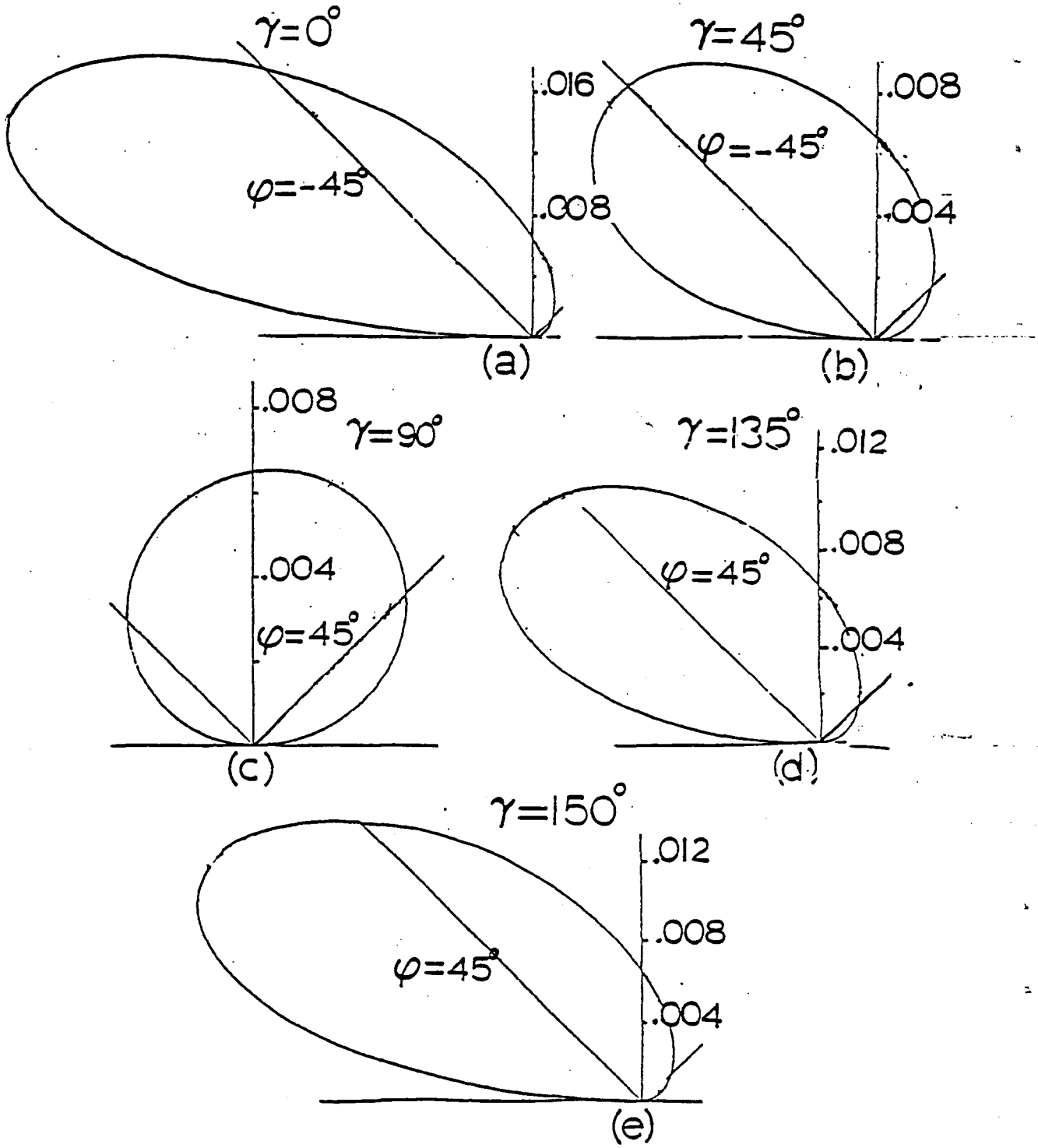

Fig. 5.7a-e Plot of the magnitude of the three-dimensional acoustic directivity $D^*_{c.o.}(\gamma, \phi)$ for $k_x=4$, $M=.8$, $\Lambda=80°$.

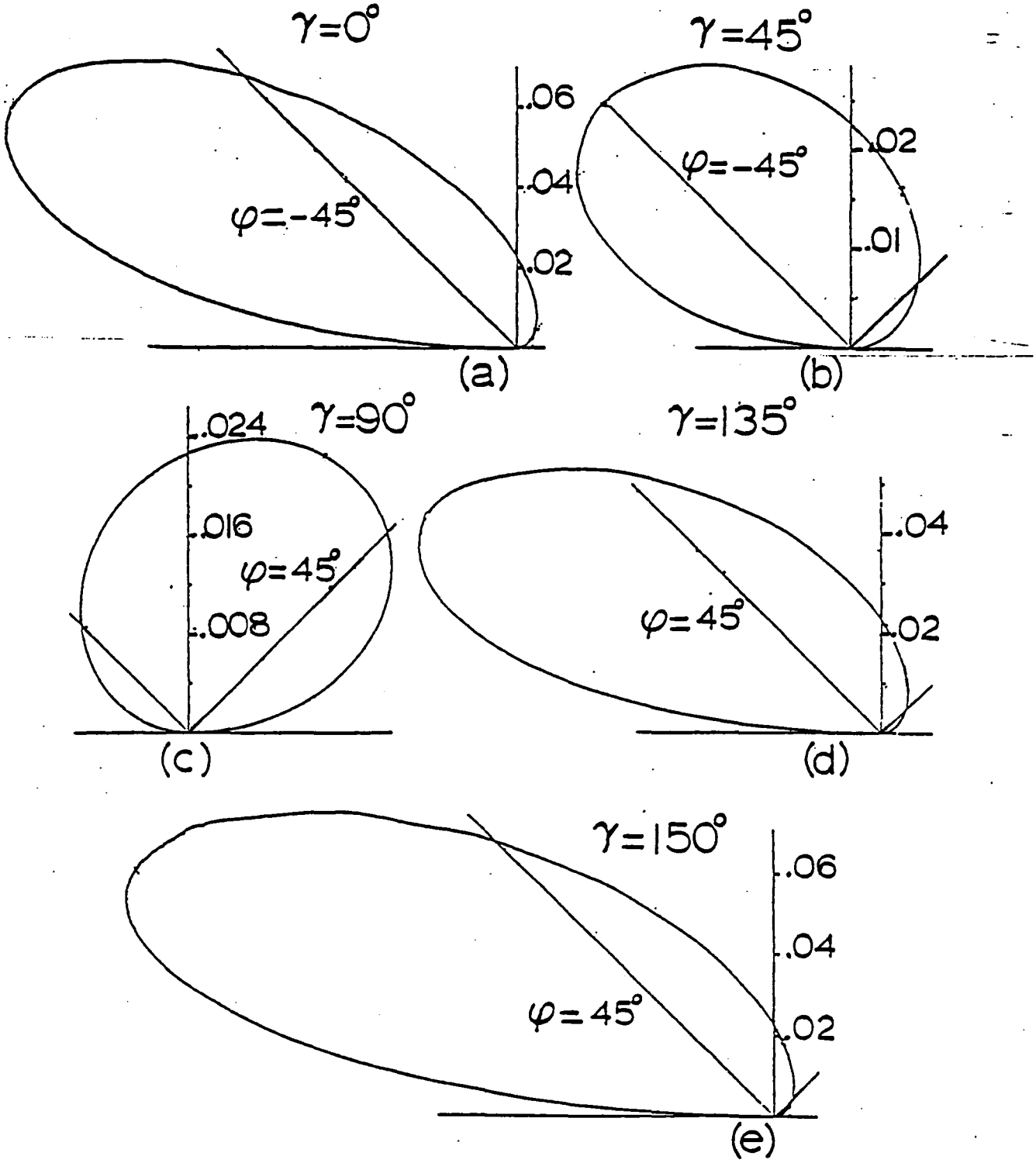

Fig. 5.8a-e Plot of the magnitude of the three-dimensional acoustic directivity $D_{\tilde{c}.\delta.}(\gamma, \phi)$ for $k_x=10$, $M=.8$, $\Lambda=62°$

1. Report No.	2. Government Accession No.	3. Recipient's Catalog No.
NASA CR-166297		

4. Title and Subtitle	5. Report Date
Aeroacoustic Theory for Noncompact Wing-Gust Interaction	October 1981
	6. Performing Organization Code

7. Author(s)	8. Performing Organization Report No.
Rudolph Martinez and Sheila E. Widnall	FDRL Report No.81-7
	10. Work Unit No. T-5486

9. Performing Organization Name and Address	11. Contract or Grant No.
Massachusetts Institute of Technology Cambridge, Massachusetts 02139	NSG-2142
	13. Type of Report and Period Covered Contractor Report-Final

12. Sponsoring Agency Name and Address	14. Sponsoring Agency Code
National Aeronautics & Space Administration Washington, D.C. 20546	RTOP 505-42-41

15. Supplementary Notes

Wayne Johnson, Technical Monitor, Mail Stop 247-1, NASA Ames Research Center, Moffett Field, CA 94035 (415) 965-5043 FTS 448-5043

16. Abstract

Three aeroacoustic models for noncompact wing-gust interaction were developed for subsonic flow. The first was for a two-dimensional (infinite-span) wing passing through an oblique gust. The second model was a simple spanwise superposition of two-dimensional solutions to account for the three-dimensional acoustic effects of wing rotation and of finiteness of wing span. The developed three-dimensional theory for a single gust was applied to calculate the acoustic signature in closed form due to blade-vortex interaction in helicopters. The third model was a quarter-infinite plate with side edge passing through a gust at high subsonic speed. The spectra predicted by the three-dimensional models developed for noncompact wing-gust interaction decay algebraically as the inverse of reduced frequency. Since compact models developed elsewhere predict spectra which reach a plateau at high frequencies, it was concluded that peak values of acoustic signals due to noncompact loadings should be less than those from compact loadings.

17. Key Words (Suggested by Author(s))	18. Distribution Statement
rotor noise wing/vortex interaction gust-induced loading	Unclassified - Unlimited STAR Category 02

19. Security Classif. (of this report)	20. Security Classif. (of this page)	21. No. of Pages	22. Price*
Unclassified	Unclassified	126	

*For sale by the National Technical Information Service, Springfield, Virginia 22161

End of Document